NEUTRON SPECTROSCOPIC FACTORS OF ^{56}NI VIA ^{56}NI(P,D)^{55}NI REACTION IN INVERSE KINEMATICS

By

Alisher Sanetullaev

A DISSERTATION

Submitted to
Michigan State University
in partial fulfillment of the requirements
for the degree of

DOCTOR OF PHILOSOPHY

Physics

2012

ProQuest LLC.
789 East Eisenhower Parkway
P.O. Box 1346
Ann Arbor, MI 48106 - 1346

ABSTRACT

NEUTRON SPECTROSCOPIC FACTORS OF ^{56}NI VIA ^{56}NI(P,D)^{55}NI REACTION IN INVERSE KINEMATICS

By

Alisher Sanetullaev

Transfer reactions have been the classic tool for studying the angular distributions, the excitation energies, and the spectroscopic factors of possible single-particles states. With the advent of radioactive beams, there has been a renewed effort to utilize them in transfer reactions in inverse kinematics. The exact shell structure of the unstable doubly magic nucleus ^{56}Ni has attracted a lot of interest recently. To test if ^{56}Ni has a closed $f_{7/2}$ orbital, we have measured the ^{56}Ni(p,d)^{55}Ni transfer reaction with the radioactive ^{56}Ni beam in inverse kinematics for the first time at the NSCL using the HiRA array and S800 spectrograph. The spectroscopic factor predicted by the independent particle model is 8, shell-model calculations give a value of 6.8. We have extracted spectroscopic factors of the ^{56}Ni(p,d)^{55}Ni reaction, for the ground and two excited states of ^{55}Ni. The neutron SF value of 7 for the ^{56}Ni(p,d)^{55}Ni ground state agrees with shell-model calculations and is consistent the view that ^{56}Ni is a closed shell nucleus. This result supports the use of ^{56}Ni as a core in shell-model calculations. Another important goal was to study the structure of ^{55}Ni by determining the spin and parities of excited states. We have assigned an ℓ value of 1 for the ℓ transfer to first excited state of ^{55}Ni for 2.089 MeV state of ^{55}Ni. We have extracted a spectroscopic factor of 0.14 for this state. This serves as a second test of the shell model, and the results agree with the shell model calculations. We have confirmed the tentative $\ell = 0$ assumption for 3.185 MeV state. A neutron spectroscopic factor of 1.2 was obtained for this state.

To my family and to the memory of my brother Aydos

ACKNOWLEDGMENTS

I would like to thank my advisor, Bill Lynch. I have learned a lot about being a scientist from him. I would like to thank Betty Tsang for her caring attitude. Her diligent planning and support has helped me tremendously. I would also like to personally thank the other members of my guidance committee, Vladimir Zelevinsky, Scott Pratt and Norman Birge. They have given me encouragement to focus on the task at hand.

My roommates and friends during the graduate school years, Dave Miller, Davitt Driscoll, Steven Waldauer and Barath Coleppa have been great friends. I have gotten to know many people in the physics department, as well as other departments.

The operators and staff at the NSCL have been tremendous help. Thank you Jon Bonofiglio, Randy Renczok, Gene and Shannon. I also appreciate the help Len Morris and Craig Snow have given with the experimental setup design.

Fellow graduate students Angelo Signoracci, Andrew Ratkiewicz, Rhiannon Meharchand, Phil Voss, Sean McDaniel and many others have made my days at the NSCL even more interesting. I am indebted to HiRA group members Andrew Rogers, Jenny Lee, Micha Kilburn, Dan Coupland, Mike Youngs, Vlad and Daniela Henzl for their hard work and team spirit. Tilak Ghosh has been a good friend and a mentor.

I am thankful to my wife, Aysulu, and constant support during my long and arduous journey towards finishing my dissertation. Last but not least, my dad Esbosyn, my mom Gulistan and my siblings Aybek, Ersultan, Gulaim and Ernazar have always been a source of great encouragement.

TABLE OF CONTENTS

LIST OF TABLES

LIST OF FIGURES

Chapter 1

Introduction

1.1 The atomic nucleus and isotopes

Understanding the properties of the atomic nucleus, which lies in the center of atoms that are the building blocks of baryonic matter, is one of the important goals of modern science. Each nucleus is defined by its mass number A, which is equal to the sum of neutron and proton numbers, and charge Z, which is equal to the number of protons. The number of protons Z defines the *element*, and the number of neutrons N defines the *isotope*.

The force that holds protons and neutrons together in a nucleus is called the *strong interaction*. It is indeed the strongest force in nature, other interactions being electromagnetic, weak and gravitational. The strong force acts only at very small distances of a few femtometers, and in this domain, it is about 100 times stronger than the electromagnetic forces. The nucleon-nucleon interaction derived from this force keeps the nucleus bound, and can be deduced from scattering experiments that study nucleon-nucleon collisions. As the Coulomb force can be viewed as the result of the exchange of photons between charged particles, the strong force between nucleons at longer distances can be viewed as the result of the exchange of mesons, first suggested by Yukawa in 1935 [1]. The theory that describes the strong interactions is called quantum chromodynamics [2].

However strong the strong force may be, it cannot hold an indefinite number of protons and neutrons together. There are a number of factors that limit the proton-neutron number space to a domain of allowed nuclei. The boundaries of this domain are the neutron and proton drip lines, and the spontaneous fission border. At the neutron drip line, the nucleus cannot add more neutrons as the separation energy of these extra neutrons would be negative, and the nucleus would be neutron unbound. Similarly, beyond the proton drip line, the nucleus would become sufficiently proton unbound that they would spontaneously emit the extra protons. Most nuclei at the limit of nuclear binding are radioactive. As the nuclei become heavy and contain more protons, the Coulomb force acting between the protons leads to spontaneous fission, providing another limit to the domain of nuclei. Figure 1.1 shows the chart of the nuclides, with proton numbers on the vertical axis and neutron numbers on the horizontal axis. The locus of black points, called the *valley of stability*, represents the stable isotopes. The blue region outlying this valley represents the known unstable isotopes, and is analogous to "hills" from which short-lived nuclei decay and fall into the valley of stability, turning into stable isotopes. These decays are not emission of nucleons, but β decays changing neutrons to protons or vice-versa in the direction of stability.

1.2 The Structure of the Atomic Nucleus

Although the knowledge about the nucleon-nucleon interaction is in general quite good, it is not sufficient in order to describe the structure of the atomic nucleus with precision. This is because of the emerging structures in many-body systems that are very complicated and extremely difficult to calculate from the individual interactions in complex nuclei. Therefore it is necessary to use models that describe some aspects of the real system. In general, there are two types of simplified models that describe the nucleus, *collective models* which

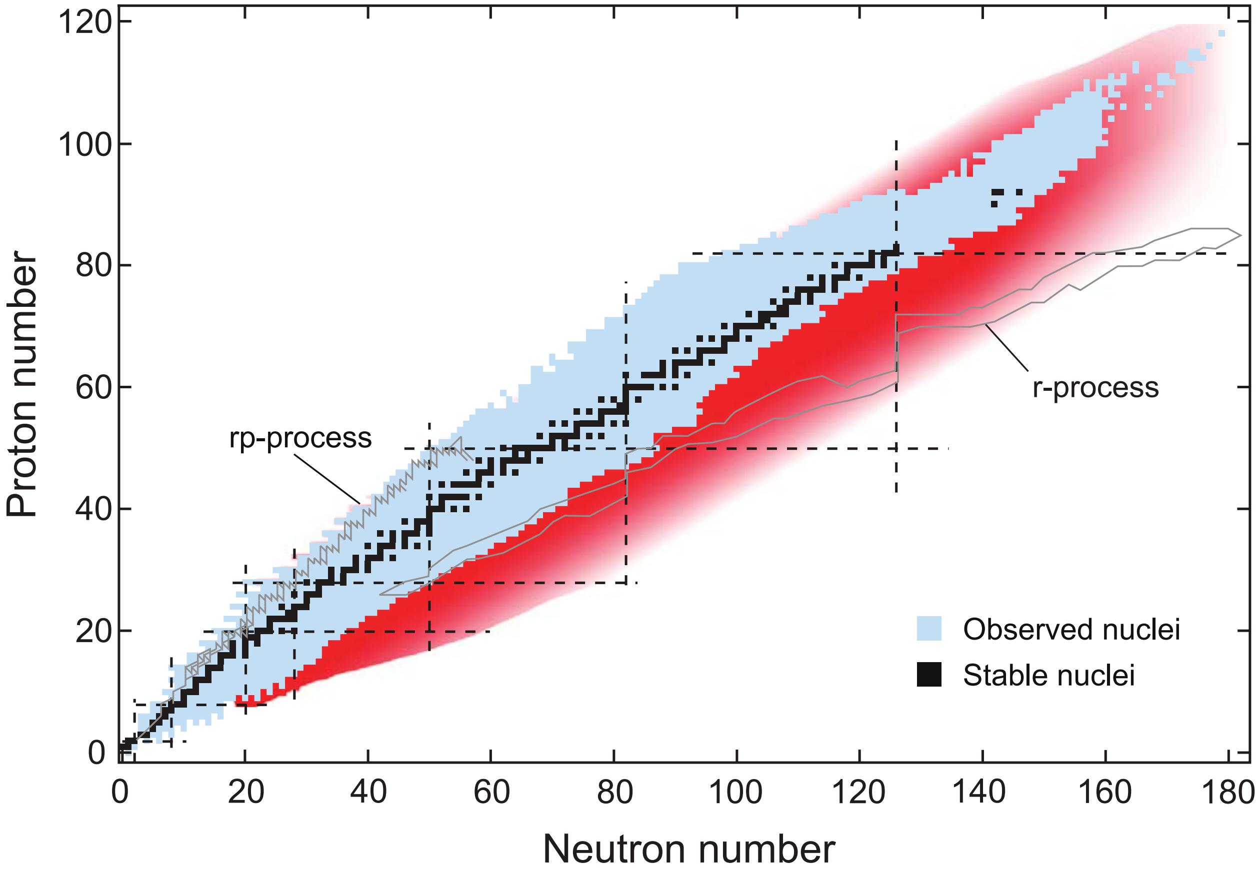

Figure 1.1: Chart of nuclides with proton numbers Z versus neutron numbers N. Dashed lines represent the magic numbers. Stable isotopes are shown in black and the observed unstable nuclei are shown in blue. Nuclei relevant in the astrophysical rp- and r-processes are shown as well (adopted from [3]). For interpretation of the references to color in this and all other figures, the reader is referred to the electronic version of this dissertation.

focus on the behavior of nucleons as they act together, and *independent particle models* that assume that the Pauli principle restricts the collisions of the nucleons inside the nucleus and leads to a more independent movement of the nucleons in the average common nuclear field. Modern theory tries to unify these models by including these collective phenomena arising from residual interactions.

The Liquid Drop Model belongs in the collective models class. As the name suggests, this model is based on the assumption that the nucleus behaves like a liquid, due to saturation of forces both in liquid and nuclear matter. In the 1930s this model was used to obtain the Bethe-Weiszacker *semi-empirical mass formula* [4]. It describes the nuclear mass as a function of five terms: volume energy, surface energy, Coulomb repulsion between the protons, asymmetry energy, and pairing. The model agrees well with experimental data on average, but for certain numbers of protons and neutrons in nuclei, there is considerable discrepancy between the model predictions and experimental data. By comparing experimental nuclear binding energies to calculated energies using the Bethe-Weiszacker formula, it was found that nuclei with numbers of neutrons or protons at 8, 20, 28, 50, 82 and 126 were more stable than expected [4,5]. These numbers came to be called *magic* numbers. Nuclei corresponding to magic numbers exhibit greater natural abundance as a consequence of their stability. Isotopes that have a magic number of both neutrons and protons are called *doubly-magic*, while those that have a magic number of one or the other are known as *semi-magic*. Magic nuclei tend to be spherical, and even-even nuclei in their vicinity possess a higher energy of the first excited state ($E(2^+)$) and a smaller reduced transition probability of the gamma-transition ($B(E2;\, 2^+ \rightarrow 0^+)$).

To explain the magic numbers and related physics, Mayer and Jensen [6] proposed the shell model of atomic nuclei, for which they shared the 1963 Nobel Prize in Physics. The original shell model assumes that the nucleons move inside the nucleus independently of each other and are subject to a central *mean-field* potential. In the simplest version of the shell model, often called the Independent Particle Model (IPM), each nucleon occupies a single-particle state in the nuclear spherical mean-field potential created by all of the nucleons in the *core*. The core is the part of the nucleus which is approximately inert at low-energy excitations. Frequently a harmonic oscillator or a more realistic Woods-Saxon potential is used as the mean field [6–8]. The Woods-Saxon potential has the form

$$V(r) = \frac{V_0}{1 + exp[(r - R_0)/a_0]} \tag{1.1}$$

where R_0 and a_0 are radius and diffuseness parameters, respectively. Due to its simplicity, this model does not take into account the correlations in the motion of particles outside the core or residual interactions between the valence particles and the core. Protons and neutrons may occupy the same state as they are not restricted by the Pauli principle and can consequently fill the orbitals independently. Each nucleon state is characterized by its single-particle energy and quantum numbers (n, l, j, m), where n is associated with the number of nodes of the radial wave function, and l and j are the orbital and total angular momenta. The maximum occupancy in each neutron (proton) orbital is $(2j + 1)$ [6–8]. The left column in Figure 1.2 shows the calculated levels for harmonic oscillator potential. The calculated magic numbers of 2, 8, 20, 40 and so on correspond to observed magic numbers only up to the third number. The middle column in Figure 1.2 shows the calculated levels for Woods-Saxon potential. The calculated magic numbers from this potential do not completely correspond to observed magic numbers either. Mayer and Jensen realized that with a strong spin-orbit force included in the nuclear spherical mean-field potential from the core, the shell model produces significant energy gaps at the magic numbers [6–9] and predicts the correct ordering of the single-particle orbits for stable isotopes as shown in the right column of Figure 1.2. In addition, it reasonably describes the nuclear static and dynamic properties of low-lying states in spherical stable nuclei and serves as a foundation of the more sophisticated modern shell model development [10].

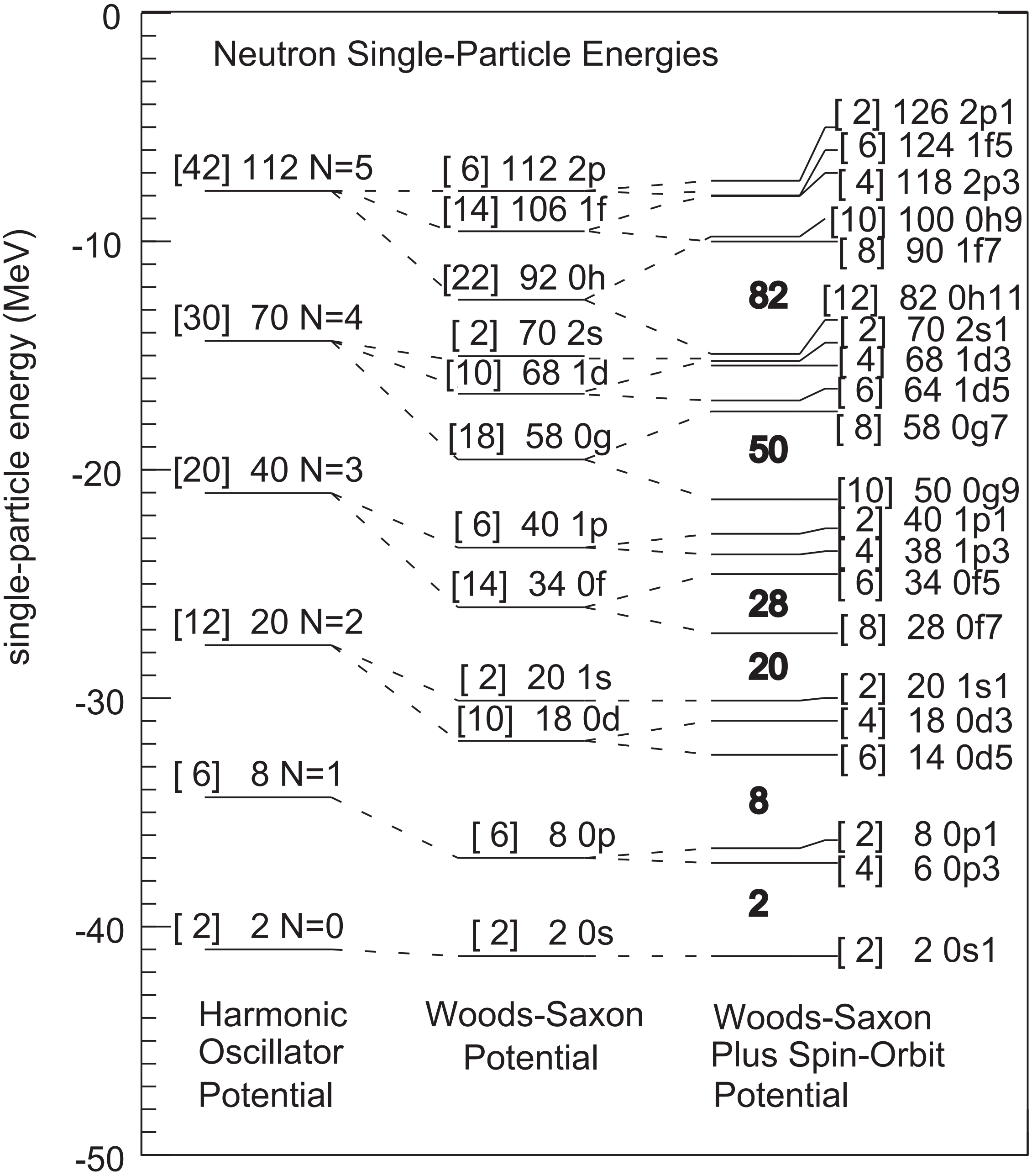

Figure 1.2: Nuclear shell structure [9].

The attempts to derive the bulk properties of nuclei based solely on the mean-field models are not completely successful, as the real situation is more complicated and it is necessary to consider the residual interactions and resulting *nucleon-nucleon (NN) correlations*. The Hamiltonian for a two-body nucleon-nucleon (NN) interaction in a nucleus can be written as:

$$H = \sum_i (\frac{\vec{p}_i^2}{2m}) + \sum_{i<j} V_{NN}(\vec{r}_i - \vec{r}_j) \tag{1.2}$$

Due to the fact that there is no exact solution for such a complicated many-body Hamiltonian, a single-particle approximation is used in which the Hamiltonian is divided into two terms. The first term, $H^{(0)}$, describes a particle moving in an effective average potential, and the second term, $H^{(1)}$, describes the residual interactions.

$$H = \sum_i [\frac{\vec{p}_i^2}{2m} + U(\vec{r}_i)] + [\sum_{i<j} V_{NN}(\vec{r}_i - \vec{r}_j) - \sum U(\vec{r}_i)] = H^{(0)} + H^{(1)} \tag{1.3}$$

The NN correlations are caused by a strong short-range repulsion of nucleons and a long-range attractive interaction between the valence nucleons. The short-range repulsive force modifies the compressibility of nuclei by shifting the single-particle wave functions to high energy orbits [11, 12]. The residual interaction and emerging NN correlations lead to a state of the nucleus with *mixed IPM configurations* of the same angular momentum and parity.

Due to the mixing of configurations, a single-particle orbital is occupied only a fraction of the time. The weight of the particular configuration in the wavefunction of the nucleus is quantified by a *spectroscopic factor* (SF). Spectroscopic factors are the common ground between transfer or knockout reaction theory and nuclear structure theory. The SF is not an observable, although it can be extracted by comparing the experimental cross section with a transfer or knockout *reaction model* calculation, such as *Distorted Wave Born Approximation* model described in Section 2.2.

The theoretical SF for removing a neutron from nucleus B is a measure of the degree to which the wave function of the initial nucleus B overlaps with the wave function of the final nucleus A plus a neutron in a specific single-particle state [9]. The wave function for a specific state ψ_i^B in initial nucleus can be expanded in terms of a summation over the complete set of states ψ_f^A in final nucleus:

$$\psi_i^B = \sum_f \Phi_f^i(\vec{r})\psi_f^A, \tag{1.4}$$

where $\vec{r}$ is the coordinate of the neutron being transferred in the reaction above. In the reaction where particles are transferred from state ψ_i^B to a specific state ψ_f^A, the overlap function $\Phi_f^i(\vec{r})$ is used for calculation of the SF:

$$SF = \int |\Phi_f^i(\vec{r})|^2 dr, \text{ where } \Phi_f^i(\vec{r}) =< \psi_f^A|a(\vec{r})|\psi_i^B > \tag{1.5}$$

where $a(\vec{r})$ is the annihilation operator of the neutron.

The Independent Particle Model (IPM), or the extreme shell-model, which was briefly discussed above, provides the simplest means of calculating the wave function. In IPM, as shown in Equation 1.6, one can obtain a simple relationship between the spectroscopic factor and the number of valence nucleons (n) on the orbital with total angular momentum j [13], assuming maximal pairing (with only one unpaired nucleon).

$$SF = \begin{cases} n, & n = even \\ 1 - \frac{n-1}{2j+1}, & n = odd \end{cases} \tag{1.6}$$

It is notable that for an odd number of nucleons in the orbital, the spectroscopic factor is less than or equal to 1. This is because of the maximal pairing assumption, and only the transfer of the single unpaired nucleon will lead to the final state of the remaining nucleus. If a paired nucleon is removed, the total spin will be different, thus leading to a different final state.

For a more realistic depiction of the nucleus, the residual interaction between the nucleons must be taken into account. The residual interaction introduces some long-range correlations in the nuclear wave function beyond the mean field and can result in the reduction in the single-particle strength. Modern Large-Basis Shell-Models (LB-SM) were developed to take into account the shell-model configuration mixing and construct the wave functions using different effective interactions in a specific Hilbert space. The effective interactions are usually obtained by fitting the two-body matrix elements and single-particle energies to the experimental energy levels, empirical nuclear masses, charge radii and low-lying excited state spectra for a wide range of nuclei within the region being studied [10]. In the present dissertation, to compute the wave functions and theoretical spectroscopic factors, an LB-SM code, NuShellX [14] was used.

The large-basis shell-model approach has been developed to include some of the NN correlations in the nuclear structure studies [10]. The effective interactions used in current shell models can describe much of the long-range component of the interactions [10, 15]. Currently available residual interactions provide satisfactory descriptions for the light to medium mass nuclei in sp-, sd- and pfg- shell regions [16]. In order to be able to describe satisfactorily the nuclear spectra including the collective excitations, the shell model orbital space should be sufficiently large, which creates computational problems. Other theoretical approaches to describe full nucleon correlations are being developed as well [15, 17, 18].

1.3 Motivation for the Experiment

For the shell model of the nucleus, magic numbers are akin to keystones for buildings. One of the important nuclei for understanding the evolution of shell closure and single-particle energies is the doubly-magic ^{56}Ni. The **^{56}Ni(p,d)^{55}Ni** reaction, which studies the transfer of one neutron from ^{56}Ni to ^{1}H, will be the focus of this dissertation. Several experiments have been performed recently in order to investigate the single-particle structure of nuclei in the vicinity of ^{56}Ni [19–22]. If the single-particle picture of the neighboring nuclei is a reasonable approximation, ^{56}Ni can be used as a core for a shell model space.

It seems viable that low-lying states in ^{57}Ni could be characterized as single-particle valence neutron states on top of the closed-core ^{56}Ni, based on the results of high-energy knockout reaction measurements of spectroscopic factors of ^{57}Ni in [20]. Figure 1.3 illustrates how a single-particle picture may be visualized in terms of a ^{56}Ni core and valence nucleons on top of it, in contrast to the many-body picture where there is no core or there are too many nucleons on top of a small core. Recent computation of the "single-particle spectral function of ^{56}Ni within the framework of self-consistent Green's functions theory" [18], as well as *Large-Basis Shell-Model* (LB-SM) calculations by Horoi et al. [23], support this single-particle view. A recent experiment performed by Minamisono et al. [21] on magnetic moment of the ground state of ^{57}Cu, which could be described as one valence proton outside ^{56}Ni, resulted in a magnetic moment much smaller than expected from a single-particle picture, implying breaking of the shell model core. However, a later more precise measurement using in-gas-cell laser spectroscopy performed by Cocolios et al. [22] suggests that there is no shell breaking for this nucleus. Because of the more accurate measurements, the results from the latter study seem to be more convincing.

A measurement of the ground state nuclear magnetic moment of ^{55}Ni was performed by Berryman et al [24] using the β-ray detecting nuclear magnetic resonance technique, the same technique that was used in the work Minamisono et al. mentioned above [21]. The experimental magnetic moments agree with the shell model calculations in the full fp shell-model space with the GXPF1 interaction [25], and differ from the single particle picture. Combining this result with the earlier measurement of the nuclear magnetic moment of the ^{55}Co [26], the isoscalar spin expectation value of 0.91±0.07 was extracted. This value is very close to single particle value of 1. Because of this, ^{56}Ni could be considered as a good core. However, the authors claim that this agreement is due to an enhancement by a large orbital angular momentum, canceling the effect of configuration mixing. Thus, they conclude that the ^{56}Ni core is soft, without implying a shell breaking at ^{56}Ni.

Another important motivation for the experiment is to study the structure of ^{55}Ni by determining the spin and parities of as many excited states as possible. In this regard, ^{55}Ni remains the least studied of the quartet of the nuclei one nucleon away from ^{56}Ni, ^{55}Ni (neutron hole in $0f_{7/2}$), ^{55}Co (proton hole in $0f_{7/2}$), ^{57}Ni (neutron particle in $1p_{3/2}$) and ^{57}Cu (proton particle in $1p_{3/2}$). The only firmly known spin and parity in this nucleus is the ground state with spin and parity of $7/2^-$ [27, 28]. The spin and parities of the first three excited states are unknown, and only 6 out of 22 known states below 7 MeV have tentative spins and parities [28]. Obtaining experimental information about these states will provide further impetus for shell-model calculations and improve our understanding of nuclei in the

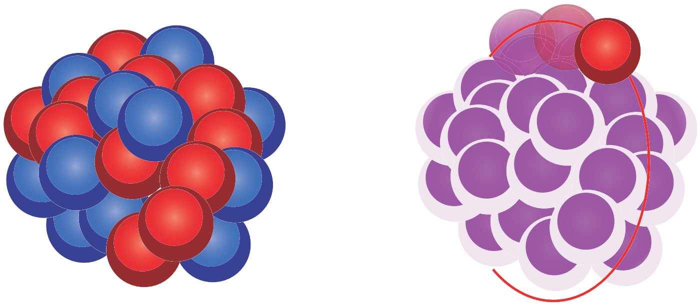

Figure 1.3: Many-body (left) or single-particle (right) picture? Adopted from [3].

vicinity of ^{56}Ni.

In order to constrain the complex many-body physics to the shell model consisting of an inert core and valence nucleons, it is important to obtain the configurations of the single-particle or hole states by directly measuring them. The classic tools for the investigation of single-particle states have been single-nucleon transfer reactions, such as (d, p) and (p, d) reactions for probing the neutron states, and the corresponding reactions such as (d,^{3}He) and (^{3}He,d) and (^{4}He,t) for probing proton states [29]. Transfer reactions provide us with information about the excitation energies of the states in the residual nucleus, about the occupancies or spectroscopic factors of the various single-particle orbits, and the angular momentum of the orbital from the angular distributions and .

The most direct way to test the configuration of ^{56}Ni is to measure the occupations of the neutrons or protons in the $f_{7/2}$ orbits. In the closed-shell model for ^{56}Ni, these orbits will be completely filled. Direct measurements of the spectroscopic factors of the neutron hole state in ^{56}Ni using the pickup (p, d) reaction will determine the degree to which the neutron $f_{7/2}$ orbit is indeed a closed shell. If the shell is not closed, the experimental data can be used to determine the measure of configuration mixing. Such information provides constraints to the ^{56}Ni core in shell model calculations. Measurements of single-nucleon removal mechanisms, such as single-nucleon transfer or knockout, provide constraints on spectroscopic factors calculated from the overlap between many-body wave functions of the initial and final states [13].

To understand the evolution of the neutron single-particle states outside the ^{56}Ni core, the neutron spectroscopic factors (SF) of different Ni isotopes were extracted using the angular distributions measured in the (p,d) and (d,p) reactions in the literature [30]. In this analysis, the consistent procedure to take into account the deuteron breakup as in Reference [31] was adopted. This procedure uses global nucleon optical potentials and the *adiabatic approximation*, which is discussed in Subsection 2.2.1. Neutron spectroscopic factors obtained in this way for light nuclei with $Z = 3 - 24$ are consistent with the predictions from large-basis shell model calculations [31]. A priori, transfer reactions do not yield absolute spectroscopic factors as the analysis depends on other input parameters such as the geometry of the bound state wave-function as well as the optical potentials used in the reaction model [32]. However, if the analysis utilizes a consistent set of parameters, the absolute SF values may change depending on the choice of optical potentials, but the relative SF could be determined reliably [32]. In Figure 1.4, the extracted SF values are compared to predictions from the large basis shell model which includes the latest $T = 1$ effective interactions within the $\mathrm{f}_{7/2}\mathrm{p}_{3/2}\mathrm{p}_{1/2}\mathrm{g}_{9/2}$ model space [33]. The dashed line indicates perfect agreement. Except for ^{63}Ni, the experimental spectroscopic factors for the Ni isotopes are about 20% lower than the predictions from shell model. If the absolute SF values are not a concern, the consistency of the SFs in Figure 1.4 suggests that the ^{56}Ni core and the effective interactions of the valence nucleons are understood.

The study of these states yields information about how the shell structure evolves from stable nuclei to rare isotopes with extreme neutron/proton ratio. For $N = 28$ isotones,

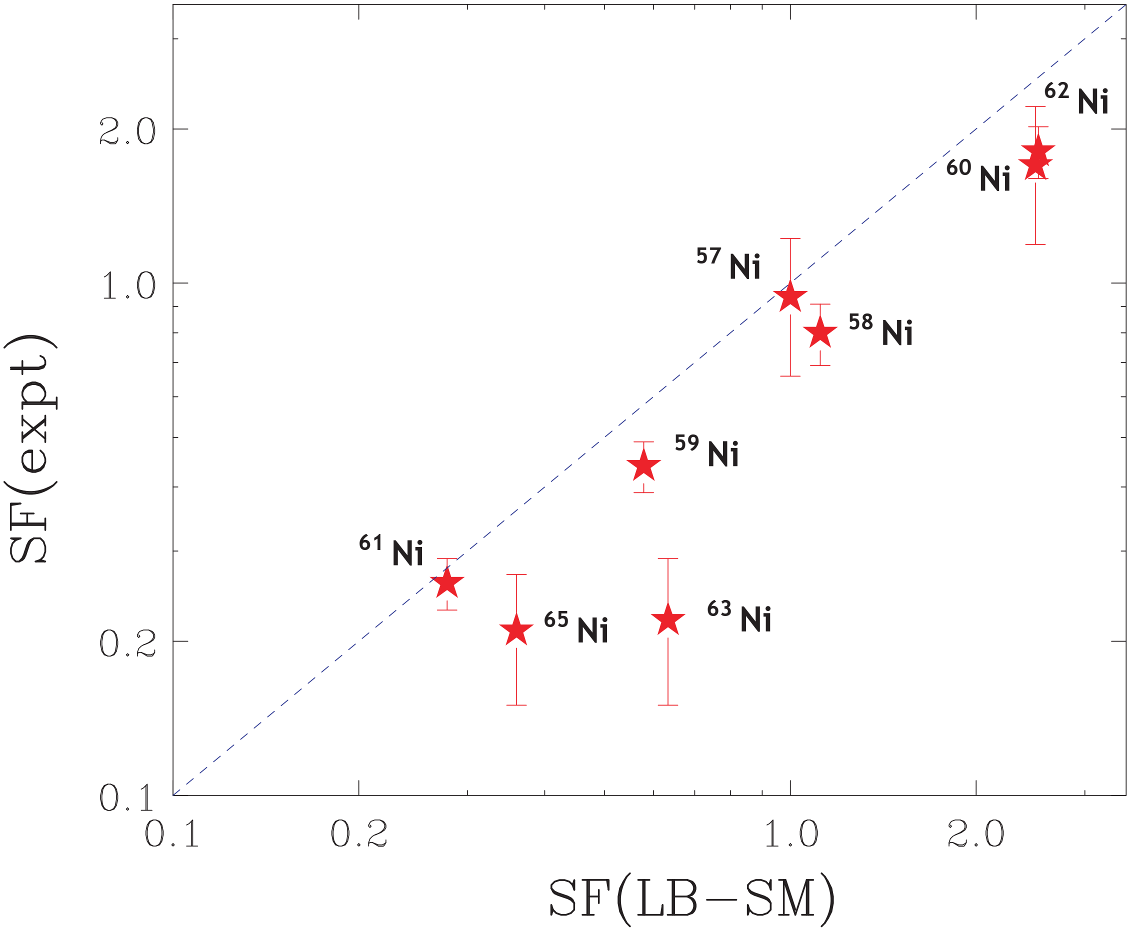

Figure 1.4: Comparison of spectroscopic factors to predictions from shell model for Ni isotopes using the new T=1 effective interactions and $f_{7/2}p_{3/2}p_{1/2}g_{9/2}$ model space [33]. The data are extracted from the literature [34].

the neutron spectroscopic factors for ^{48}Ca, ^{50}Ti and ^{52}Cr ($Z = 20$, 22 and 24) have been extracted [34] and they are plotted in Figure 1.5. As these are stable nuclei, neutron SF values are expected to not depend on the protons in the $f_{7/2}$ orbit. This may change as one moves to the $N = Z$ nucleus, ^{56}Ni (indicated by the double dashed lines on the right side of the figure) or to the more neutron rich nucleus, ^{46}Ar (indicated by the double dashed lines on the left). The current experiment will provide information on the evolution of the $N = 28$ shell from $Z = 18$ to $Z = 28$. Since there is very little information about the excited states of ^{55}Ni, the data from the current experiment will provide angular momenta and other information of the excited states that are populated by the (p, d) transfer reaction.

1.4 Organization of the dissertation

The remainder of this dissertation is organized as follows. In Chapter we discuss the theory of reactions and the Large Basis Shell Model and their common ground, spectroscopic factors. In Chapter we give an overview of the experimental setup and details of our measurement techniques for the ^{56}Ni(p,d)^{55}Ni reaction. We also provide a detailed description of the detectors used in the experiment including the S800 spectrograph, Microchannel plate beam tracking detectors, and the *High Resolution Array* (HiRA). In Chapter we describe the analysis of the raw data. We discuss the data analysis strategy, data corrections, and detector calibrations. In Chapter we discuss the physics data and results.

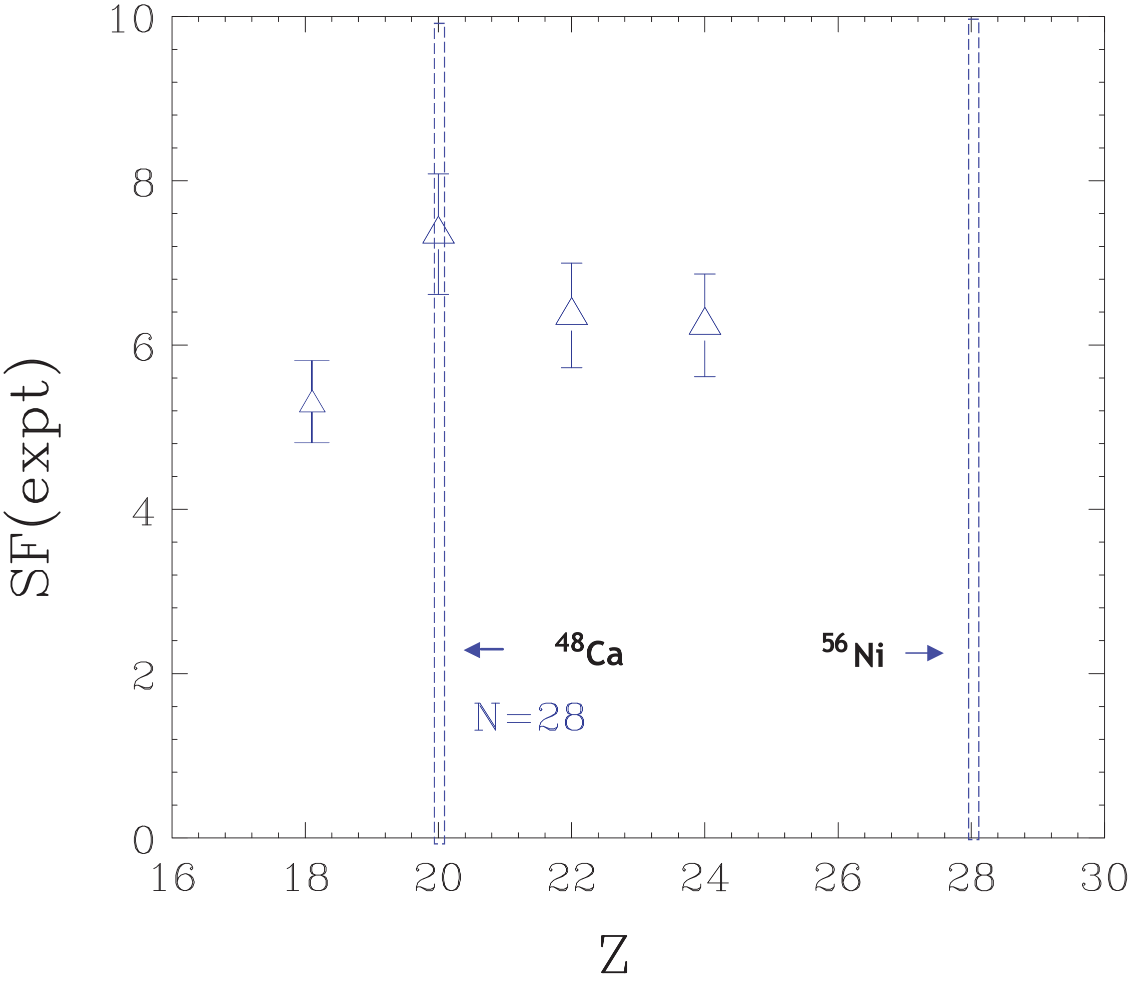

Figure 1.5: Spectroscopic factors for N=28 isotones. ^{56}Ni(p,d)^{55}Ni reaction is the proposed measurement. Open triangles are extracted SF values obtained from the past measurements [30].

Chapter 2

Theoretical Description

2.1 Direct Reactions

There are typically two nuclei in the *initial system* of nuclear reactions, an *incident projectile* colliding with a *target nucleus*. The initial system is transformed into a *final system*, containing the *reaction products*. For the ^{56}Ni(p,d)^{55}Ni reaction, this may be represented symbolically by:

$$A + a \rightarrow B + b \tag{2.1}$$

where a is the incident proton, A is the target nucleus (^{56}Ni), B is the *residual nucleus* (^{56}Ni), and b is the final deuteron. An even shorter notation is used as well: $A(a,b)B$. If any of the reaction products are in an excited state, this condition may be indicated by an asterisk, e.g. $A(a,b)B^*$.

In *direct reactions*, the duration of the interaction between the projectile and the target, with possible exchange of energy and particles, is short, comparable to typical time of passage through the diameters of the interacting nuclei. It should be noted that labeling of the lighter nucleus as the projectile and the heavier nucleus as the target is just a convention. The physics is independent of the frame of reference; therefore, interchanging the projectile and the target do not change the description of a reaction. Thus, we will continue to use (a,b) to denote the light particles, e.g. (p,d) or (d,p). In our experiment, as will be discussed in

Section 3.1, the heavier nucleus A is the projectile, and the lighter nucleus a is the target. The probability of the direct reaction increases with increased energy of the incident particle, since its wavelength gets smaller with higher energy, and the projectile can "probe" localized areas in the target nucleus. Typically, the reactions are *peripheral*, involving a few nucleons on the surface of the target nucleus. The time it takes for a direct reaction to happen is on the order of 10^{-22} s, while the compound nucleus reactions are approximately up to six orders of magnitude slower. It should be noted that the same final products can be obtained by both mechanisms. However, the angular distribution from the compound nucleus decay is isotropic, which can be distinguished from the forward peaked direct reaction angular distributions [35].

The main characteristic types of direct reactions are reactions involving only the exchange of energy, reactions involving exchange of particles, and reactions involving neither particle nor energy exchanges between the participants. The first type involves inelastic scattering of the incident particle, with the change in energy exciting a collective state of the nucleus, such as rotational or vibrational modes. The second type involves change in the particular composition of the participating nuclei. *Transfer reactions*, in which a nucleon is moved from one participating nucleus to the other, such as *pick-up* and *stripping*, are classical examples of this type. In a pick-up reaction, the projectile picks up a nucleon from the target, and similarly in a stripping reaction the projectile transfers a nucleon to the target nucleus. Our reaction of interest in this dissertation is a transfer reaction, namely a pickup reaction. We discuss the theory of direct transfer reactions in the next section. Another reaction of the second type is the *knock-out* reaction, in which the projectile knocks out a particle from the target without picking it up and continues on its path, resulting in three reaction products. The third type of direct reactions is *elastic scattering*, in which the projectile and the target have the same nucleon composition and same energy in the *center-of-mass* (CM) system. Elastic scattering reactions are not the focus of the present study.

2.2 Reaction Theory

In general, the *Distorted-Wave Born Approximation* (DWBA) is employed for theoretical analysis of direct transfer reactions. The approximation treats the direct reaction as a perturbation in the elastic scattering that causes the nucleon transfer between the projectile and the target. It is a single-step process in which the projectile (e.g. a proton) forms the *ejectile* (e.g. a deuteron) after a single interaction. The particles move in an *optical potential*, which is a single-channel complex potential that reproduces the energy average of the elastic scattering amplitude [36]. The complex part of the potential causes the absorption, analogous to electromagnetic waves being absorbed in dielectric materials with complex indices of refraction. This analogy is the reason for the naming of the potential.

The simple DWBA model does not take into account the break-up of the deuteron in A(p,d)B reactions. To correct for the break-up, an *adiabatic approximation* can be used, and the modified model is called *Adiabatic Distorted-Wave Born Approximation* (ADWA), which can be incorporated into the DWBA framework. The following subsection presents the DWBA formalism and the use of adiabatic approximation in ADWA.

2.2.1 Adiabatic Distorted-Wave Born Approximation

The basis of the distorted-wave Born approximation for direct transfer reactions (A+a→B+b) is the distorted-wave transition amplitude which is expressed as Equation 2.2. [13, 37–39].

$$\begin{aligned}T_{\alpha\beta}^{DW} &= \langle\chi_{\beta}^{(-)}(\vec{k}_{\beta},\vec{r}_{\beta})\psi_B\psi_b|V_{\alpha}-U_{\alpha}|\psi_A\psi_a\chi_{\alpha}^{(+)}(\vec{k}_{\alpha},\vec{r}_{\alpha})\rangle \\ &= \int d\vec{r}_{\beta}\int d\vec{r}_{\alpha}\chi_{\beta}^{(-)*}(\vec{k}_{\beta},\vec{r}_{\beta})\langle Bb|V_{\alpha}-U_{\alpha}|Aa\rangle\chi_{\alpha}^{(+)}(\vec{k}_{\alpha},\vec{r}_{\alpha})\end{aligned} \tag{2.2}$$

Here α and β are the entrance channel with projectile (proton) a and target nucleus A (^{56}Ni), and exit channel with ejectile b (deuteron) and final nucleus B (^{56}Ni), respectively. $\vec{r}_{\alpha}$ and $\vec{r}_{\beta}$ are the relative coordinates between projectile a and target nucleus A and between ejectile b and final nucleus B, respectively. V_{α} is the interaction between the projectile a and the target nucleus A. ψ_A and ψ_B are the internal wave functions of the target nucleus A and final nucleus B. $\chi_{\alpha}^{(+)}(\vec{k}_{\alpha},\vec{r}_{\alpha})$ is the solution of the Schrodinger equation for the incoming particle with the optical potential U_{α} in channel α. The function $\chi_{\beta}^{(+)}(\vec{k}_{\beta},\vec{r}_{\beta})$ is associated with the elastic scattering of the outgoing particle from the final nucleus B. The exact wave function of the system is described by a product of the internal wave functions of the outgoing particle ψ_b, the residual nucleus ψ_B and $\chi_{\beta}^{(+)}(\vec{k}_{\beta},\vec{r}_{\beta})$. In practice the term $V_{\alpha}-U_{\alpha}$ can be commonly replaced by the interaction between the transferred neutron and the projectile (proton) V_{an}.

The nuclear matrix element $\langle Bb|V_{\alpha}-U_{\alpha}|Aa\rangle$, with integration performed over all coordinates independent of $\vec{r}_{\alpha}$ and $\vec{r}_{\beta}$, can be expanded into the nuclear overlap integral as shown in Equation 2.3 , which carries single-particle state information (n,l,j,m), and into the overlap function between the projectile and ejectile as presented in Equation 2.5.

$$\int d\zeta_B\psi_B^*(\zeta_B)\psi_A(\zeta_B,\vec{R}) = \sum_{nljm}\langle J_BjM_Bm|J_AM_A\rangle\sqrt{S_{nlj}}\Phi_{nljm}(\vec{R}) \tag{2.3}$$

where ζ is the internal coordinate, $\langle J_BjM_Bm|J_AM_A\rangle$ is the Clebsch-Gordan coefficient,

$\sqrt{S_{nlj}}$ is the spectroscopic amplitude and $\Phi_{nljm}(\vec{R})$ is the normalized single-particle wave function.

Following Equations 2.2-2.3, the transition amplitude can be expressed in Equation 2.4 and the differential cross section is proportional to the square of the transition amplitude [39],

$$T_{\alpha\beta}^{DW} \propto \sum_{nljm} \sqrt{S_{nlj}} \int d\vec{r}_\beta \int d\vec{r}_\alpha \chi_\beta^{(-)*}(\vec{k}_\beta, \vec{r}_\beta) \Phi_{nljm}(\vec{R}) f(\vec{r}) \chi_\alpha^{(+)*}(\vec{k}_\alpha, \vec{r}_\alpha) \tag{2.4}$$

where

$$f(\vec{r}) = \langle \psi_b^*(\zeta_a, \vec{r}) | V_{an}(\vec{r}) | \psi_a(\zeta_a) \rangle \tag{2.5}$$

Equation 2.4 is called the *prior* form of the reaction amplitude, because it is based on the interactions in the entrance channel. This is the form used in calculations in the present dissertation. If instead the interactions in the exit channel were used, it would be called *post* form of the reaction amplitude. Equivalent results can be obtained using either form.

2.2.1.1 Nonlocality Correction

The simple optical model potentials are local, meaning that the particle at point $\vec{r}$ feels the potential only at that point. However, the realistic optical potentials should be nonlocal, affecting the wave functions of the projectile and ejectile within their acting range. The nonlocal potential acting on a wavefunction can be expressed as

$$V\Psi(r) = \int V(r, r')\Psi(r')dr' \tag{2.6}$$

Nonlocality can be expected wherever the potential is energy dependent due to the exchange terms required by the asymmetry of the overall wavefunction. Perey and Buck [40] studied nonlocal optical potentials by straightforward numerical means, factoring the nonlocal kernel $U(\vec{r}, \vec{r'})$ into a constant potential U_0 and a Gaussian nonlocality function.

$$U(\vec{r}, \vec{r'}) = U_0 \left(\left| \frac{\vec{r} + \vec{r'}}{2} \right| \right) G(\vec{r} - \vec{r'}) \tag{2.7}$$

where $G(\vec{r} - \vec{r'})$ is a Gaussian function normalized to unity over integration over $\vec{r}$ or $\vec{r'}$:

$$G(\vec{r} - \vec{r'}) = \frac{exp(-((\vec{r} - \vec{r'})/\beta_{NL})^2)}{\pi^{3/2}\beta_{NL}^3} \tag{2.8}$$

The parameters of this nonlocal potential can been obtained from fits of the experimental differential cross sections. It was found that the parameters were energy independent with suitable nonlocality [40].

2.2.1.2 Zero-Range and Finite-Range Interactions

The DWBA expression for the transition amplitude in Equation 2.4 involves a 6-fold integration over $\vec{r_n}$ and $\vec{r_p}$ after the integration of the nuclear coordinates B. To simplify the integration, it can be assumed that the transition amplitude receives contributions only from the region where the coordinates of the proton and neutron coincide so that we have the *zero-range approximation*:

$$D(\vec{r}) \equiv V_{pn}\psi_b(\vec{r}) \approxeq D_0\delta(\vec{r}) \tag{2.9}$$

The *zero-range strength* D_0 that is used in the zero-range approximation can be obtained by the integral of this equation over $\vec{r}$:

$$D_0 = \int r^2 V_{pn}(\vec{r})\psi_b(\vec{r}) dr \tag{2.10}$$

In reality, it may be necessary to take into account the finite range of interactions between nucleons. Otherwise the contribution from the interior of the nucleus will be overestimated. If the interaction potential range is small, a first order approximation can be made to the zero-range approximation, considerably improving the accuracy. This approach, called *local energy approximation* (LEA), is used as an approximation of the finite-range interaction for the deuteron [41]. The zero-range strength above is replaced by the *effective zero-range strength*:

$$D = (1 + k_b^2 \beta^2) D_0 \tag{2.11}$$

where β is the *finite-range effective radius* and $k_b = 2\mu_b \epsilon_b / \hbar^2$ is the bound state wave number for the deuteron. The parameters for LEA are given in Subsection 2.4.1.

2.2.1.3 Deuteron Breakup

The separation energy between the proton and neutron in deuteron is small, 2.224 MeV, as a result the deuteron breaks up easily in the field of the core nucleus. Thus, cross section calculations of (p, d) and (d, p) reactions using the DWBA calculations is usually not very reliable, especially at high incident energy, because of inadequate treatment of three body effects, i.e. effects arising from deuteron breakup.

Johnson and Soper [42] modified the DWBA theory with the adiabatic deuteron breakup approximation.In this approximation, the effective two-nucleon-nucleus interaction is assumed to be the sum of the nucleon optical-model potentials evaluated at one-half the incident deuteron kinetic energy. The deuteron adiabatic potential is defined as

$$U_d(\vec{R}) = \frac{1}{D_0} \int \left\{ U_n(\vec{R} + \frac{1}{2}\vec{r}) + U_p(\vec{R} - \frac{1}{2}\vec{r}) \right\} V_{pn}(\vec{r}) \phi_d(\vec{r}) d\vec{r} \tag{2.12}$$

where U_n and U_p are the neutron and proton optical potentials at one half the deuteron bombarding energy, $\vec{R}$ is the coordinate of the deuteron center of mass and $\vec{r}$ is the relative coordinate between proton and neutron, V_{pn} is the interaction between proton and neutron, $\phi_d(\vec{r})$ is the deuteron wave function, and D_0 is defined in Equation 2.9.

2.2.2 Global optical model potential

Instead of obtaining parameters for each individual nucleus separately, a global set of parameters can be obtained by fitting a group of nuclei at various energies. This is made possible by the fact that the parameters of the optical potential usually vary smoothly with energy and are similar for neighboring nuclei. The local optical-model potential for nucleon-nucleus scattering can be written in the Woods-Saxon form [13]:

$$\begin{aligned} U(r) = -V_r f(r, R_V, a_V) - iW_v f(r, R_W, a_W) + 4iW_s a_w \frac{d}{dr} f(r, R_W, a_W) \\ +2(V_{so} + iW_{so})(\frac{1}{r}\frac{d}{dr} f(r, R_{so}, a_{so}) L \cdot \sigma) + V_c \end{aligned} \tag{2.13}$$

where $f(r, R, a) = \frac{1}{1+exp\left[\frac{r-R}{a}\right]}$ and $V_c = \begin{cases} \frac{Z_a Z_b e^2}{r}, & r \geq R_c \\ \frac{Z_a Z_b e^2}{2R_c}(3 - \frac{r^2}{R_c^2}), & r < R_c \end{cases}$
and where R and a are nuclear radius and diffuseness; V and W are the depths of the real and imaginary potential, in which the subscripts r, s, so and c correspond to volume term, surface term, spin-orbit and Coulomb, respectively. L represents the orbital angular momentum operator of relative motion of the scattered particle and σ represents the spin operator. R_c is the radius of nucleon charge distribution, considered to be at a constant density for $r < R_c$.

Optical potential parameters for transfer reactions can be obtained from elastic scattering data. However, with rare-isotope beams this approach has practical limitations, such as lack of data with a broad range of energies and nuclei that are necessary for systematic studies and the lack of beamtime for elastic scattering with radioactive beams. In order to circumvent these difficulties, one can use global optical potentials that are in general independent of the energy and nuclei. Global optical potentials are determined from fitting experimental data over a wide range of nuclei and their energies. An optical-model potential that has gained wide usage is discussed in the following section.

2.2.3 Chapel-Hill 89

Chapel-Hill 89 (CH89) is a parametrization of the nucleon-nucleus optical-model potential based on data for nuclear mass range $A = 40-209$ and nucleon laboratory energy range $E = 10-65$ MeV [43]. CH89 parametrization is determined based on the current understanding of the basis of optical potential, such as folding model and nuclear matter approaches. It is based on an extensive database of nearly 300 proton and neutron differential cross sections and analyzing-power angular distributions. Parameter uncertainties and correlations between parameters are estimated. The parametrization of the CH89 optical-model potential is summarized in Equations (2.14-2.17) and the parameters of CH89 are listed in Table 2.1. It has been shown that compared to other global optical potentials, the CH89 potential is well suited for description of the (d,p) experimental data [44, 45].

$$V_r = V_0 \pm V_t \left(\frac{N-Z}{A}\right) + (E - E_c)V_e \tag{2.14}$$

$$V_c = \begin{cases} \frac{6Ze^2}{5R_c} = \frac{1.73}{R_c} MeV, & \text{for protons} \\ 0, & \text{for neutrons} \end{cases} \tag{2.15}$$

$$\begin{aligned} R_V = r_V A^{\frac{1}{3}} + r_V^{(0)} \quad &, \quad R_W = r_W A^{\frac{1}{3}} + r_W^{(0)} \\ R_{so} = r_{so} A^{\frac{1}{3}} + r_{so}^{(0)} \quad &, \quad R_c = r_c A^{\frac{1}{3}} + r_c^{(0)} \end{aligned} \tag{2.16}$$

$$\begin{aligned} W_v &= \frac{W_{v0}}{1 + exp\left(\frac{W_{ve0} - (E - E_c)}{W_{vew}}\right)} \\ W_s &= \frac{W_{s0} \pm W_{st}\left(\frac{N-Z}{A}\right)}{1 + exp\left(\frac{(E - E_c) - W_{se0}}{W_{sew}}\right)} \end{aligned} \tag{2.17}$$

2.3 Energy dependence of Transfer Reactions

In order to extract meaningful information about the structure of a nucleus, in our case ^{56}Ni, the (p,d) or (d,p) transfer reactions have to take place in the appropriate range of center of mass energies. At low energies, the cross section is Coulomb-dominated, while at high energies ($\gtrsim$100 MeV) the *angular momentum mismatch* (the difference in angular momenta of the entrance and exit channel) is considerable, reducing the cross section and washing out the characteristic effects of nuclear-surface interactions [13]. Macefield et al. [46] computed cross sections for (d,p) reactions involving heavy nucleus ^{238}U and concluded that (d,p) reactions are best studied at deuteron incident energies of 20-25 MeV. This is because the reactions are Coulomb-dominated at low energies and have forward peaked cross sections

Table 2.1: Parameters of the global nucleon-nucleus optical potential for CH89

Parameter	Value	Uncertainty
V_0	52.9 MeV	±0.2
V_t	13.1 MeV	±0.8
V_e	-0.299	±0.004
r_0	1.250 fm	±0.002
$r_0^{(0)}$	-0.225 fm	±0.009
a_0	0.690 fm	±0.006
r_c	1.24 fm	-
$r_c^{(0)}$	0.12 fm	-
V_{so}	5.9 MeV fm^2	±0.1
r_{so}	1.34 fm	±0.03
$r_{so}^{(0)}$	-1.2 fm	±0.1
a_{so}	0.63 fm	±0.02
W_{v0}	7.8 MeV	±0.3
W_{ve0}	35 MeV	±1
W_{vew}	16 MeV	±1
W_{s0}	10.0 MeV	±0.2
W_{st}	18 MeV	±1
W_{se0}	36 MeV	±2
W_{sew}	37 MeV	±2
r_w	1.33 fm	±0.01
$r_w^{(0)}$	-0.42 fm	±0.03
a_w	0.69 fm	±0.01

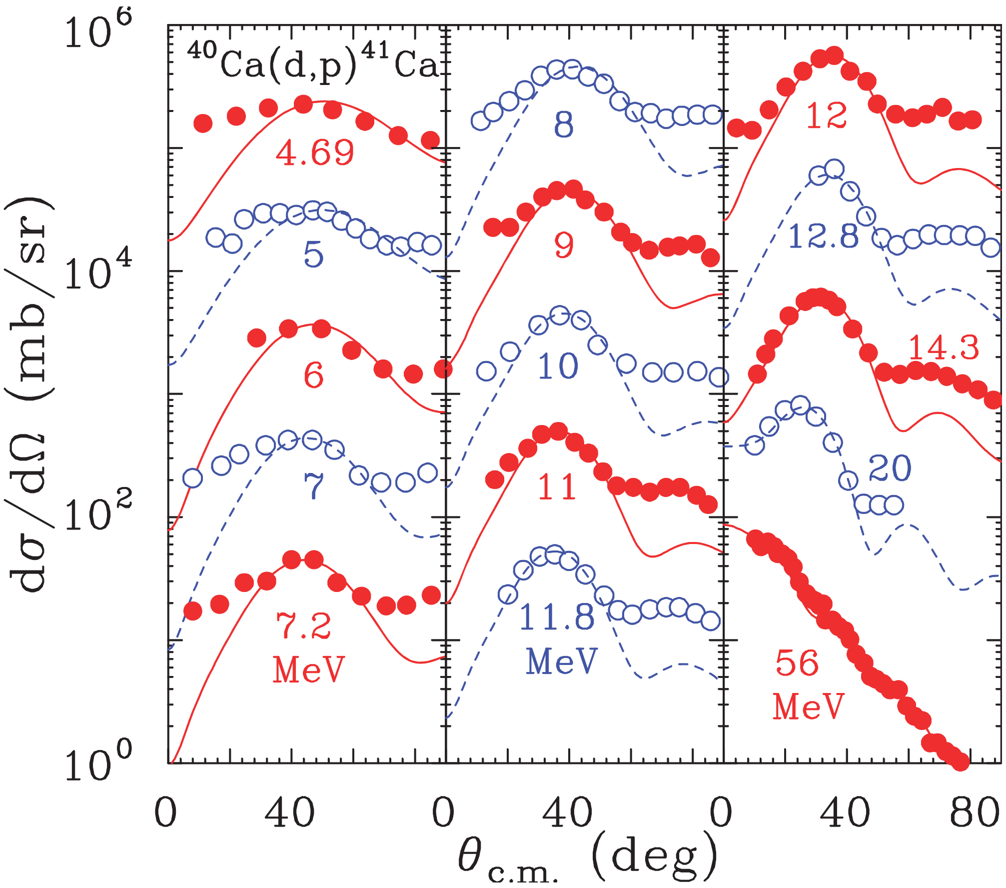

Figure 2.1: Angular distributions for ^{40}Ca(d,p)^{41}Ca reactions for beam energy from 4.69 to 56 MeV total energy. Each distribution is displaced by factors of 10 from adjacent distributions. The overall normalization factor is 10 for the 7.2 MeV data. References are listed in Ref. [47].

at high energies. At both extremes of the energy range it becomes difficult to distinguish ℓ values. For lighter target nuclei, Lee et al. have compared the angular distributions of protons emitted from the ^{40}Ca(d,p)^{41}Ca (g.s) reaction from E_d=4.7 to 56 MeV, as demonstrated in Figure 2.1. Better agreement is found for ground state transfers at incident energies of around 10-20 MeV. At 56 MeV energy, the sensitivity to ℓ is lost. Only one angular distribution is shown at each incident energy. Comparing these two conclusions, the stronger Coulomb potentials for heavy ions shift the best range of incident projectile energies upward by about 5 MeV.

The projectile incident energies discussed above pertained to the stripping (d, p) reactions, that are equivalent to pick-up (p,d) reactions under the time-reversal reciprocity assumption. However, the energy considerations in the entrance channels are different for these transfer reactions. Typical stripping reactions are exothermic, with a Q-value of 14.41 MeV for the ^{55}Ni(d,p)^{56}Ni reaction, whereas typical pick-up reactions are endothermic, with a Q-value of -14.41 MeV (exactly the negative of the former) for the equivalent ^{56}Ni(p,d)^{55}Ni reaction. This is in part due to large excess mass of the deuteron (13.135 MeV). If we assume a best range of deuteron incident energies of 10-25 MeV according to considerations in the previous paragraph, the proton energies in the exit channel are in the range of 25-40 MeV. Because of the equivalence of entrance and exit channels under time-reversal, we can expect that best range for proton incident energy in the ^{56}Ni(p,d)^{55}Ni reaction is 25-40 MeV. Below 25 MeV, the cross section will be suppressed due to lack of available energy in the exit channel (<10 MeV). Even in the best range of incident energies the variance in cross section is significant. As demonstrated in Figure 2.2, the cross section for the ^{56}Ni(p,d)^{55}Ni reaction decreases more than twice when the incident proton energy is lowered from 37 MeV to 27 MeV. Also shown in the figure are the differential cross sections for 47 MeV and 87 MeV proton energies, which is outside of our best range. The angular distribution for these energies already shows the effects of high energy in the form of a peak at 0 angle. At 87 MeV, it becomes difficult to distinguish ℓ values, and one sees shoulders instead of peaks in the angular distribution. Also, a different set of optical model parameters may be necessary for energies above 65 MeV, because the proton energies used in elastic scattering fitting for the widely used global optical-model are lower than 65 MeV. Coupled with the availability and quality of beam at the range of interest, 37 MeV relative energy of the proton and the ^{56}Ni nucleus that was used in the present experiment is reasonable.

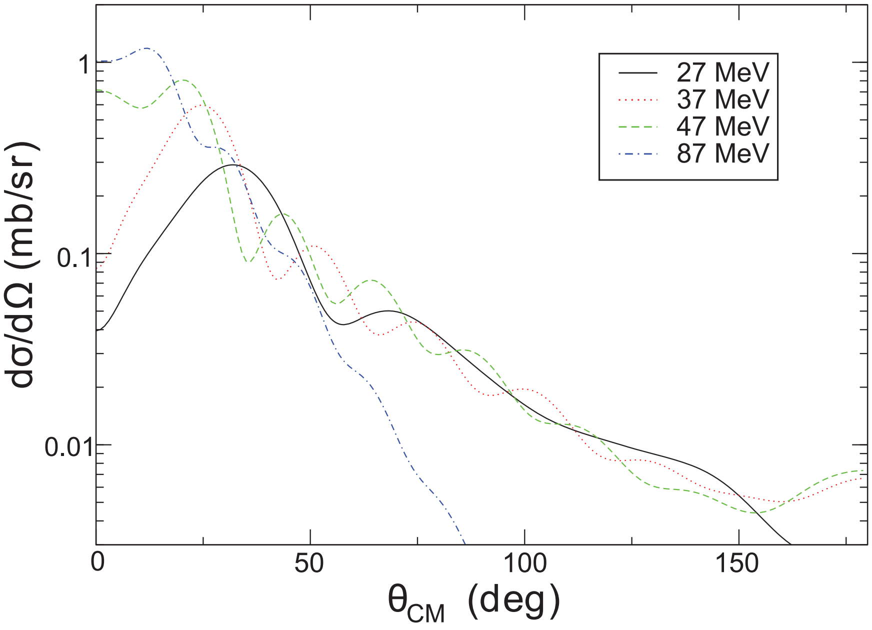

Figure 2.2: Calculated differential cross sections of the ^{56}Ni(p,d)^{55}Ni reaction at different energies. The solid black, dotted red, dashed green, and dot-dashed blue lines correspond to incident proton energies of 27, 37, 47 and 87 MeV, respectively.

2.3.1 Angular Momentum Matching

For the ^{56}Ni(p,d)^{55}Ni reaction, with ground state ^{55}Ni final nucleus, the angular momentum ℓ of the tranferred neutron is 3. Even though it is not a requirement [48], it would be desirable to have the angular momentum mismatch between the incoming proton and outgoing deuteron to be close to this ℓ value, i.e. between 2 and 4. For an estimated radius of 4.56 fm for ^{55}Ni, the angular momentum of the incoming 37 MeV proton is 6.41 $\hbar$. The angular momentum of the outgoing 22 MeV deuteron is 5.92 $\hbar$. The angular momentum mismatch L is the difference of those values, equal to 0.48 $\hbar$. This is outside of the desired range of the angular momentum mismatch, but 37 MeV is still reasonable because of sufficiently large cross sections and clearly distinguishable peaks in the angular distribution. This small angular mismatch of 0.48 $\hbar$ is actually in favor of l values 0 and one. Therefore, if there are excited states in ^{55}Ni with neutron angular momentum of 1 or 2, their cross sections will likely be enhanced.

2.4 Method for Extraction of Spectroscopic Factors

2.4.1 Input Parameters in Reaction Model

To take into account the breakup of the deuteron in the exit channel, we use the Johnson-Soper adiabatic approximation [42] of the full many-body system by a three-body system consisting of a neutron, a proton, and an inert core. The core would be the ^{55}Ni nucleus in the present study. In the place of the phenomenological deuteron optical potential, one can fold proton- and neutron-optical model potentials (CH89) [43] to form the deuteron optical potential. This folded deuteron potential is used in the ADWA calculations and corrects the effects of the deuteron breakup in the field of the core nucleus. The adiabatic approximation has been shown to describe the elastic scattering of 21.6 MeV deuterons from Ni well [42]. This deuteron energy is approximately the same as the deuteron energy in the center of mass frame in the exit channel of the ^{56}Ni(p,d)^{55}Ni of the present experiment, therefore it should give a very good account of the breakup effect in the reaction of interest.

We used a modified version of the code TWOFNR (University of Surrey version) in our transfer reaction calculations [49], mainly for convenience of use. With the same input parameters, TWOFNR predicts the same cross sections as do the calculations from two other widely used reaction model codes, DWUCK5 and FRESCO [44, 50, 51]. In this code, as well as in the other often used DWBA codes mentioned above, the detailed balance between pick-up (p,d) and stripping (d,p) reactions with reversion of the entrance and exit channels is preserved. The calculations use the local energy approximation (LEA) for finite-range effects [41] using the zero-range strength (D_0^2 =15006.25 MeV fm^3) and range parameter (β=0.7457 fm) of the Reid Soft core ^{3}S$_1$-^{3}D$_1$ neutron-proton interaction [52].

The spin-orbit coupling is not included in the calculations, because it has been shown that it has less than 10 % effect, and to be consistent with other calculations [44, 53]. For the ^{56}Ni(p,d)^{55}Ni reaction ending in the ground state of ^{55}Ni, the effect is approximately 10%, as demonstrated in Figure 2.3. The solid black and dashed red lines correspond to calculations with and without taking into account the spin-orbit term, respectively. Nonlocality corrections [40] with range parameters of 0.85 fm for the proton channel and 0.54 fm for the deuteron channel are used.

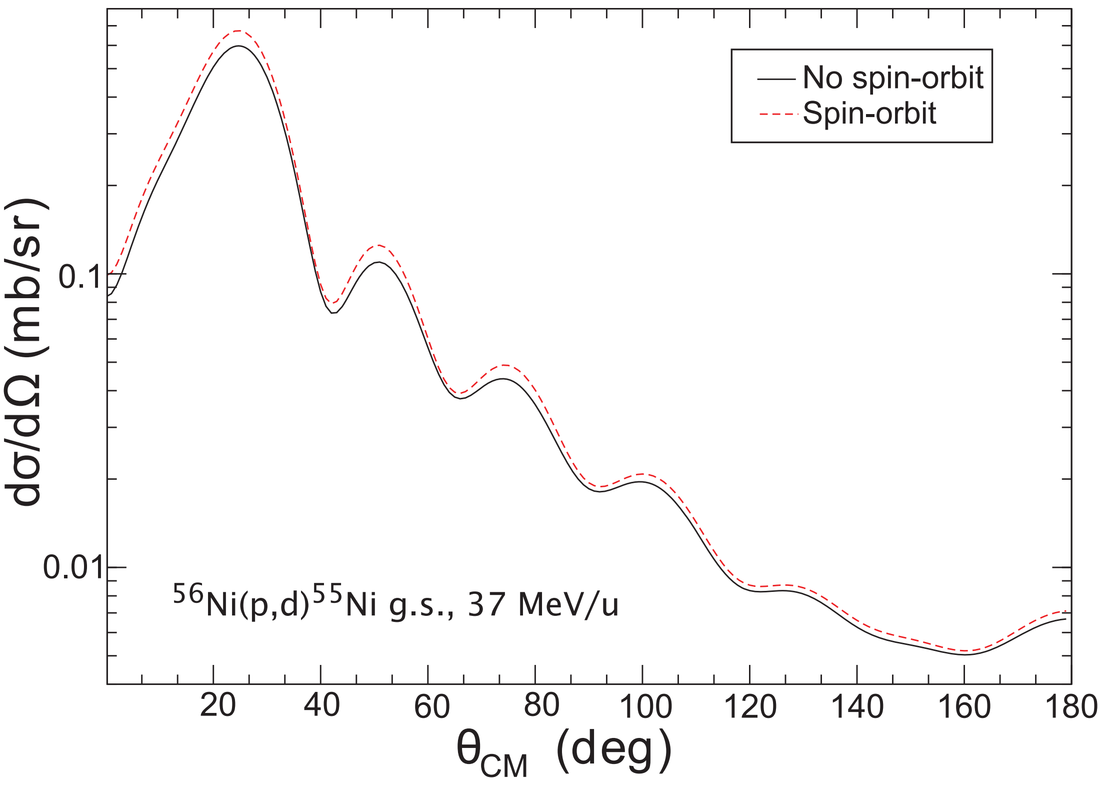

Figure 2.3: TWOFNR calculations of ^{56}Ni(p,d)^{55}Ni reaction at 37 MeV/u. The solid black and dashed red lines correspond to calculations with and without taking into account the spin-orbit term, respectively.

2.4.2 Extraction of Spectroscopic Factors from Transfer Reactions

Following the procedures in place for several decades, the spectroscopic factor is extracted by fitting the reaction model calculations to the data at the first peak of the differential cross section. This is done because the backward angles data are more sensitive to the effects of inelastic couplings and other higher-order effects, and agreement between the calculations and the measurements is not very good at the minima of the differential cross sections. To be consistent, the spectroscopic factors are extracted by minimizing χ^2, including only angular points that are within 30% of the maximum yield at the predicted angle of the first peak. The angular momentum ℓ values can be determined from the angular distributions. Thus, it is important to have the accuracy and statistics in absolute cross section measurements near the peak.

Chapter 3

Experimental Setup

3.1 Introduction

As explained in Chapter , measuring the neutron spectroscopic factor of symmetric doubly-magic nucleus ^{56}Ni by means of a (p,d) transfer reaction provides an important benchmark of the shell model for nuclei in the vicinity of this isotope. Transfer reactions can have large enough differential cross sections that measurements can be feasible with low beam intensities. Traditionally transfer reactions are measured in “normal kinematics”, in which the beam, consisting of light particles such as protons, impinges upon the target containing the heavy nuclei. However, ^{56}Ni is a radioactive isotope that turns into ^{56}Co by means of electron capture with a lifetime of 6.1 days, emitting gamma-rays in the process. ^{56}Co in turn beta-decays into stable ^{56}Fe with a half-life of 77.3 days. Thus, it is not viable to have a ^{56}Ni target, because of its lifetime, as well as its intense radioactivity.

These problems can be circumvented by the “inverse kinematics” technique. In inverse kinematics, the roles are reversed; the beam consists of heavy radioactive isotopes, whereas the target contains the light isotopes, such as hydrogen, deuterium or helium. In this experiment, the heavy radioactive beam and light target nuclei are ^{56}Ni and protons, respectively.

In this chapter, the method of measurement and experimental design are discussed in Section 3.2. The description of the detector systems, namely HiRA, S800 and MCPs will be found in Sections 3.3, 3.4, 3.5, respectively. The method of position measurement are discussed in Section 3.7. Description of the data acquisition and electronics system for the present experiment is included in Section 3.8.

3.2 Experimental Design

3.2.1 Reaction Target

As our target nuclei are protons, we had to make a compromise in choosing the target material. Ideally, we would like to use a solid or liquid hydrogen target, since using a gas hydrogen target of reasonable thickness does not provide sufficient number of nuclei per unit area. However, there are technical challenges involved with solid and liquid hydrogen. It is difficult to obtain a uniform hydrogen target with the desired thickness of approximately 1.3 mg/cm^2, corresponding to the same number of protons per square centimeter as the target used in the present experiment. If the target is too thick, the energies of the beam, ejectile and recoil particles decrease, and the energy loss in the target causes the energy resolution of the measurements to deteriorate. Also, if there are entrance and exit windows to contain such targets, the effects of reactions in window materials have to be taken into account. Taking these practical issues, the costs and benefits into account, we made a compromise in choosing the target material. We chose a plastic alternative, $(CH_2)_n$ polyethylene, which contains 2/3 hydrogen and 1/3 carbon atoms by numbers, or 1/7 hydrogen by mass. It is available with a wide range of thicknesses and good uniformity. The main drawback is that for the same number of hydrogen atoms per unit area, the energy loss of the beam particles per unit length is greater by almost factor of 3. If the target thickness is constrained by the energy resolution of the experiment, this puts a limit on the effective thickness of the target that is almost three times lower than the same limit for the solid/liquid hydrogen target.

3.2.2 Method of Measurement

The ^{56}Ni(p,d)^{55}Ni experiment was performed at the National Superconducting Cyclotron Laboratory at Michigan State University with a secondary ^{56}Ni beam energy of about 37 MeV/nucleon. The choice of the beam energy is explained in Subsection 3.2.3. We used the High Resolution Array, HiRA [54], to measure the energies and angles of the emitted deuterons. The deuteron energies and angles were used to identify the states populated in the final nuclei. The forward going recoil residues were detected in coincidence with the deuterons in the S800 spectrograph [55, 56]. This coincident and kinematically complete measurement of the deuteron and the recoil residue ensures that both particles originate from the ^{56}Ni(p,d)^{55}Ni reaction and not from some other reaction on the ^{12}C nuclei in the CH_2 target.

Due to the considerable size of the secondary beam spot in our experiment, two microchannel plate (MCP) detection systems [57,58] with thin carbon foils were employed to track the positions of the incoming beams and correct the deuteron angles for the beam positions and angles at the target [59].

Figure 3.1 summarizes the designed experimental setup. The HiRA array with 16 telescopes was placed at 35 cm from $(CH_2)_n$ reaction target. The design of this configuration is further explained in Subsection 3.2.4. The two MCP foils were positioned at 10 cm and 60 cm upstream of the reaction target. The MCP closest to the target also monitored the absolute beam intensities throughout the experiment for the overall normalization of the deuteron cross sections. The MCP's are discussed in more detail in Section 3.5. The HiRA, MCP and reaction targets were placed in the S800 scattering chamber in front of the S800 spectrometer.

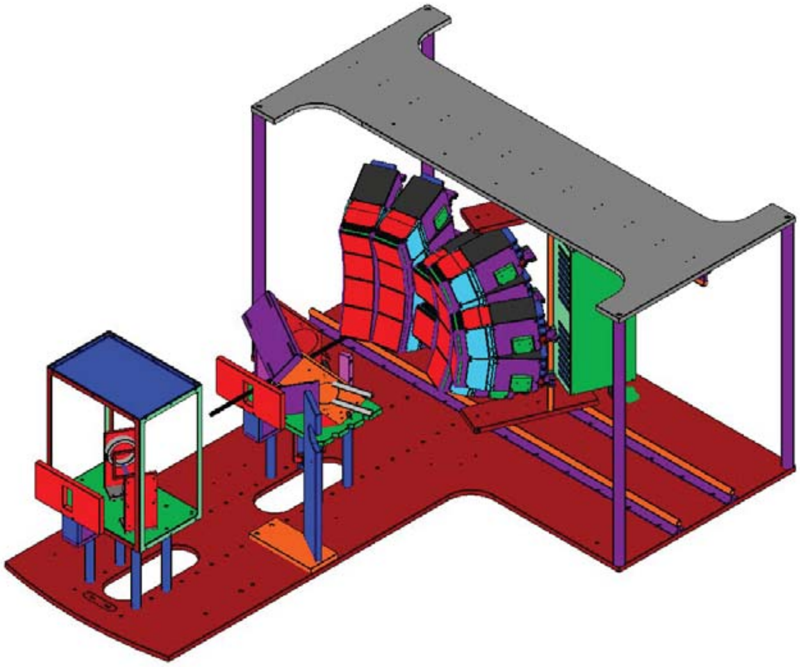

Figure 3.1: Simplified schematic diagram of the designed experimental setup inside the S800 chamber.

3.2.3 Beam Production

Rare isotopes are produced at the Coupled Cyclotron Facility (CCF)of the NSCL by the in-flight fast fragmentation method. The CCF consists of two superconducting cyclotrons, the K500 and the K1200 [60–62]. The process of beam production starts with insertion of stable ^{58}Ni into the *electron cyclotron resonance* (ECR) ion source. Stable or sufficiently long lived isotopes are delivered from the ECR as positively charged ions and injected into the central region of K500 cyclotron. An overhead view of the CCF is given in Figure 3.2.

The advantage of the CCF is that the K500 can accelerate isotopes with low charge states (ions with low total charge), thus enabling high output of ions from the ECR, as well as higher output of accelerated primary beam particles [63]. The ions are then accelerated

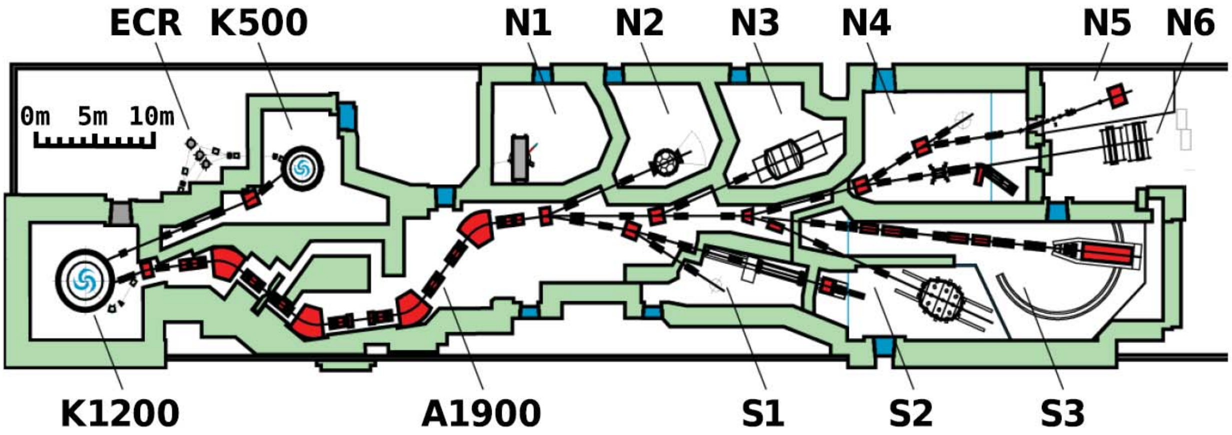

Figure 3.2: Coupled cyclotron facility of the NSCL [ISF]. The nickel beam starts in the ECR, is accelerated in the K500 and K1200 cyclotrons, fragmented, separated in the A1900 and transported to the experimental vault in S3.

up to 14 MeV/u in the K500 cyclotron, and delivered to K1200. At the energy of 14 MeV/u, most or all of the remaining electrons on the ions are stripped off by the stripper foil located in the first dee of the K1200 cyclotron. This high *charge state* enables the ^{58}Ni ions to reach higher energies due to stronger interaction with the electric and magnetic fields inside the K1200. Subsequently they are accelerated up to energies of about 140 MeV/u and extracted using a high voltage deflector.

The primary beam impinges upon a production target made of 1269 mg/cm^2 ^{9}Be as it leaves the extraction line. Then, the ^{58}Ni isotopes in the primary beam collide with beryllium nuclei in the target, producing a wide range of isotopes. To select the radioactive nuclei of interest after fragmentation, the A1900 large acceptance fragment separator is employed [64]. A schematic diagram of A1900 fragment separator is shown as a part of the Coupled Cyclotron Facility in Figure 3.3. A 150 mg/cm^2 thick achromatic aluminum wedge degrader and momentum slits at the dispersive image of the separator were employed to degrade the secondary beams to 37 MeV per nucleon and further purify the beams, resulting in a ^{56}Ni beam with average purity of 70%. The contaminants in the beam consisted of mainly the unstable ^{55}Co and ^{54}Fe (nuclei with the same number of neutrons). The secondary ^{56}Ni beam was identified unambiguously by the time of flight from cyclotron to the A1900 focal plane, using the *radio-frequency* (RF) signal of the cyclotron and a scintillator at the extended focal plane of the A1900. A magnetic switchyard is used to deliver the secondary beam into the S800 vault for measurements.

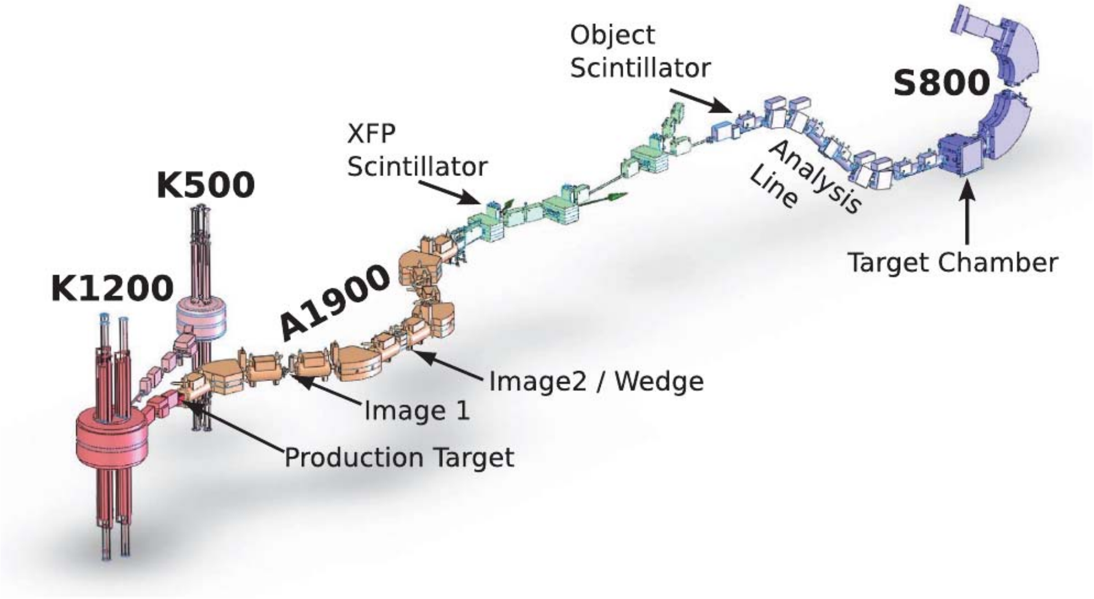

Figure 3.3: Schematic rendering of the coupled cyclotron facility, A1900 separator and the S800 spectrograph aligned with the scattering chamber and analysis beam line.

As discussed in Section 2.3, a good range of beam energies is 25-40 MeV/A. In this region, the differential cross sections are large enough and ℓ value of the transferred nucleon can be identified from the angluar distribution. The radioactive beam is produced at 120 MeV/A or higher, and its intensity generally decreases as the secondary beam energy is decreased by degrading with absorbers in the A1900 fragment separator. We performed our measurement at an energy of 37 MeV/A, which is within the good energy range. It was chosen because it provides a reasonable compromise between beam quality and count rate considerations.

The beam impinged upon a polyethylene $(\mathrm{CH}_2)_n$ target with a thickness of 9.60 mg/cm^2, which was chosen as a compromise between maximizing the cross-section yields and minimizing the energy loss and the angular and energy straggling of deuterons in the target.

3.2.4 Geometry of the HiRA Detector Array

As mentioned above, the deuterons emitted from the ^{56}Ni(p,d)^{55}Ni reaction are detected by the HiRA array. In inverse kinematics, the reaction is the same as in normal kinematics in the center-of-mass, however, the kinematics are quite different in the laboratory frame. One must understand these kinematics well in order to optimally use the HiRA array for the experiment. For example, one must know the location of the expected peaks of the differential cross section of the reaction of interest, ^{56}Ni(p,d)^{55}Ni .

For the reaction of interest in inverse kinematics, all deuterons are emitted in the forward angles and any single angle in laboratory corresponds to two different deuteron energies and CM angles. This is illustrated by the following two figures. Figure 3.4 shows the center-of-mass angle θ_{CM} versus the laboratory angle θ_{lab} for a deuteron from the ^{56}Ni(p,d)^{55}Ni reaction in inverse kinematics with a beam energy of 37 MeV/u. As one can see, there is a maximum laboratory angle around 32 degrees. At smaller lab angles there are two different angles for each center-of-mass angle.

This can be understood by the velocity diagram for the deuteron displayed in Figure 3.5, where V$_{CM}$ is the velocity of the center-of-mass in the laboratory frame; V$_d^{Lab}$ and V$_d^{CM}$ are the deuteron velocity in the laboratory and center-of-mass frame. The corresponding laboratory and center-of-mass angles are θ_{lab} and θ_{CM} respectively. The circle represents the velocity of the deuteron in the center-of-mass frame. It can be seen from the figure that there's a maximum angle θ_{max}, in concordance with Figure 3.4.

Differential cross sections in the center-of-mass and lab frame, calculated using the

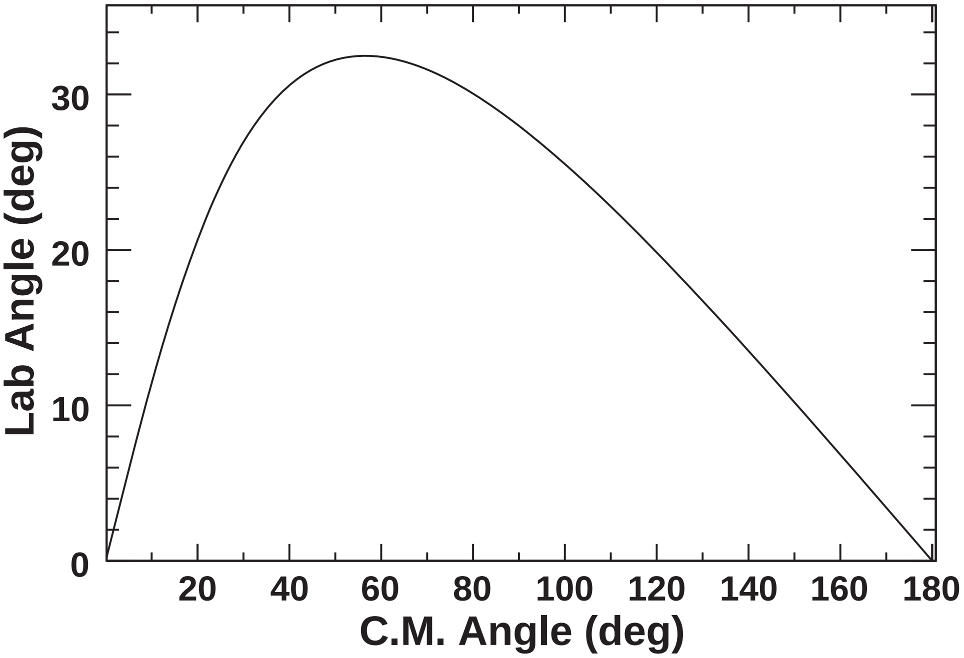

Figure 3.4: Laboratory angle vs. CM angle for a deuteron in the ^{56}Ni(p,d)^{55}Ni reaction.

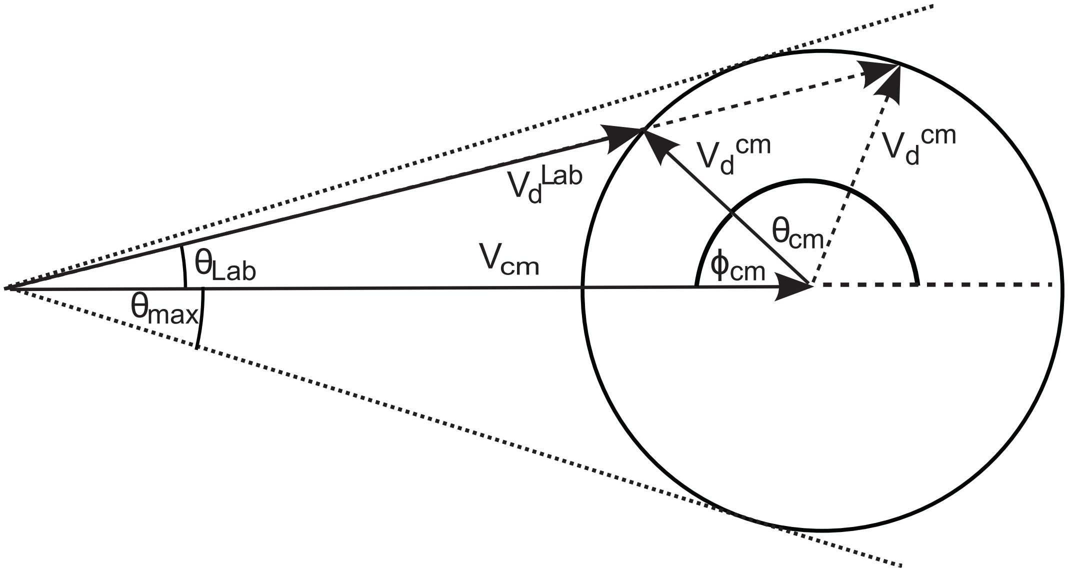

Figure 3.5: Velocity diagram for the (p,d) transfer reaction in inverse kinematics.

TWOFNR code [49] for the ground-state transfers for the ^{56}Ni(p,d)^{55}Ni reaction, are displayed in Figure 3.6.

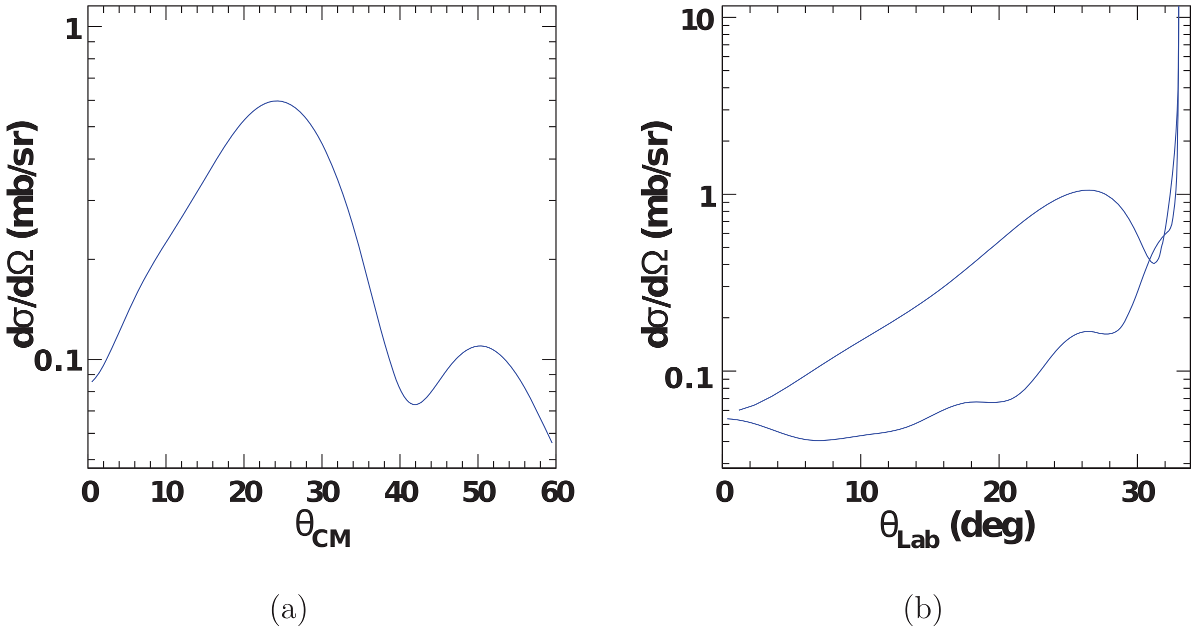

(a) (b)

Figure 3.6: The theoretical differential cross sections of the ^{56}Ni(p,d)^{55}Ni reaction for ground state transitions in c.m. frame (a) and in laboratory frame (b) at beam energy of 37 MeV/A.

In the left panel, theoretical differential cross section in the center-of-mass frame is displayed. The right panel shows the corresponding differential cross section in the laboratory frame. The deuterons that are emitted in backward angles in the center-of-mass also show up in forward angles in the laboratory frame, however, they have much higher energies and can be easily separated from the forward angle deuterons in the center-of-mass frame.

Based on the theoretical angular distribution of deuterons in the laboratory frame, an optimal configuration of the HiRA array was chosen. The coverage of the HiRA configuration as seen from the reaction target position is shown in Figure 3.7 in cartesian coordinates, as well as polar coordinates in Figure 3.8. Each telescope is assigned a number for reference. The red cross indicates the beam position.

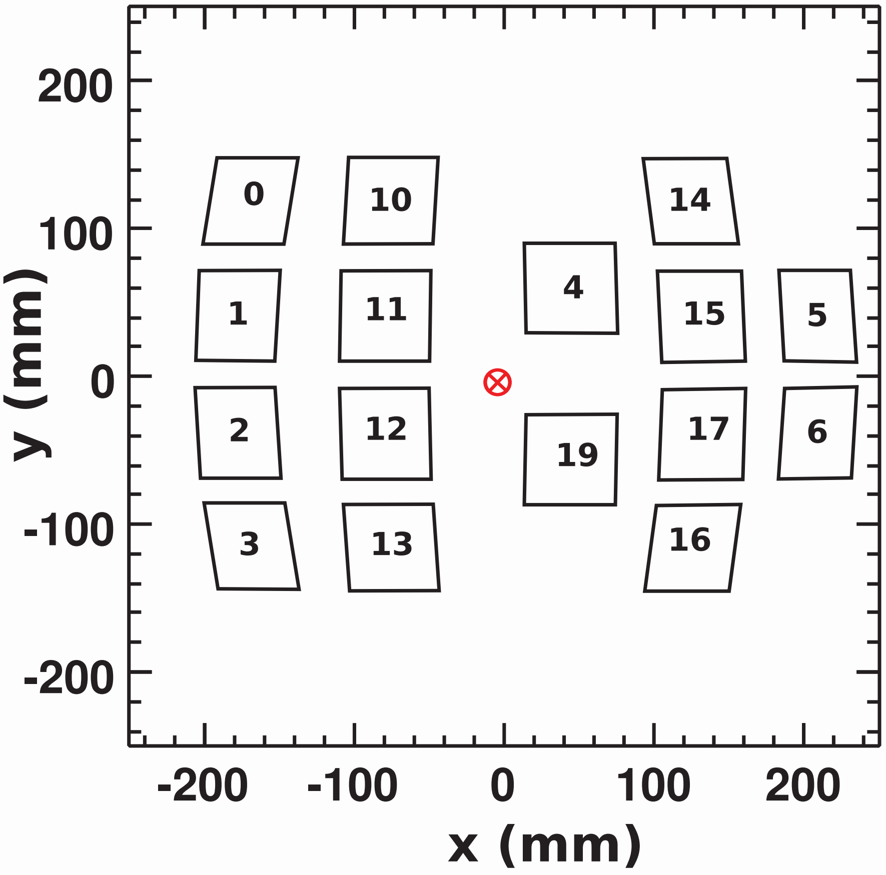

Figure 3.7: Beam's eye view of the outlines of the telescopes for the HiRA configuration projected on the X-Y plane. Telescopes are labelled by their numbers in the experiment. The beam position is at the red cross. Here the Z-axis is along the beam.

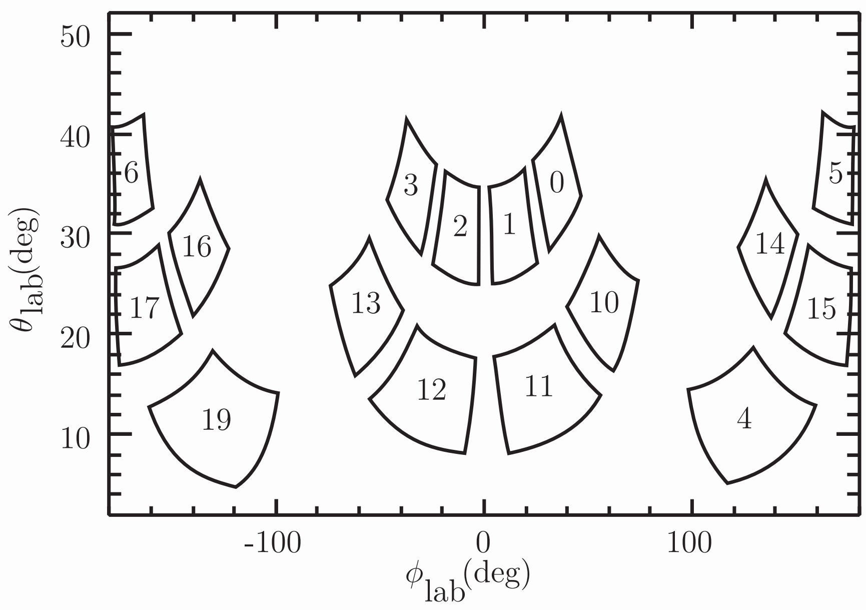

Figure 3.8: Beam's eye view of the HiRA configuration in spherical coordinates.

Figure 3.9 shows a photograph of the HiRA detector array and the upstream MCP. A total of 16 HiRA telescopes were arranged in four "towers" positioned at a radius of 35 cm from the reaction target and subtended polar angles of 5-45°. The gap at angles less than 5° allows the beam and heavy reaction fragments to exit the S800 chamber and continue on to the S800 spectrometer. Due to the forward focusing of the deuteron particles, this setup covers most of the important solid angles in the center-of-mass frame for the reaction of interest. The geometric efficiency of the HiRA array setup was calculated by a Monte Carlo procedure, the result is shown in Figure 3.10, approximately 30-40% coverage is achieved. In addition to a large geometric efficiency in the angular regions covering the first peak of the ground state at around 26° and an l=1 excited state at 2.089 MeV with a peak at around 12° in the laboratory frame, the design of the HiRA configuration also optimizes the angular resolution, which improves with the distance from the target. The granularity of the HiRA telescopes provides an angular resolution of ±0.16° in this setup where the target is located

35 cm away from the telescopes.

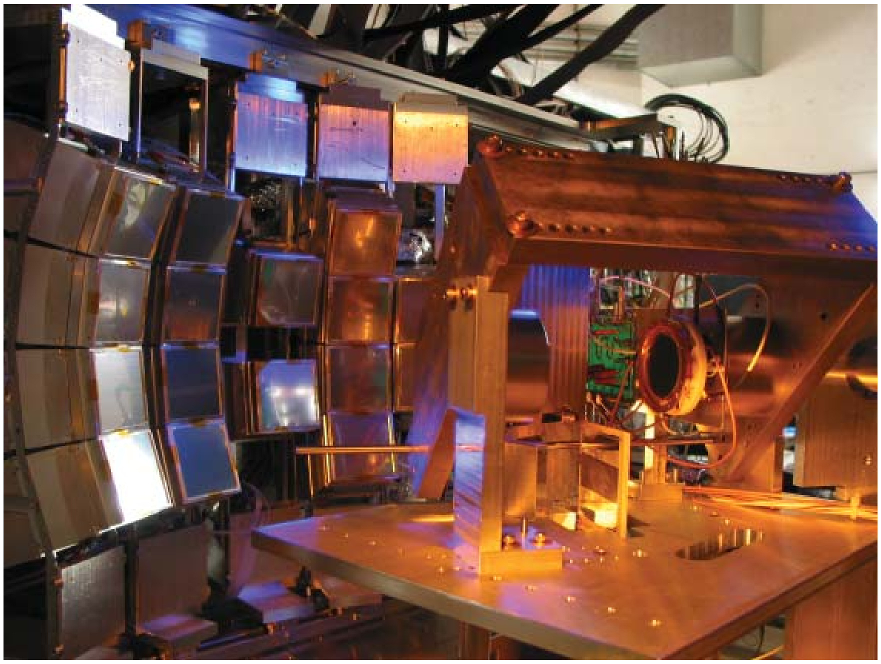

Figure 3.9: Photograph of the experimental setup.

3.3 HiRA (High Resolution Array)

The HiRA (High Resolution Array) is a modular set of 20 detectors, called “telescopes”, ideally suited for detecting and analyzing light charged particles [54]. The array covers a large solid angle and each telescope consists of highly segmented ΔE-E silicon strip detectors and a cluster of 4 CsI crystals. It can be configured in space to match the needs of a specific experiment, as in some examples shown in Figure 3.11. The silicon strip detectors have excellent energy resolution, and their granularity gives the array high angular resolution as well. A schematic view of a HiRA telescope is shown in Figure 3.12. Each telescope consists of a 65 μm single sided strip detector (SSSD) with 32 strips, a 1.5 mm double sided strip detector (DSSD) with 32 strips in the front and 32 strips in the back, and four 4 cm thick *thallium doped Cesium Iodide* (CsI(Tl)) detectors.

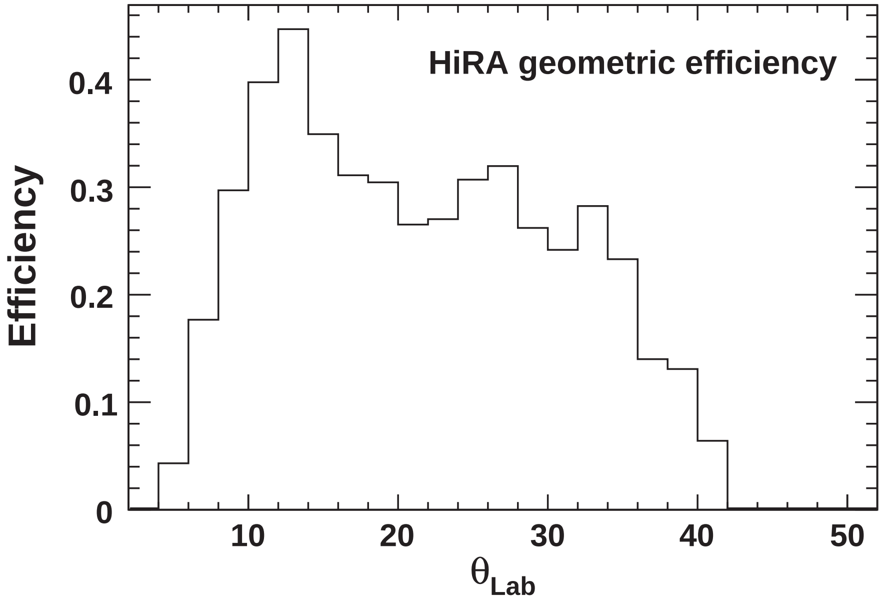

Figure 3.10: Geometric efficiency of the HiRA configuration.

The ΔE-E telescope technique is used for identifying isotopes that stop in the 1.5 mm DSSD, whereby the energy loss in the first thin ΔE layer is plotted against energy loss in the thick E layer where the particle is stopped. The energy loss in the ΔE detector is approximately proportional to Z^2A/E. Thus, in the ΔE-E plot each isotope will form a unique band. The ΔE-E technique is discussed in greater detail in subsection 4.2.7. It should be noted that the naming convention of the Si detectors is somewhat arbitrary, as for particles with higher energies, the thick DSSD is used as the "ΔE" layer and the CsI(Tl) as the "E" layer. Thin mylar foils (265 μg/cm^2), attached to aluminum frames, cover the fronts of telescopes and serve as Faraday cages. The telescopes are arranged into three columns of four telescopes to form three "towers". The remaining four telescopes combined into two columns form the fourth tower. In addition, each telescope has an ID tag associated with it. The positions of telescopes with the corresponding ID tags are shown in Figure 3.7.

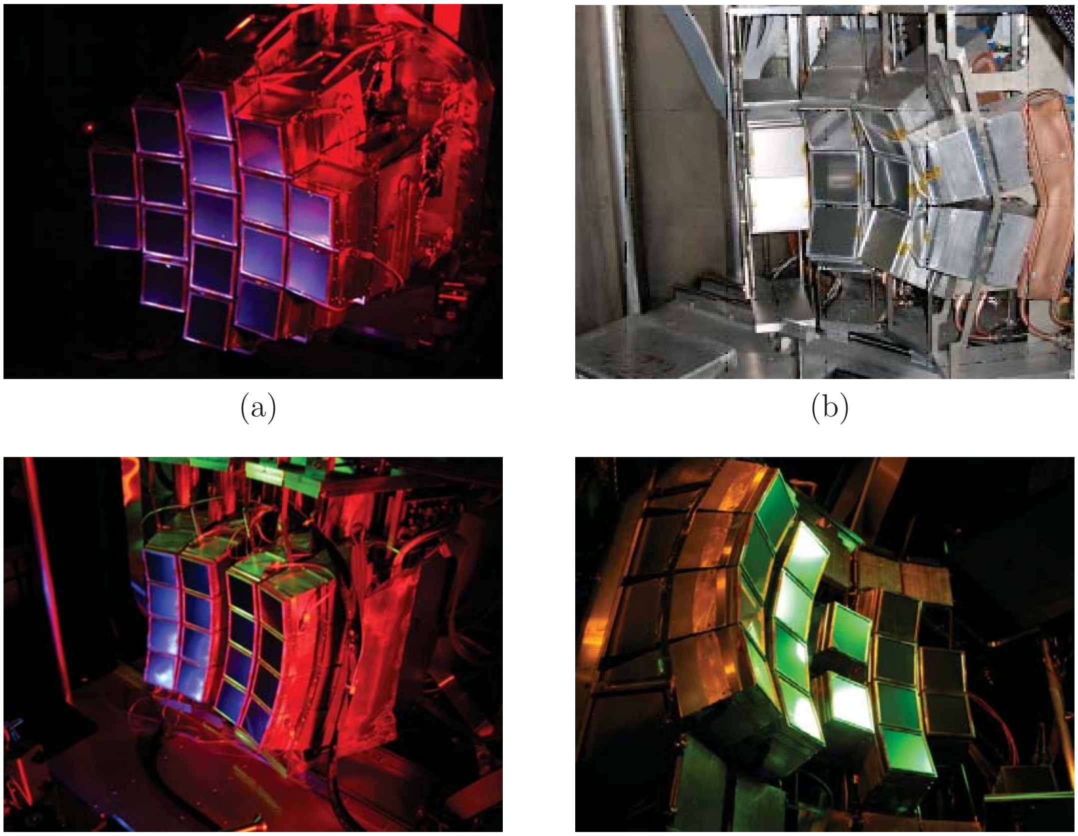
(a) (b)
(c) (d)

Figure 3.11: Photographs of HiRA configurations used in four different experiments, the bottom-right photograph (d) shows the configuration used in this experiment.

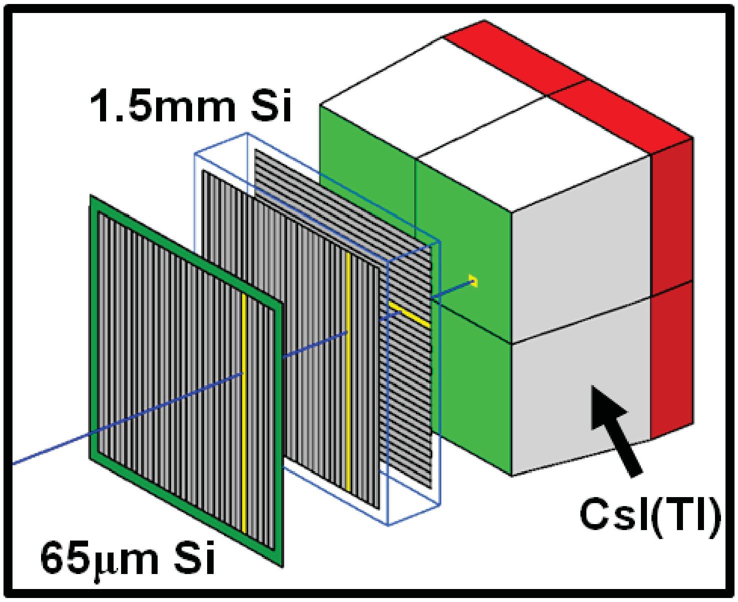

Figure 3.12: Schematic of a single HiRA telescope.

3.3.1 Silicon Strip Detectors

Si detectors are frequently used for charged particle detection [65]. At relatively lower energies of a few tens of MeVs, most particles punch through the thin ΔE detectors and stop in the thick DSSD E detectors, the Si detectors of the HiRA. The thin 65 μm single-sided ΔE Si detectors have thirty-two 2 mm vertical strips with a typical Full Width Half Maximum (FWHM) energy resolution of 55 keV. The thicker 1.5 mm double-sided Si detector, called E, has thirty-two 2 mm vertical strips in front and thirty-two 2 mm horizontal strips in the back with a typical energy resolution (FWHM) of 65 keV.

The passage of particles through semiconductor detectors generate electron-hole pairs that are used as information carriers. Semiconductors differ from metals and insulators by their electronic band structure, i.e. allowed and forbidden band energies. In general, electronic properties of materials can be understood in terms of a valence band and conduction band, as demonstrated in a simplified diagram, Figure 3.13. The valence band is the highest range of electron energies in which electrons are normally present and bound to specific lattice sites. The conduction band is the range of electron energies, higher than that of the valence band, sufficient for electron to move freely within the atomic lattice of the material. In metal conductors these two bands overlap, supplying the conduction band with mobile electrons. In a semiconductor such as silicon, the forbidden region, or band gap, between these two bands is small compared to an insulator band gap. Charged particles that traverse such a material excite electrons into the conduction band and create holes in the valence band. An electric field is applied to the silicon and these electrons and holes drift to the opposite sides of the silicon detector. One collects charge signals that are proportional to the energy deposited by the particle. The front side of the silicon detector is biased negatively

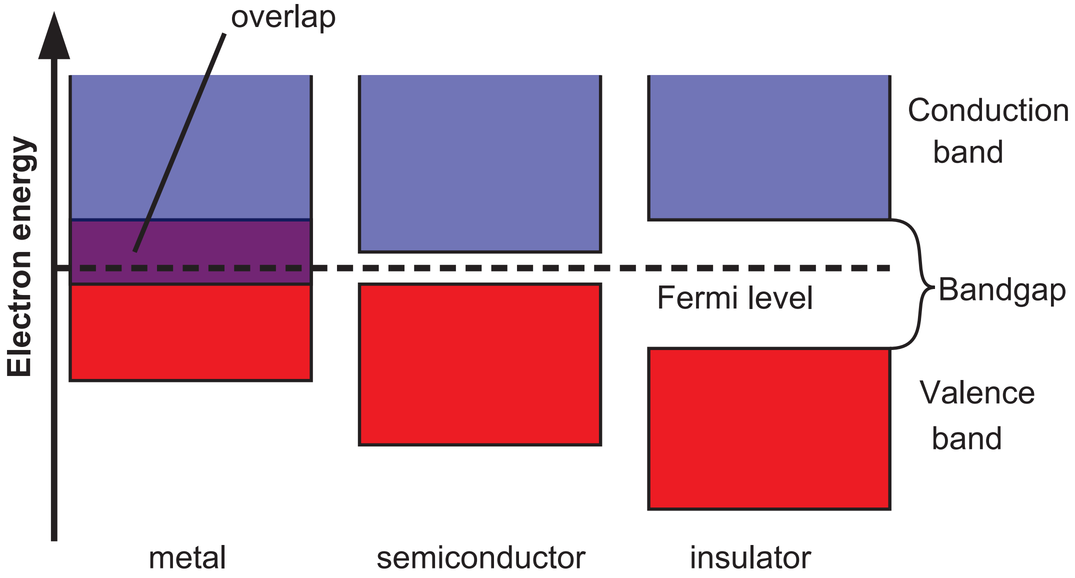

Figure 3.13: Simplified diagram of the electronic band structure of metals, semiconductors, and insulators. Credit: Pieter Kuiper.

and collects the positive holes, and the back side is biased positively and collects the negative electrons.

The HiRA Si strip detectors shown in Figures 3.14 and 3.15 consist of the silicon wafer, its G-10 frame, which supports the silicon, and the cabling from the silicon wafer to an external connector. The wafer is epoxied into the custom designed G-10 frame the details of which are described in [54]. A flexible 0.246 mm thick polyimide cable is used to carry the signals and bias the detectors. This cable is epoxied to the frame and coupled to the Si through wire bonds that are ultrasonically bonded to the strip surface on the wafer and to the electrode pads connected to the cable. When mounted in the telescope can, the signal cables run at a 90° angle to ridge of the frame. This allows the cable to go straight to a printed circuit board (PCB) at the back plane of the can which maps each of them to a 34-pin output connector. The 32 strips on Si surface connect to traces going to pins 2 through 33 of the connector. Pins 1 and 34 are used to connect the back plane of the single sided detector to the ground. On the double sided detector these pins do not connect to the silicon wafer.

Characteristics of semiconductors can be precisely controlled and the performance tailored through the use of impurity doping. Impurity doping is generally defined as being n-type or p-type. N-type impurities are sources of excess electrons which are more easily promoted to the conduction band than those electrons associated with the valence band lattice sites. P-type impurities are sources of excess holes. The HiRA Si strip detectors function as a p-n junction. The bulk silicon wafer is n-type material while the strip surfaces on the front (junction side) are p-type which have been created using a p+ ion implantation method. This forms the basis for the junction. Space charge generated at the interface of the p-n junction induces an electric field near the junction known as the depletion region [65]. Here, any electron-hole pairs that are created quickly migrate apart. Placing a reverse bias voltage across the junction results in the extension of the depletion region across the wafer. The result is that charge carriers migrate rapidly and are efficiently collected, generating a high quality signal. The HiRA Si detectors are operated as fully depleted detectors with typical operating voltages of 350 V. More detailed information including information on the performance of HiRA Si detectors, design, and testing methods can be found in references [66] and [54].

3.3.2 CsI Detectors

When the detected particle has relatively high energy, more than 15 MeV for protons or 21 MeV for deuterons, it will punch through the E detector and reach a CsI(Tl) crystal. The cluster of CsIs have trapezoidal shapes so that particles entering the crystals stay inside, without leaving the crystals through the side walls, if the target is 35 cm from the Si detectors assuming a point source. If the source is not at that center point, the particles might leave or enter the CsI crystals from the sides. If we imagine a long pyramid made out of CsI(Tl),

Figure 3.14: Photograph of a HiRA single-sided silicon strip-detector (ΔE) in a circular plastic container. The brown band extending outside the container is the signal cable.

Figure 3.15: Photograph of a HiRA double-sided silicon strip-detector (E) in a circular plastic container. The two brown bands extending outside the container are the signal cables.

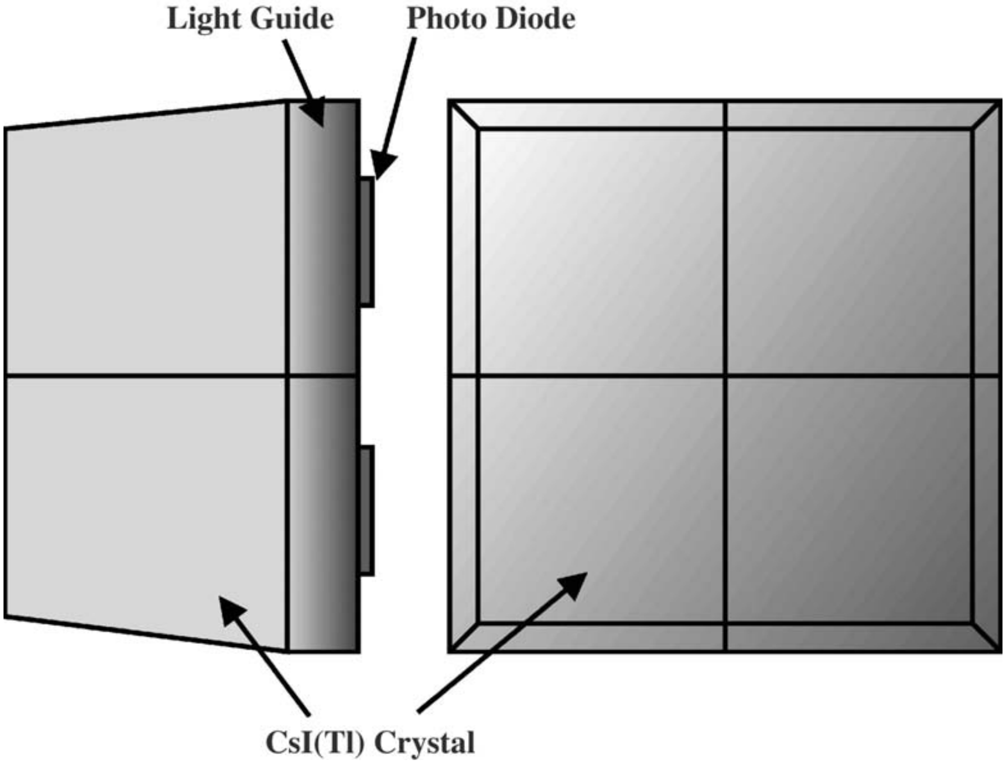

Figure 3.16: A schematic rendering of a HiRA CsI crystal cluster.

with the tip at the target position and base of 7.8x7.8 cm^2, and cut it 3.9 cm away from the base, then we have the shape of our cluster. The sides will be at 5.3° from the normal to the base. We then split it into four symmetric crystals for better granularity, and the inner sides of each crystal will be straight, as seen in Figure 3.16. Each one is 3.5x3.5 cm^2 in front and 3.9x3.9 cm^2 in the back, and 3.9 cm long. A 1.3 cm thick light guide is glued with silicon rubber to the back of each crystal, and covers the entire crystal. Attached behind the light guide is a 0.3 mm thick photo-diode with an active area of 18x18 mm^2. The thickness of the CsI(Tl) crystals is sufficient to stop protons up to ∼115 MeV, deuterons up to ∼150 MeV and alphas up to ∼465 MeV. The crystals are doped with thallium (Tl) to shift the CsI scintillation into the green region suitable for the use of photo diodes.

Thallium-doped CsI crystals are a cost-effective and widely used way of detecting energetic charged particles. They are not as vulnerable to humidity as Na(Tl) crystals and are easily machined into shapes, producing light with a spectrum that matches well with the readout of silicon photo-diodes [67]. However, response of CsI(Tl) to low energy protons has not been investigated well enough. In fact there is hardly any data in the region of E≤5 MeV [68].

A small fraction of kinetic energy loss (<10%) of a charged particle in CsI(Tl) is converted into fluorescent energy. The thallium in the CsI is in molar concentrations of the order of 0.1% [69]. In general, while the light output is caused by the competition between the radiative deexcitations of the thallium dopant ions in the CsI(Tl) crystal and the non-radiative deexcitation of the crystal by other decay modes, the ionization density of a specific ion dictates the amount of light produced [70]. A schematic diagram of a CsI(Tl) cluster is shown in Figure 3.16 [69].

3.4 S800 Spectrograph

Secondary beams produced using in-flight fragmentation method have a large emittance as a result of the compromise between beam quality and beam intensity. Therefore, it becomes necessary to track the particles both before and after the reaction. The S800 spectrograph addresses the need to identify beam-like reaction residues on an event-by-event basis.

A schematic diagram of the S800 spectrograph and its analysis line that comprise the S800 magnetic optical system is given in Figure 3.17. The analysis line consists of the beamline and 4 superconducting magnetic dipoles before the target position as well as 5 superconducting magnetic quadrupole triplets. The S800 spectrograph consists of a magnetic quadrupole doublet followed by two magnetic dipoles. Particle spectroscopy and identification of nuclear reaction products generated with secondary beams is enabled by the combination of the large acceptances of the S800 in both solid angle and momentum, and a high resolution focal plane detection system [55]. A reaction target is generally positioned at the pivot point of the S800, located in front of the entrance of a large bore quadrupole doublet. In the present experiment the target was placed upstream of this position by 0.53 m.

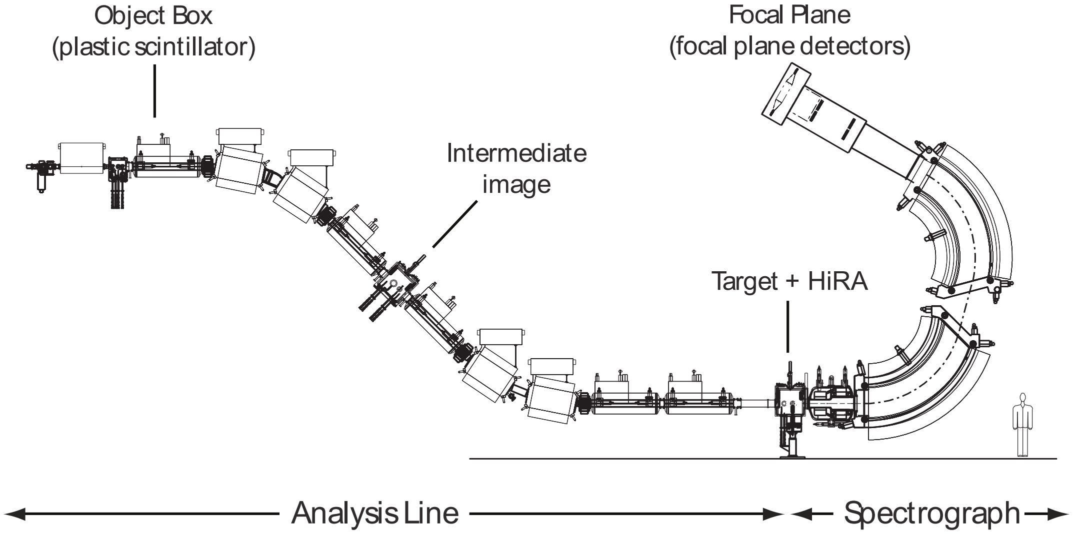

Figure 3.17: Schematic diagram of the S800 spectrograph aligned with the scattering chamber and analysis beam line.

The S800 has two possible optical modes of operation, dispersion matched and focused mode [56]. In dispersion matched mode all beam particles that start from a focused beam spot at the object come to a focused beam spot in the focal plane, i.e. the beam is tuned to an achromatic focus on the focal plane of the S800 spectrograph. This means the beam must be dispersed in both momentum and position at the target, with particles of higher momentum hitting higher spots on the target. This displacement is 10 cm/% of the momentum difference from the central momentum of the beam, resulting in a very large beam spot at the target position with the large momentum spreads typical of secondary beams of the CCF. In focused mode the image at the target is achromatic. In this configuration the beam particles are focused to a smaller beam spot at the target. This mode provides a worse momentum resolution at the focal plane due to a larger momentum acceptance, but on the positive side allows a large overall beam intensity. To keep the beam spot small and intensity high the S800 system was configured for focused mode for our experiment.

The central-ray or reference trajectory, which is the path taken by a particle with the same rigidity as that of the magnetic system, is an important concept in any beam optics system. The deviation from this central-ray of a reaction product with a known mass and charge, is used to reconstruct the reaction that occurred in the target and achieve the required energy and angular resolution. It should be noted that while the information about the direction of the reaction residue is provided by the focal plane detectors, the direction of the beam particle is provided by the MCP beam tracking system.

The focal plane box, shown in Figure 3.18, houses several detectors that are used for particle identification, measurement of total energy, reconstruction of a particle's momentum vector at the reaction target, as well as a determination of non-dispersive position at the interaction point on the target. Two position sensitive cathode readout drift chambers (CRDCs) measure the trajectory of the particle entering the focal plane and provide the information for the reconstruction of the angles, non-dispersive position and energy of the residue (see Subsection 3.4.1). A segmented ion chamber measures the energy loss for particles entering the focal plane and enables particle identification using the ΔE-ToF technique (see Subsection 3.4.2). Three successively thicker scintillators labeled E1, E2, and E3 at the end of the focal plane box measure energy loss/total energy and also provide timing and trigger information with E1 (see Subsection 3.4.3). To reconstruct momentum and partial position of the particles at the target from the quantities measured with the focal plane detectors, an analytical method is used (see Subsection 3.4.4).

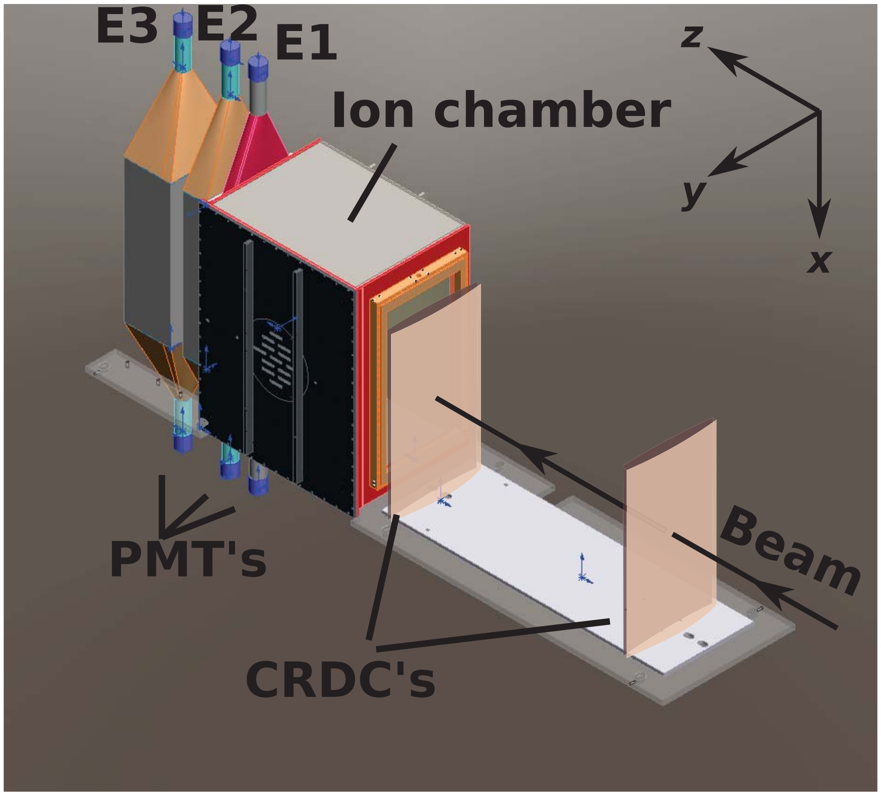

Figure 3.18: Schematic diagram of the S800 focal plane.

3.4.1 Cathode Readout Drift Chambers

When a reaction residue enters the S800 focal plane, it first goes through two Cathode Readout Drift Chambers (CRDC) detectors that are located 1 m apart and parallel to each other. The CRDCs are gas-filled, high-voltage, single-wire drift detectors with active areas of 30 cm x 59 cm. A mixture of 80% CF_4 (freon 14) and 20% C_4H_{10} (isobutane) at a pressure of 50 Torr is used as the drift gas. The position and angle information from the CRDC's are used as inputs for the inverse map, described in Section 3.4.4.

Particles going through the CRDC's ionize the gas in the chambers, and the electrons drift to the anode wires under constant electric field. The time of drift gives the Y-position corresponding to the non-dispersive plane, which is parallel to the magnetic field of the spectrograph. In the dispersive plane, which is perpendicular to the magnetic field, the

X-position is calculated using the distribution of charges on electrode pads of a CRDC. Each pad has a width of 2.54 mm and there are 224 of them in each CRDC. The signals from the pads are processed using front end electronics (FEE) chips developed by the STAR collaboration [71]. The position of the particle in the CRDC can be calculated using a Gaussian fit to the charge distribution on the pads. An alternative way of calculating the position is using the center of gravity of the induced charge distribution, which produces results that are practically identical to the ones with Gaussian fit method. In the analysis of this experiment, the center of gravity method was used, as it is procedurally easier than the Gaussian fit method.

3.4.2 Ionization Chamber

The S800 ionization chamber (also called ion chamber) measures the energy loss (ΔE) of particles that reach the focal plane. When combined with a measurement of a particle's time of flight (ToF), a particle can be identified based on its Z and A. The ion chamber is a standard Frisch grid ion chamber that is divided into 16 2.54 cm (1 inch) segments totaling 40.64 cm in length, with anodes perpendicular to the path of the ions. It is filled with a 300 Torr of 90% Ar and 10% CH4 (methane), a mixture commonly known as P10 gas. As a particle travels through the chamber, it loses energy by ionizing the gas. The gas ions then drift toward the anodes of the chamber and their signals are summed to provide the DE signal for the particle identification (PID).

3.4.3 Scintillation Detectors

In general, for trigger information and timing, as well as energy loss and total energy measurements, three plastic scintillators were used, labeled as E1, E2 and E3 with thicknesses of 5, 10 and 20 mm respectively. These scintillators are located towards the end of the focal plane. Signals collected by the photomultiplier tubes located on two ends of the scintillator were used to generate energy and timing signals.

All of the particles of interest (^{55}Ni, and for calibration purposes, ^{56}Ni), as well as other residues with similar mass and charge, are stopped in E1 scintillator, and the scintillator serves multiple purposes. It is used as the trigger for the S800 as well as providing a start timing signal for all of the time of flight (ToF) measurements. The drift times in the CRDCs, which provide the non-dispersive position information (see Subsection 3.4.1), are taken relative to the trigger generated by E1 as well.

3.4.4 Inverse Mapping

The position-sensitive Cathode Readout Drift Chambers measure the positions and angles of the particles at the focal plane of the S800 on both the dispersive and non-dispersive directions. This is important because the paths of the particles can be traced upstream to the target. Precise magnetic fields of the S800 magnets are used to calculate analytically a matrix called transfer map using the ion-optics code COSY INFINITY [72]. This transfer map is inverted to obtain an *inverse map*. The detailed description of this method can be found in reference [73]. The map converts the four focal plane position parameters measured at the CRDCs to the kinematics of the outgoing particle at the target. It is calculated to the fifth order in the focal plane parameters: dispersive position (x_{fp}), non-dispersive position

(y_{fp}), dispersive angle (a_{fp}), and non-dispersive angle (b_{fp}). The map calculates the angle of propagation out of the target (a_{ta}, b_{ta}) and the momentum deviation from the central track in the spectrograph (d_{ta}). The non-dispersive position at the target (y_{ta}) is calculated as well. Since the track of the particles through the spectrograph depends on their particular mass A and charge Q, an inverse map was calculated for each reaction channel.

3.5 Beam tracking with Micro Channel Plates

In this section, as well as in the section devoted to the analysis of MCP data, Section 4.4, we describe the performance of position sensitive MCPs of a design that was previously described by Shapira et al [57, 58]. One of the major difference between the present and the previous studies concerns the velocity of the beam ions being tracked; Shapira et al presented the position response for ions with $E/A \approx$1.4 MeV corresponding to $v/c = 0.055$ [57, 58]. Here, we investigate the response of similar detectors to ions with energies of up to $E/A \approx$72 MeV corresponding to $v/c = 0.4$. Since the scattered electron kinetic energies scale roughly with the incident kinetic energy per nucleon, which increases by a factor of ~ 50, consideration of the electron optics leads one to suspect that the MCPs may produce more diffuse images of the beam spot at high energies than at low energies; we document this in the present dissertation and compensate for such effects by increasing the magnetic field of tracking detector. In the following, we describe the MCP system used in our measurements and demonstrate its performance with both sources and beams. In addition, we demonstrate the practical use of the channel plate tracking detector in fast beam experiments by showing how it improves the resolution of experimental transfer reaction data.

Microchannel Plates are compact arrays of single channel electron multipliers [74]. In

MCPs, these electron multipliers are glass tubes with individual diameters of about 10 microns or less, that have been fused together in a hexagonal array and subsequently cut into wafers of a millimeter or less in length. The front and back surfaces of these wafers are coated with a conductive surface that allows a uniform bias to be applied across the MCP and consequently between the two ends of each tube or "channel" in the MCP. Electrons that enter a channel, strike the interior surface of the channel and produce secondary electrons that are accelerated down the channel and multiplied. The gain of such a channel depends on average number of hits inside the channel. This is governed by the ratio of its length to its diameter [75]. Progress in fabrication techniques has made it possible to scale this technology down to produce channels with diameters as small as 2 microns and lengths as short at 80 microns [76]. Depending on the channel design, gain factors up to 10^9 or more may be reached [74].

To achieve a higher gain, instead of using one microchannel plate, stability can be enhanced by stacking two MCPs in a chevron design as shown in Fig. 3.19. This was done for the MCP detector systems used in the present work. Each plate is cut to produce a bias angle of 8°. Stacking the plates serves two purposes. The first is to increase and saturate the gain of the system due to the larger number of multiplication steps. The second is to reduce positive ion feedback by preventing any ions that are generated at the output end of the channel from flowing back toward the input end and producing after pulses. In many MCP designs, after pulses are minimized by forcing the ions to undergo a significant change in direction at the juncture between the two MCPs [75].

The large gain of MCPs makes them a clear choice for applications of single electron counting. The short length of the channels also make them ideal timing detectors [78]. In the design discussed below, we have electric and magnetic fields that are approximately parallel

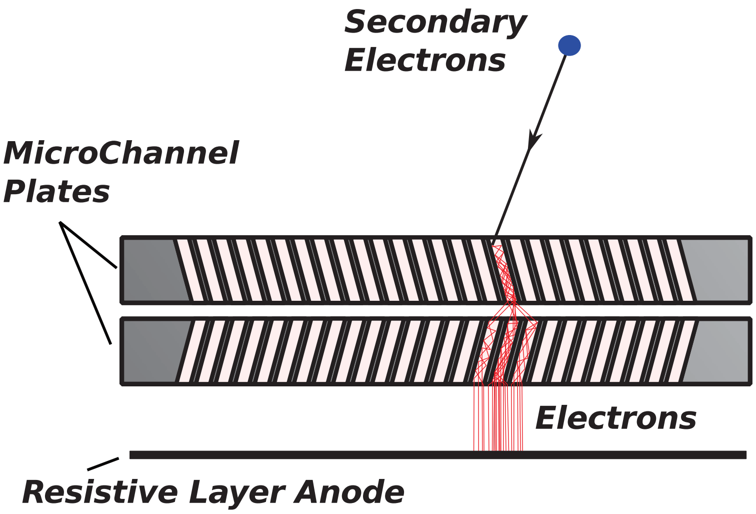

Figure 3.19: Signal amplification from secondary electron emission with two Chevron design MCP. Adopted from [77].

to each other and perpendicular to the target and the MCP. This ensures transmission of electrons from a point of emission on the target to an image on the front surface of the MCP [57, 58, 79, 80]. When the electron optics create an image of the charge emitted by the target foil on the input side of the MCP, position sensitivity can be achieved by using a position sensitive anode. The charge collected at the various points on the anode reflect the charge running though the channels immediately above, which itself corresponds to the spatial distribution of charge emitted by the target foil. As one choice, one can replace the anode with a grid of sensewires [79]. As a second choice one can use a resistive anode.

The MCPs described in here have resistive anodes with connections at four "corners". Charge deposited on the resistive anode is drained through the corners. Each corner signal is amplified. The amplitude of a specific corner signal is proportional to the ratio of the total resistance from the point of charge deposition on the anode to ground divided by the resistance to ground through that specific corner. The resistance to ground through that corner, in turn, depends on the distance across the anode to that corner. The technique of charge division, described below, is employed to deduce the position that charge is deposited on the anode and from that the position that the beam ion traverses through the target foil is deduced. This concept has been implemented in a number of nuclear physics and astrophysics experiments [57, 58, 80]. Details of the actual design are given in the next section.

3.6 MCP setup

A schematic diagram of the MCP tracking detector is shown in Fig. 3.20. It contains two MCPs in a chevron configuration. Each microchannel plate is a close packed structure, 0.46 mm thick, 40 mm in active diameter and composed of 10 μm diameter channels with a spacing of 12 μm between centers of adjacent channels [76]. A resistive anode layer is located 4 mm behind the second MCP and employed to obtain position information using resistive readout. The chevron configuration and resistive layer were assembled by Quantar [81]. Operation of this device requires a vacuum of less than 5×10^{-6} Torr to prevent discharge of electrons in the micro-channel tubes.

The tracking signals originate when an ion traveling from left to right traverses the MCP foil (rotated at an angle of 60° in the figure), and ionizes or scatters electrons from it. The MCP foil can be rather thin to minimize the energy loss of the beam particles; both 290 μg/cm^2 aluminized Mylar and 50 μg/cm^2 natural carbon have been used alternatively in our measurements with similar results. We biased the foil to a voltage of -1000 V, which accelerated the ejected electrons towards the MCP, whose front surface is at ground potential. Two permanent magnets provide a magnetic field that is roughly parallel to the electric field, confining low and moderate energy electrons to tight helical orbits coiling around the magnetic field lines. The points where the electrons' trajectories intersect the front surface

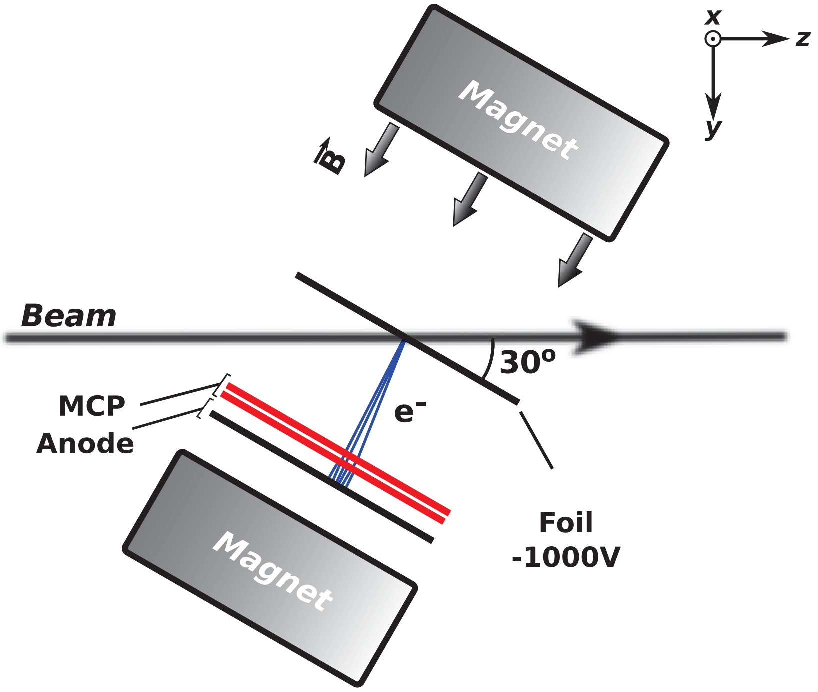

Figure 3.20: The schematic top view of a MCP detection system with 2 MCPs, a resitive anode, two permanent magnets, and target foil. Adopted from [77].

of the MCP becomes an image of the points where they are emitted from the target. In Section 4.4, we compare results from experiments using two different sets of magnets with fields of 0.13 and 0.57 T at the pole faces. In each case, the fields for these sets of magnets decreased smoothly to values of 0.03 and 0.127 T at the target, respectively.

After being deflected by the magnet onto the MCP, the electrons enter the micro-channel where they are multiplied and deposited on the anode behind the MCPs. Capacitively decoupled position signals were taken from the Upper Left (UL), Lower Left (LL), Upper Right (UR) and Lower Right (LR) "corners" of the anode. In addition, a capacitively decoupled time signal (T) is taken from the positive electrode of the second MCP in the chevron assembly. The electronic system of the MCPs is discussed in Section 3.8.

To obtain the angle of deuteron emission from the ^{56}Ni(p,d)^{55}Ni reaction, both the position at the target as well as the beam angle have to be measured, in addition to the position information from HiRA. To this end, two Microchannel Plates (MCPs) were placed at two locations along the beam.

3.7 The Laser Based Alignment System (LBAS)

The Laser Based Alignment System (LBAS) has two basic devices as its components, as shown in Figure 3.21: an Acuity laser [82] and two OWIS rotary stages [83]. The laser (Schmitt Measuring Systems, Inc, USA; Model no: Acuity AR600) is housed inside a box of 90 mm long, 26 mm wide and 154 mm tall. The laser beam is projected from the housing, reflected from the target surface, and collected at the laser collection system by a lens that focuses the image of the spot onto a CCD digital camera. The system uses triangulation measurement principles to determine distance with high sensitivity for very low amounts of reflected light. The LBAS measures distance in the range of 25.4 to 40.6 cm with a resolution of 45.6 um.

The sensor housing box is mounted on two rotary stages with OWIS stepping motors [83] and controllers (Wheedco, Model no: IMJ-105D-1-D). The LBAS stepping motors are controlled independently by two motion controllers that utilize digital signal processing. Two rotary stages can rotate the laser sensor for the capability of measuring 360 degrees in both theta and phi directions with a resolution better than 0.006 degrees. The overall position measurement can achieve resolution of 52.8-61.9 μm. A Java language based program was developed to control the laser, scan with specified step sizes and output the distance, theta and phi in spherical coordinates to a file.

A laser beam scans along the surface, and determines the position of an edge by the abrupt change in the distance when it reaches the edge. To determine the position of the

Figure 3.21: Photograph of Laser Based Alignment System (LBAS).

target center, a mask with 5 well-defined holes as shown in Figure 3.22, as well as in Figure 4.25, occupied one of the target positions. Figure 3.22 shows the target ladder with a beam scintillator viewer placed on the top followed by four $(CH_2)_n$ reaction targets of different thickness, a highly uniform thickness of carbon target and the target mask. Each hole on the mask was scanned twice in horizontal and vertical directions for a total of 20 edge points as shown in Figure 3.22. We obtained the first-order estimate of the centers by averaging the scanned edge points of each hole. Determination of center positions was done by requiring that all the centers lie on the plane forming a 1 cm×1 cm square. The center of the central hole corrected for the target mask thickness represents the reaction target center. The results indicate the target mask is titled by 0.7 degrees with respect to the beam axis. This is a small angle that corresponds to an insignificant distance change of 0.06 mm between holes. The center of reaction target is defined as the origin in our reaction system.

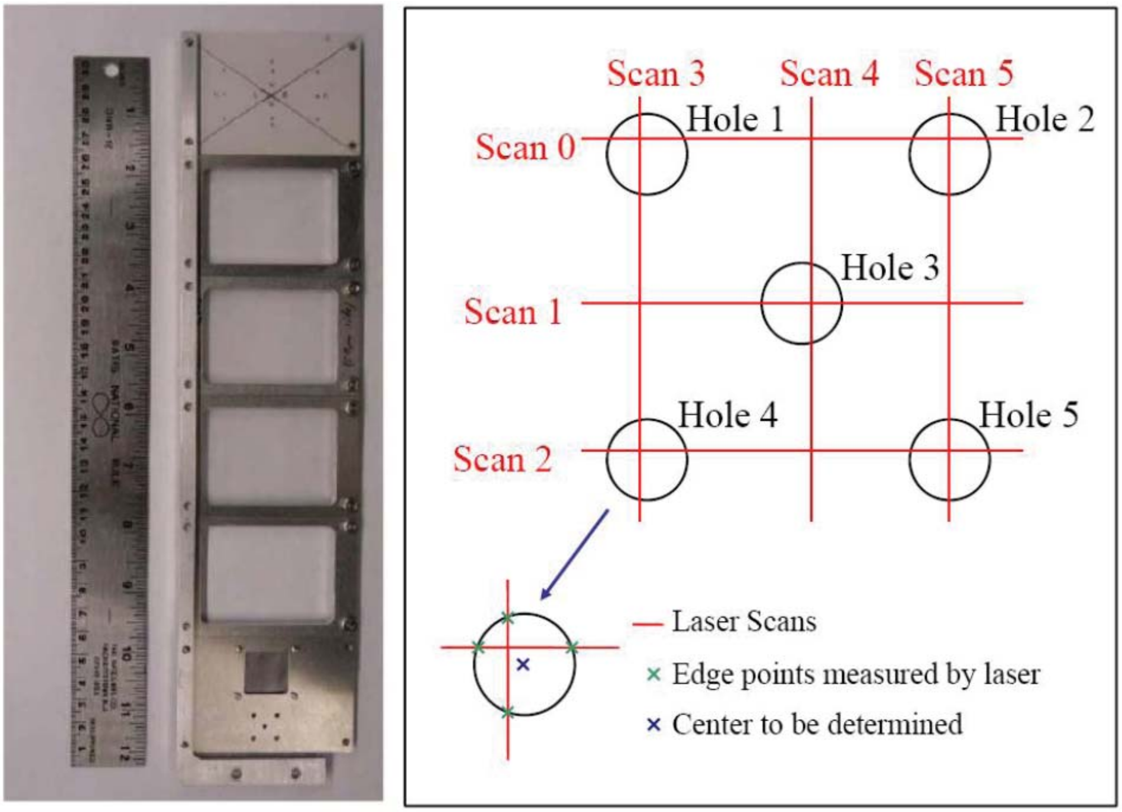

Figure 3.22: (left) Target ladder with a beam scintillator viewer placed on the top following by four $(CH_2)_n$ reaction targets of different thickness, a highly uniform carbon target (appeared as a black square and target mask. (Right) Schematic diagram of the strategy of laser scanning on the target mask. Adopted from [53].

Figure 3.23 displays the configuration of the six large holes on each MCP mask. Following the same strategy used in the target mask measurement, four edge points were obtained for each hole and used to constrain fitting to determine the centers of each hole. The results show that the angle between the MCP foil and the beam is 58.46° for MCP0 and 59.79° for MCP1, slightly different from the design of 60°. The centers of the MCP0 and MCP1 foils deviate from the target center by approximately 1.5 mm and 0.7 mm in vertical and 0.91 mm and 0.54 mm in horizontal direction respectively.These displacements are taken into account in measuring the beam positions at the MCP foils. To achieve the best angular and energy resolution at large laboratory angles, these offsets are taken into account in the analysis. A more detailed description of the LBAS system can be found in [53].

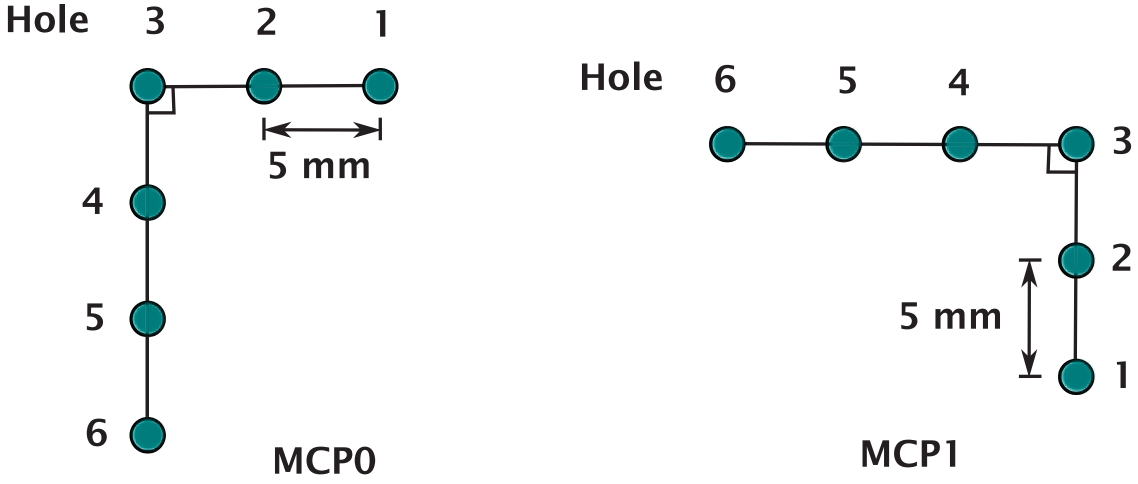

Figure 3.23: The configuration of six large holes in two MCP masks.

For each HiRA telescope, the frame was scanned three times on each side. Four corner positions of the frame were determined by fitting the plane with the constraints of the four measured sides forming a square lying on the same plane. Using the known distance between the frame and the silicon detectors and the strip dimension, the positions of the pixels can be deduced. The LBAS measurements give 35.97±0.12 cm while the design value is 35.76 cm. The difference is small and comparable to the strip size of a HiRA E detector, which is 0.2

cm. It was also found that the normal of some telescopes did not point to the target center. The maximum deviation, the angle between the normal of the telescope face and the line from the center of telescope to the center of target, is 2.58° (telescope 5). These systematic and consistent discrepancies reflect distortions in the mounting structure.

3.8 Data Acquisition and Electronics System

We have three main detection devices, and consequently, the data acquisition system consists of three subsystems, HiRA, S800 and MCP. The coincidence of the HiRA and the S800 triggers define the coincidence premaster trigger. This is done so that every event has reaction products both in HiRA and S800, and limits the data to kinematically complete measurements of the reaction. The MCP data is mainly acquired as a slave process, so that for every registered event, we have the angle and the position of the beam particle on the target, assuming 100% efficiencies. In addition, downscaled MCP data were also recorded as an independent trigger.

3.8.1 HiRA and Application Specific Integrated Circuit (ASIC) Electronics

We start our discussion of the electronics system with HiRA electronics. The flowchart for the HiRA electronics is shown in Figure 3.24. With the increasing complexity of experiments in nuclear science and other fields, there is a growing demand for high density electronics in analog signal processing. Each HiRA telescope has 96 Si channels, 32x2=64 for front and back of the E detectors, and 32 more for the DE detectors. A typical HiRA configuration may consist of about 20 telescopes, giving us total of 1920 channels to process. With conventional electronics, the large number of channels would require a very large number of cables and classical electronics modules. This is very expensive, and prone to connection problems because of the number of cables and connectors involved.

To address this issue, an *Application Specific Integrated Circuit* (ASIC) chip called HINP16C was developed in collaboration with Washington University in Saint Luis [84]. A schematic block diagram of an ASIC chip is shown in Figure 3.25. Each ASIC chip processes signals for 16 individual channels. Since HiRA silicon detectors have 32 strips on each surface, two ASIC chips with other high density electronics mounted on a *chipboard*, are used for each surface. Input and output signals of several chipboards are merged by a circuit board called the *motherboard*. Each motherboard had 8 chipboards in the present experiment.Photographs of a motherboard and chipboard are shown in Figure 3.26. Details of the HiRA electronics can be found in Reference [84].

In the following we describe the ASIC electronics schematically. The signals from DE, EF or EB strips go first to the *Charge Sensitive Amplifier*, and then to the pseudo-constant fraction discriminator (PCFD) and to the shaper within the ASIC in the chipboard. The logic signal from the PCFD goes to a hit register and time-to-voltage converter (TVC) circuit. If the signal is above a computer set threshold the PCFD triggers and the hit register is set. The TVC is started by the PCFD and generates a voltage signal which is proportional to the time between the start and an external stop. The resulting two signals from the shaper and CFD circuits are sent to peak sampling circuits which are designed to track and hold the maximum value of the input signal. Then both the E and T signals are sent to an off-chip differential amplifier, which generates the E and T analog signals.

If the signal triggers the PCFD, the time, energy and event address go to the HiRA motherboard buffer. Also the PCFD time signal is transformed through an ECL-NIM module and

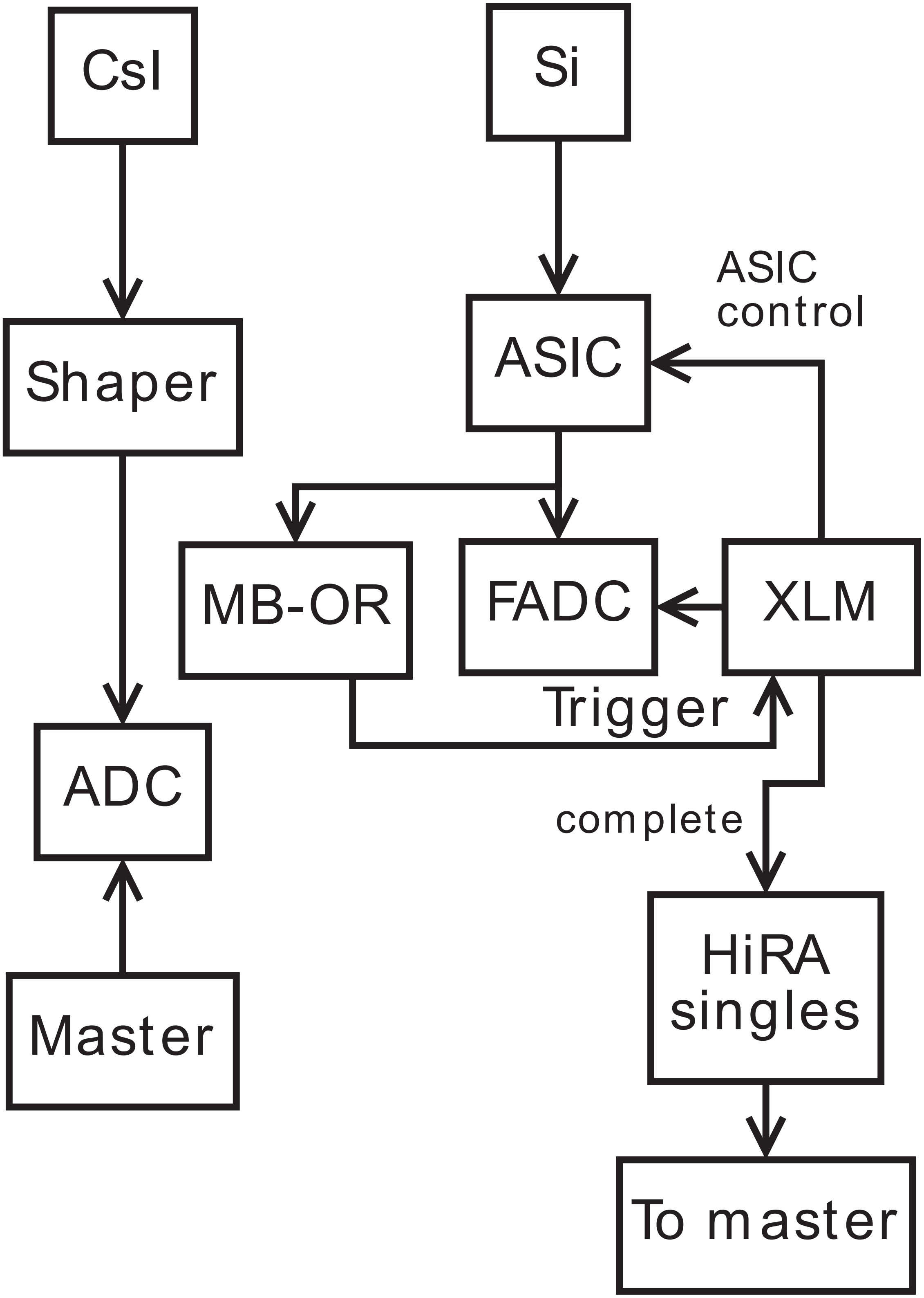

Figure 3.24: Flow chart of the HiRA data acquisition system.

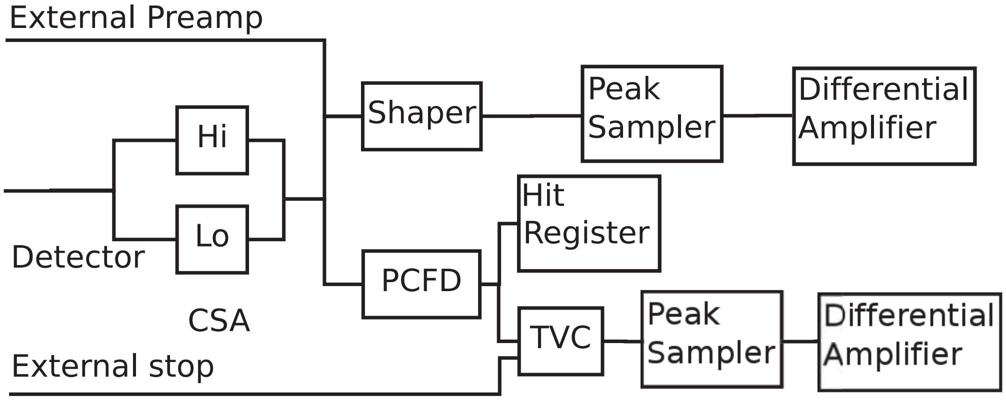

Figure 3.25: A block diagram of an ASIC chipboard.

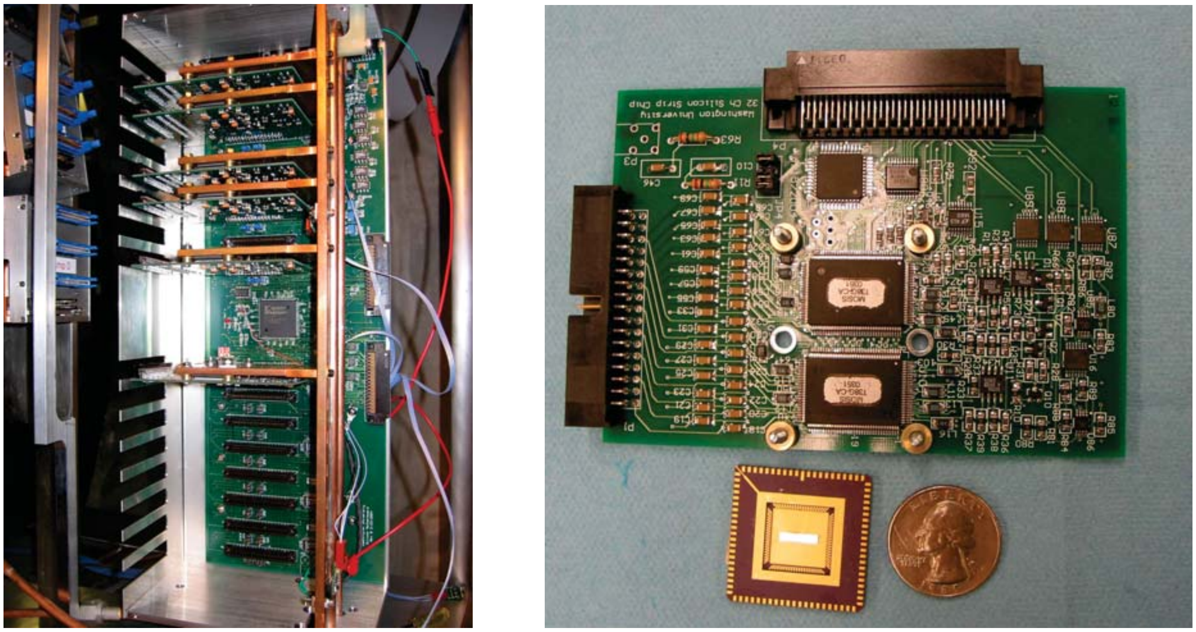

(a) A photo of an ASIC motherboard housing 6 chipboards.

(b) A photo of an ASIC chipboard. An 8 channel prototype is shown in the bottom left.

Figure 3.26: HiRA ASIC photographs.

then is sent to a logical “OR”, to trigger the XLM universal logic module. The “OR” signals from different motherboards are fanned out and logically OR-ed to give the HiRA premaster signal. The HiRA premaster is then logically AND-ed with the S800 premaster signal to give coincidence premaster signal. An XLM performs the task of controlling the readout of the ASIC motherboards. Once the XLM is triggered, the event address information is sent directly to the XLM, and the corresponding time and energy information are sent to a *Flash Analog-Digital Converter* FADC. A clock signal issued by the XLM becomes an input to the FADC to initiate the FADC to digitize the time and energy signals and store them in its internal buffer. When the requested data is no longer acknowledged by the motherboard, a logic “complete” signal is sent out by the XLM and used as the start for the trigger latch.

3.8.2 S800 Electronics

The second part of the electronics system is the S800. A schematic electronics diagram of this system is shown in Figure 3.27. The signals from each of the top and bottom (also called “up” and “down”) PMTs of the E1 scintillator in the focal plane of the S800 are amplified and split into two signals. One of the signals goes to a constant fraction discriminator (CFD) module and provides a logic pulse. The second one is sent to a fast encoding ADC (FERA). The E1 “up” CFD output serves as the S800 premaster signal. The coincidence between the S800 premaster and the HiRA premaster gives the master trigger of the experiment. Additionally, the S800 premaster signal serves as the start for ion drift time in the CRDCs. Combined with the CFD logic pulse from the CRDC anode wires that serves as the stop for a *Time to Analog Converter* (TAC), it gives the drift time of the ions, after the TAC output is digitized by an analog-to-digital converter (ADC). The drift time, in turn, provides the Y-position (non-dispersive) in that CRDC. As described in Subsection 3.4.1, the signals from the pads are processed using front end electronics (FEE) system of the STAR collaboration. This process is started by the S800 premaster and stopped by the anode CFD pulse. For the ion chamber, each anode has a small postage stamp size preamplifier attached to it inside the ion chamber and has a charge gain of 500 mV/pC. The preamplifier signals are then shaped by a sixteen channel spectroscopy amplifier, after which they are sent to an ADC. There were two TDC's used in the experiment, one "S800 TDC", and another one downstairs near the large scattering chamber, called the "MCP TDC". Time signals such as extended focal plane (XFP), MCP, and RF timing signals are digitized by both the S800 TDC (Phillips 7186H), and MCP TDC (CAEN V775) after additional delays.

3.8.3 MCP Electronics

The third part of the data acquisition system is the MCP system. Each of the four signals from the anode corners, that are used for calculating the position on the MCP foils, are split into two using a fast amplifier (ORTEC 820). One of the signals from each corner is amplified via a fast amplifier (CAEN 979N), and called "high gain" (HG) corner signals. The other one is left unchanged and called "low gain" (LG). Both HG and LG signals are sent to charge-to-digital converters (CAEN V792N QDCs) and digitized. The timing signals from the MCPs are amplified via ORTEC VT120 fast amplifiers and sent to constant-fraction discriminators (CFD). Then the logic signals are split into two. One will be delayed and sent to the "MCP" TDC (CAEN 775) to be digitized. The other signal is logically OR-ed with the same timing signal from the second MCP. The OR signal is downscaled by the rate divider, delayed and logically OR-ed with the master trigger to enable the gate signals for the QDCs.

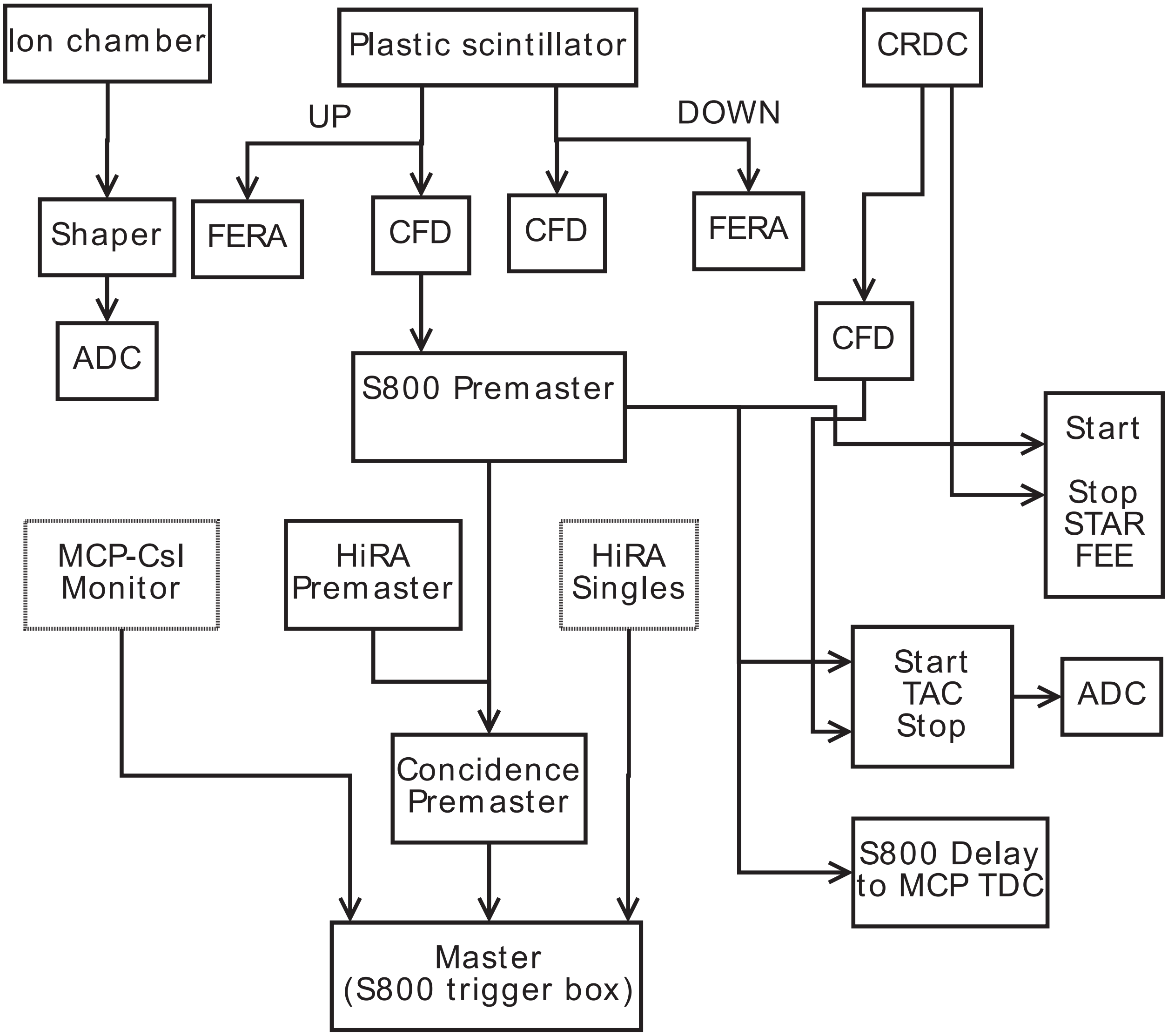

Figure 3.27: Flow chart of the S800 data acquisition system.

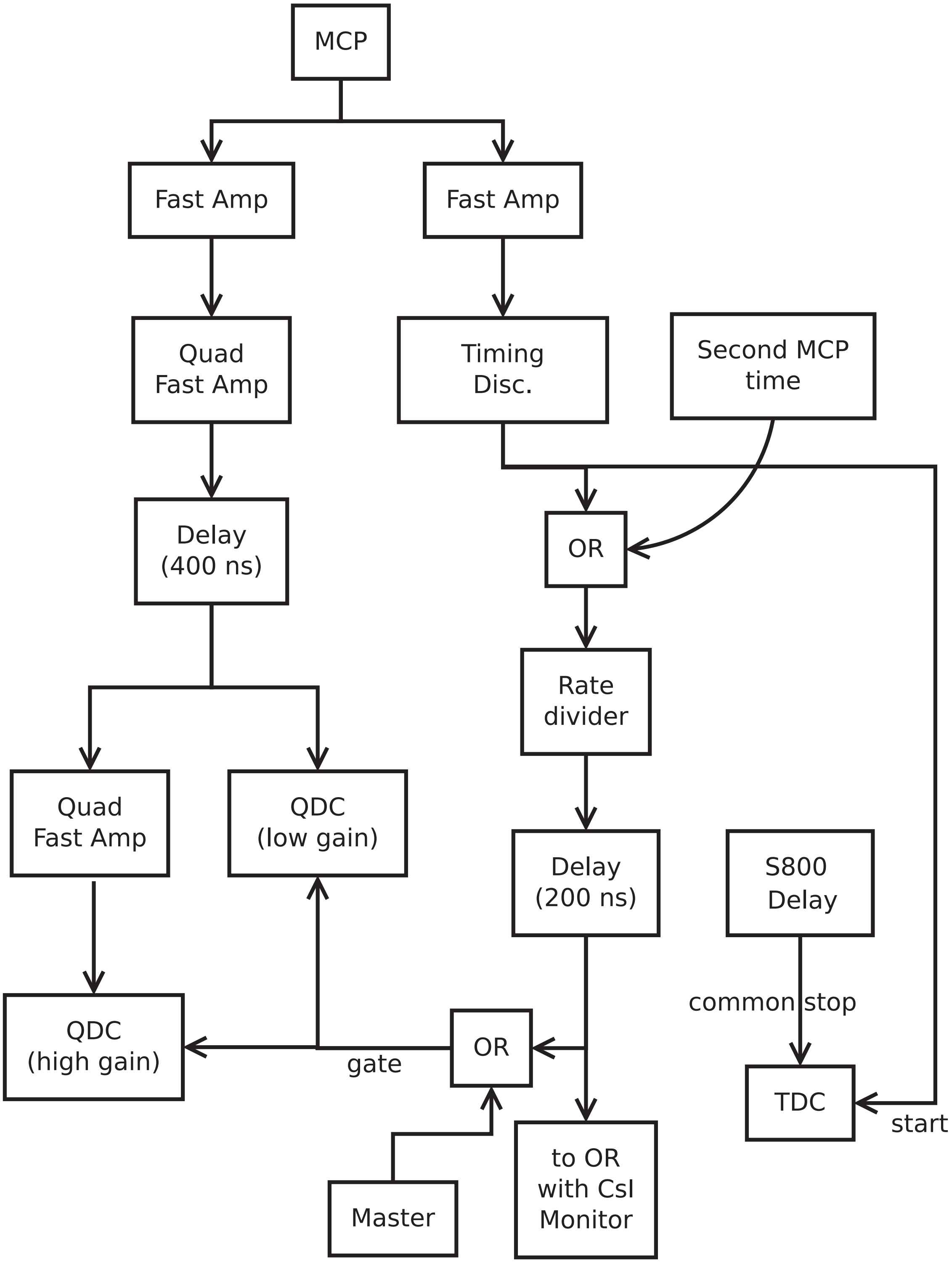

Figure 3.28: Flow chart of the MCP data acquisition system.

Chapter 4

Data Processing and Analysis

4.1 Overview

Nuclear physics experiments produce data from electric signals generated in detectors through an electronic *Data Acquisition System* (DAQ). The DAQ system writes the data into computer files for further processing. The recording of the data is stopped and restarted in order to have manageable file size of less than 1 GB, or to change the settings of measurements, and this period is called a “run”. For complex experiments like this, with a large number of detector channels and different types of detectors, the raw data files can be difficult to handle and analyze. One of the purposes of data analysis is to reduce the complexity of raw data by changing it into more manageable and physically meaningful data sets.

Our experiment consisted of three subsystems, HiRA, S800 and MCP. To make our analysis simpler, we adopted the strategy of dividing and analyzing each subsystem separately, and integrating them later. Figure 4.1 shows the flowchart of how we start with the raw data and obtain physics information seat the end.

The ROOT data analysis package was used for analysis of the experiment. It is a set of object oriented frameworks designed to handle and analyze large amounts of data [85]. The raw event data file is converted into a raw ROOT file, which is subsequently split into three different files for the relevant subsystems. At the same time, a preliminary calibration is done on each of those files. This method makes the data analysis more manageable, and reduces the size of the file when working on a particular branch of the analysis. The analyzed data from each of the devices are integrated and relevant physics information is obtained.

4.2 HiRA Analysis

HiRA detects the deuterons that are produced as a result of the ^{56}Ni(p,d)^{55}Ni reaction. There are three main functions of the array:

1. Identify the deuterons from other light charged particles.
2. Measure their energy accurately and precisely.
3. Measure the angle of emittance of deuterons with respect to the beam direction.

In order to simplify the task of calibration, HiRA data processing is done in two steps. As mentioned above, a preliminary calibration is done according to the telescopes and detectors therein. At this stage, all the Si and CsI detectors are calibrated and grouped under telescopes. However, further processing is needed to extract the energies from the Si detectors, as will be explained in subsection 4.2.3. The next step is called “pixelization” described in subsection 4.2.6, where each event has been assigned a position in space, in addition to energies in each detector they interact with.

4.2.1 Pulser Calibration

It is important to ensure that signals from the Si and CsI detectors are converted into digital channels in a linear fashion. For this purpose, pulser calibrations were carried out for CsI as well as the DSSD detectors. In the case of the CsI’s, a single pulser signal is delivered to the test inputs of the CsI preamps via a distribution box.

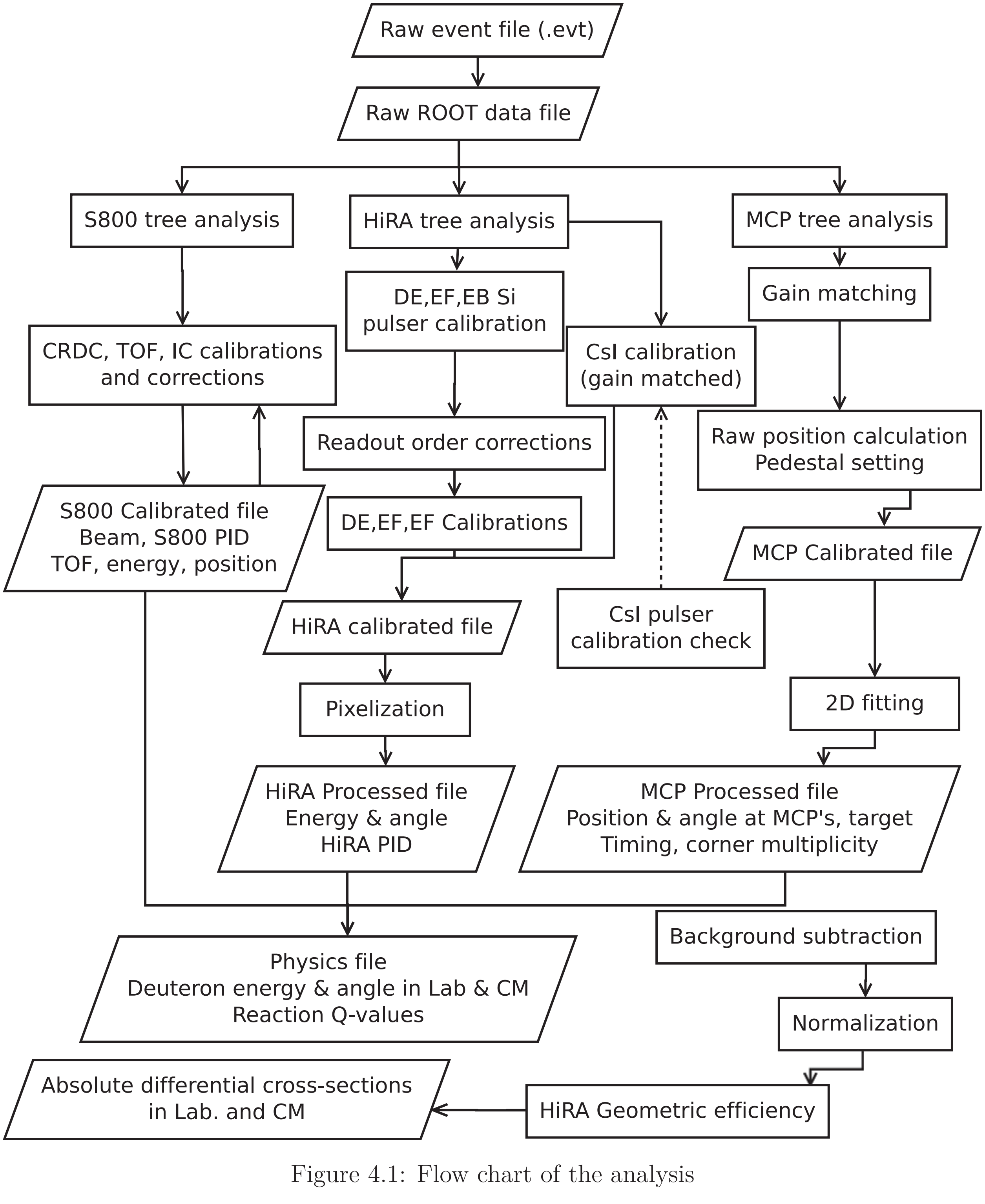

Figure 4.1: Flow chart of the analysis

Fig. 4.2 shows pulser "ramp" data for a CsI crystal, where the amplitude of the pulse is increased from zero to 0.5 V in steps of 5 mV to scan the entire range of the ADC. Note that at 0.25 V, there was a peak with double the normal amplitude to help identify the correspondence of pulses with ADC channels.

Figure 4.3 shows the linear fit of the pulser ramp of the same CsI(Tl) crystal. The pulse amplitude is equivalent to the light output of the crystal. It has been known that the combination of amplifiers and ADC modules start to show nonlinearities above channel 3500. Taking this into account, the fit is done only up to 3500 channels.

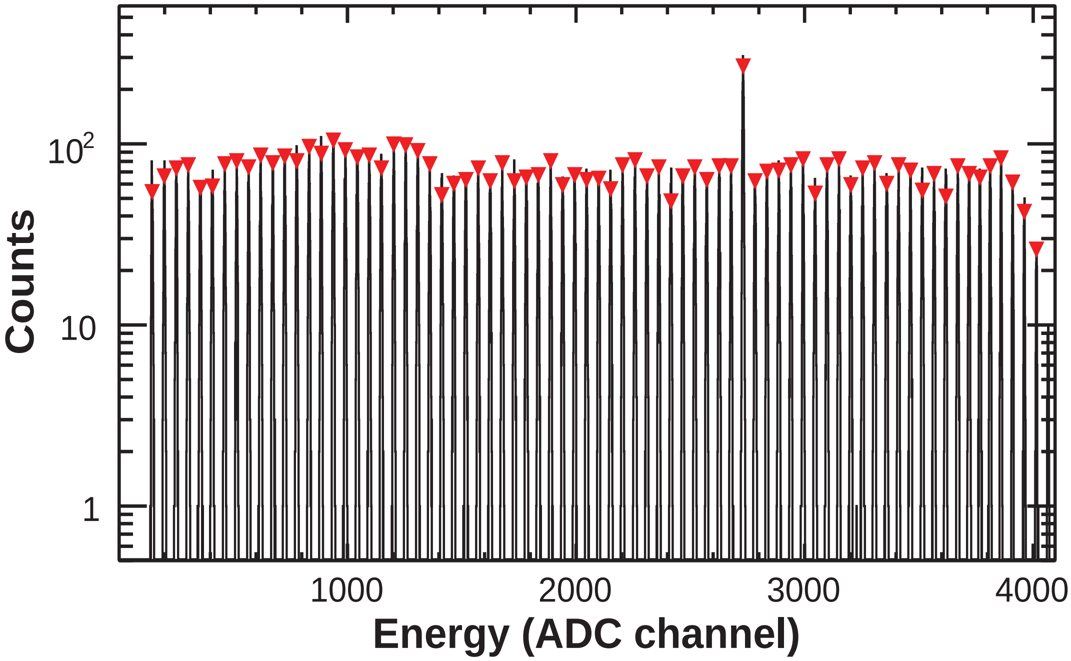

Figure 4.2: Pulser ramp of telescope 10, CsI 1 crystal.

For pulser calibrations of Si detectors, a pulser system developed at Indiana University (IU) was used [86]. The "IU pulser" provides automatic pulses with an accuracy of <0.1%. A pulser ramp is carried out on all strips individually. Fig. 4.4 shows the pulser ramp of an individual strip. It can be seen from the even spacing in the figure that the Si strip is linear

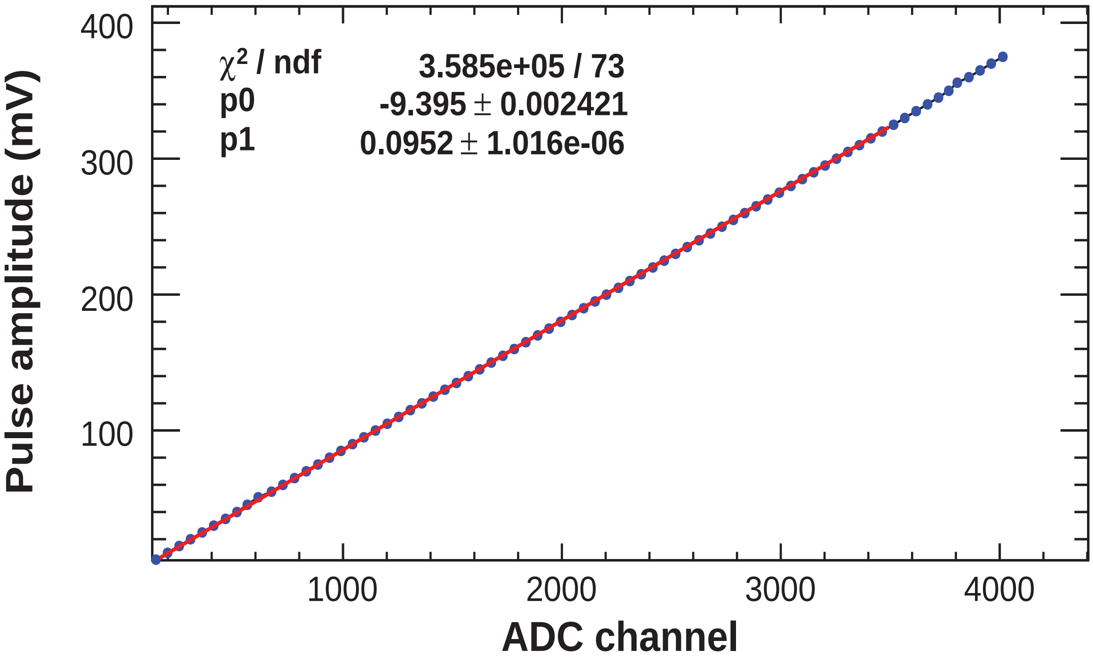

Figure 4.3: Linear fit of the pulser ramp for telescope 10, CsI 1 CsI crystal.

over the dynamic range of EB (38 MeV). All strips for EF, EB and DE have similarly good linearity.

4.2.2 Readout Order Corrections

The main issue of the HiRA ASIC electronics used in the present dissertation is the readout order problem, i.e. dependence of amplitude of signals on the order it is read out. This problem has since been corrected by a new ASIC and the new ASIC will be used in future experiments. In either ASIC, there are two modes of readout, sparse and forced. In sparse mode only channels that triggered the discriminator are read out, whereas in forced mode all channels are read out. For the present experiment, sparse readout mode is used. In the mainboards, which are processed independently from each other, chips are read out from the bottom to top. (See Figure 3.26a.) Each DSSD has two chipboards processing signals, one

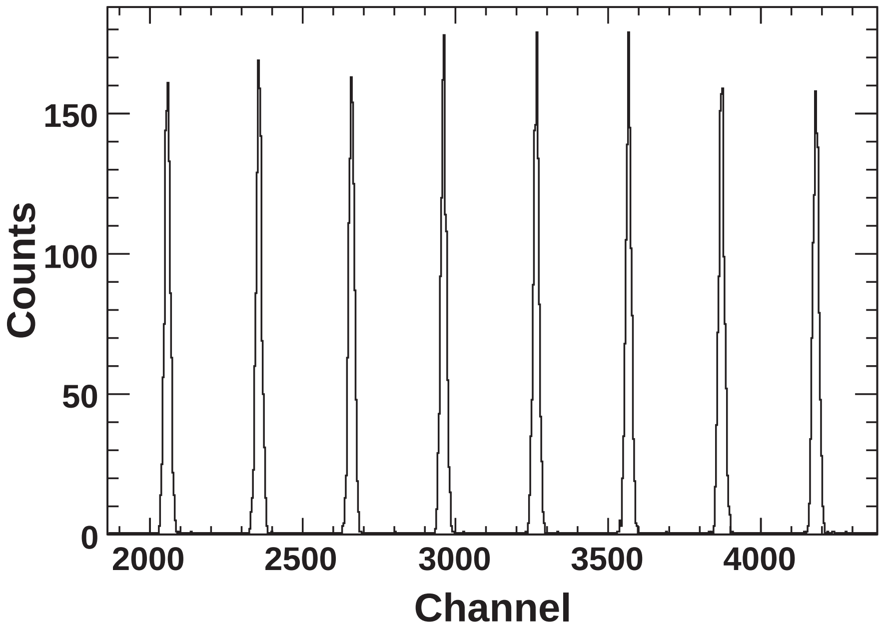

Figure 4.4: IU pulser ramp spectrum of a single backside strip in HiRA telescope.

for front side (EF) and one for back side (EB) of the DSSD, and this influences the order in which these signals are processed. Because the EB output connectors are located lower than EF output connectors on the back of the telescopes, EB signals are always read out before EF signals. Additionally, each side of a DSSD is processed by two 16 channel chips. For the back side, one chip (chip 0) processes all the even strips before the second chip (chip 1) processes the odd strips, while the odd strips are read out first for the front side.

It was known from a previous experiment [77] that the energy value of a given channel was affected by the number and sequence of channels read previously to that channel. For each particle that passes through the DSSD, signals of equal magnitude, but opposite sign are generated on one front strip and one back strip of the detector. The value of the signal read out for the back strip stays unchanged, as it is the first channel in the sequence processed. However, the amplitude of the front strip is altered due to the back strip that previously read out.

In general it is found that the amplitude for a particular channel is shifted by a constant amount that only depends on the number of channels readout prior to that channel. The results of the readout order problem are clearly observed in the alpha-source spectra in Figure 4.5. The double-peak (or peak-shoulder for some peaks) structure is a direct consequence of the readout order problem. When an alpha-particle deposits its energy in the detector, ideally an equal number of holes should be collected on a single front strip as electrons on a single back strip, thus uniquely defining a pixel. However, there is also a possibility that electron-hole pairs from an event are collected over more than one back strip. The second most probable situation after a two strip event (one front and one back) is a three strip event where one front strip fires along with two back strips. Since the back strips are processed first there are now two channels read out prior to the front strip as opposed to just one. This results in a shift in the amplitude of the energy signal from the front strip and is observed as a shadow peak at higher energies in the upper spectra in Figure 4.5 near channel 3600.

To determine the correction values, the readout order of each signal within the motherboard (MB) and chipboard (CB) was identified when unpacking the data from an event file using two parameters. One of them is a 32-bit array used to represent channels being fired in a CB with the corresponding bits flipped to 1 from 0. The second parameter represents the number of channels read in a tower. From these two parameters, we can deduce the readout sequences of a hit in its corresponding MB and CB.

For readout order correction, procedures established by V. Henzl were used [87]. The corrections were done by Jenny Lee [53]. The readout order corrections for the MBs and CBs are determined independently, because there is no evidence that those two are correlated. The correction for each strip is the average of shifts in four alpha peaks with energies of 5.69,

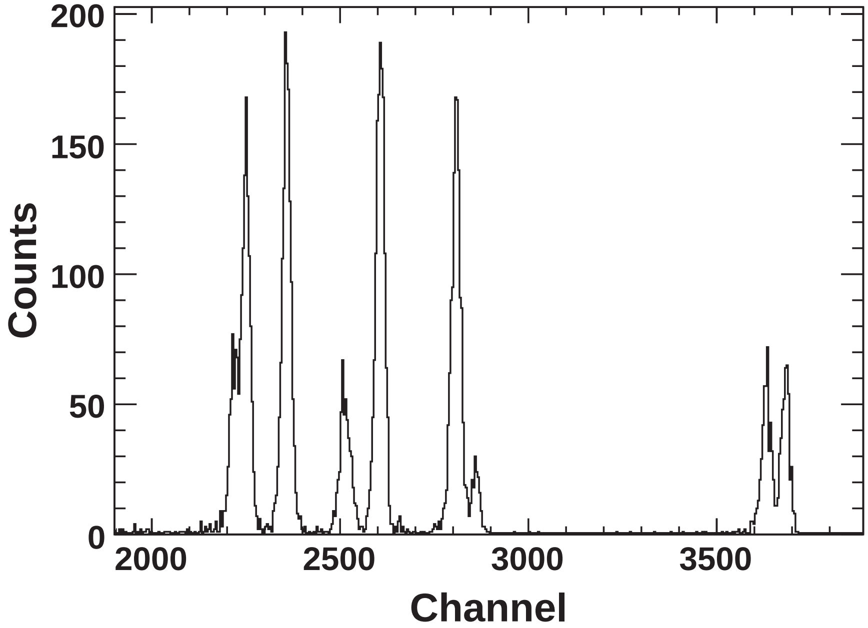

Figure 4.5: A raw ^{228}Th alpha spectrum of one EF strip without the readout-order correction.

6.29, 6.78 and 8.78 MeV at the particular MB readout sequence. The average MB readout corrections in units of channels for each telescope are listed in Table 4.1. Each strip within a telescope is corrected individually, however, the corrections differ only slightly from the average. The non-integer values of shifts are caused by the randomization of digital channel outputs used in the analysis.

4.2.3 Si Detector Alpha-Source Calibrations

To obtain the real energy information, the Si detectors were calibrated using α-particles. A ^{228}Th α-source was placed at the target position. The source has an activity of 1.2 μCi and a Au window of 50 μg/cm^2 thickness. As seen in Figure 4.6, the α-particles have 5 prominent energies at 5.43 MeV, 5.685 MeV, 6.288 MeV, 6.778 MeV and 8.785 MeV. These peaks are identified and channels are transformed linearly to corresponding energies. Typical

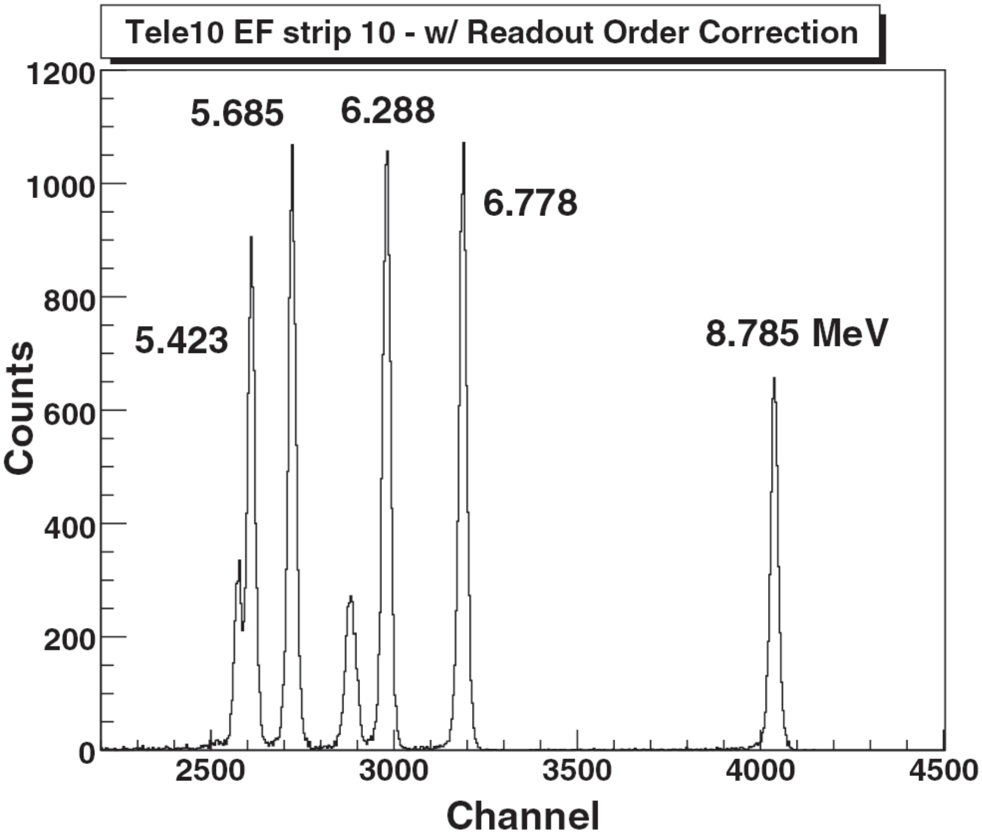

Figure 4.6: A raw ^{228}Th alpha spectrum of one EF strip after readout order correction applied on both motherboard and chipboard readout.

Table 4.1: Average MB corrections for the first two readout orders for EF and EB within each telescope. Units are in channels.

Average readout order correction for MB on EF											
Tower0			Tower1			Tower2			Tower3		
Tele	1st	2nd	Tele	1st	2nd	Tele	1st	2nd	Tele	1st	2nd
0	-6.72	-12.33	10	-6.97	-10.51	14	-0.09	2.01	4	-7.86	-10.53
1	-4.07	-5.98	11	-7.54	-12.96	15	-0.27	1.85	5	-6.72	-8.32
2	-4.59	-7.90	12	-6.89	-10.45	17	0.64	2.17	6	-7.06	-10.68
3	-5.68	-9.39	13	-7.19	-11.08	16	-4.00	-5.42	19	-7.39	-11.87

Average readout order correction for MB on EB											
Tower0			Tower1			Tower2			Tower3		
Tele	1st	2nd	Tele	1st	2nd	Tele	1st	2nd	Tele	1st	2nd
0	18.14	29.51	10	37.60	65.47	14	32.48	61.32	4	14.61	25.27
1	33.91	54.71	11	30.56	46.70	15	26.20	42.97	5	15.59	25.95
2	35.82	54.50	12	32.92	60.86	17	33.90	62.95	6	16.73	26.33
3	31.59	45.86	13	37.06	68.59	16	31.11	55.74	19	17.55	27.09

resolutions for 6.778 MeV particles in DE, EF and EB are 45-55 keV, 60-75 keV and 60-85 respectively. However, about 20% of EB strips have relatively worse resolutions of 90-120 keV; therefore, the EF strips were used as deuteron energies in the analysis for all events.

The energy range of alpha particles used in the calibration (5.42 to 8.79 MeV) does not cover the dynamic ranges of DE and EF (13 and 38 MeV, respectively) in this experiment. However, as discussed in subsection 4.2.1, it was verified that all strips have good linearity. Therefore the calibrations obtained from alpha source spectra were extended using the pulser calibration to the full ADC ranges.

4.2.4 CsI(Tl) Calibration

CsI(Tl) are necessary for identification of particles that punch through the E Si detectors and measurement of their energies. CsI(Tl) detectors were calibrated using the ΔE-E method. Knowing the thickness of Si detectors preceding the CsI(Tl) crystals, one can calculate the remaining energy of the deuteron that punches through the Si detector and stops in CsI(Tl).

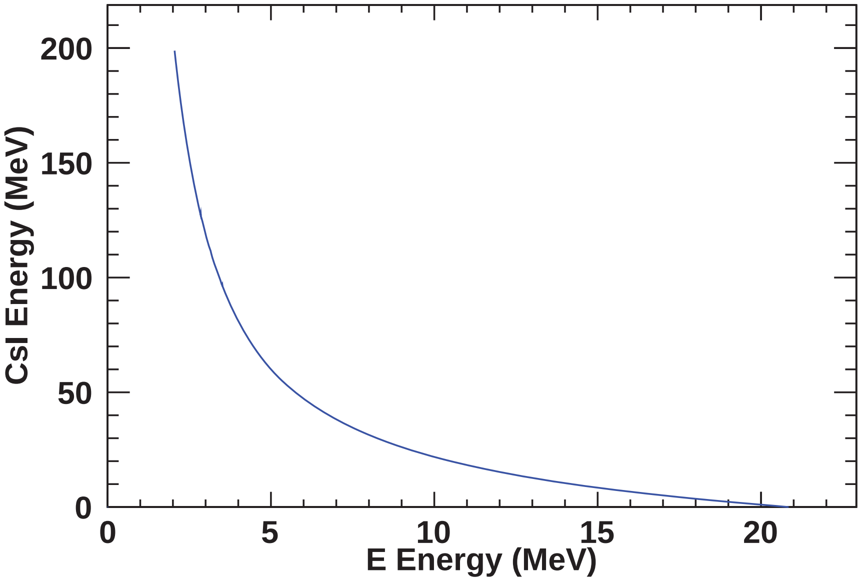

Figure 4.7: Deuteron energy in CsI as a function of energy in Si E detector for deuterons in telescope 19, from a LISE calculated table [88].

4.2.5 Test of Light Response of CsI(Tl) Crystals at Western Michigan University

It is known that CsI(Tl) exhibit nonlinearity and dependence of light output on particle type [89]. To test the nonlinearity of CsI's for light charged particles, two HiRA CsI(Tl) clusters were taken to the Western Michigan University tandem Van deGraaf accelerator facility [90]. The silicon detectors were removed since our main purpose was calibration of

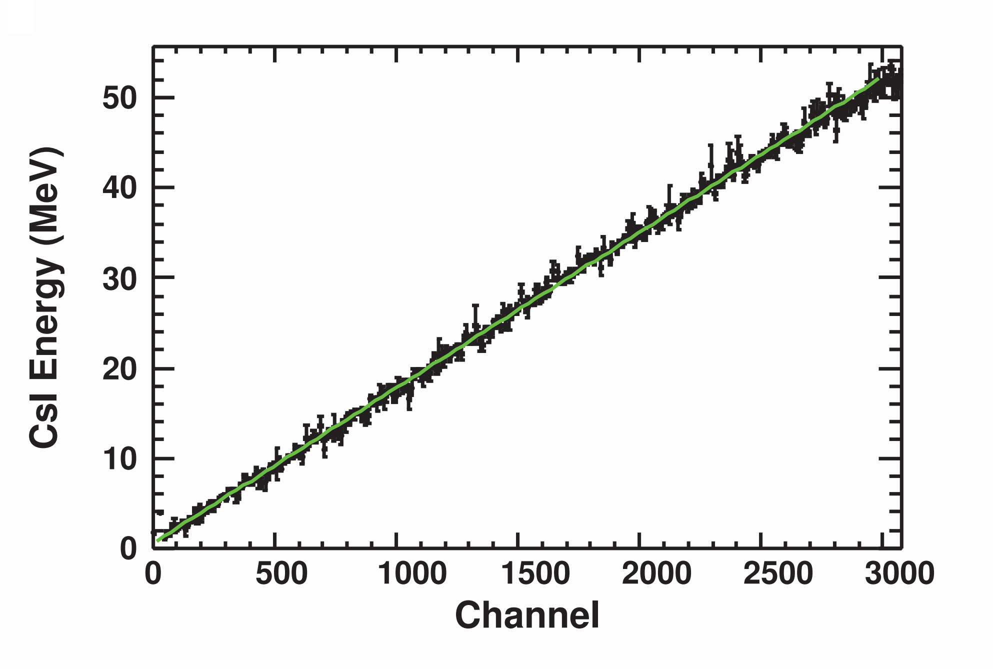

Figure 4.8: Linear fit of uncalibrated CsI energy with calculated CsI energy using Si energy for deuterons.

CsI's. A 1 pnA beam of protons at energies 1.5, 2, 4, 6, 8 MeV was used. The chamber where the detectors were placed was a flat cylinder of 42.5 cm in diameter and 26 cm in height, as shown in Figure 4.9.

A thin carbon target of thickness 80 μg/cm^2 was put in the beam entrance to the chamber. The detectors spanned an angular range of 10°-50°, with 4 crystals (inner) at 10°-30° range and 4 crystals (outer) at 30°-50° range. Classical NIM electronics (shapers, discriminators etc.) were used in the setup. The inner detectors were not triggered because of a very high count rate. Hence only the data from outer 4 crystals are discussed in this work. Kinematics calculations were done for angles 10°-50° and beam energies of 1.5, 2, 4, 6, 8 MeV.

Figure 4.10 shows the relationship between the calculated energy of the scattered proton and the measured channel in the CsI readout. The relationship is linear at higher energies, however it is no longer linear below about 1 MeV. Although the tests were performed with

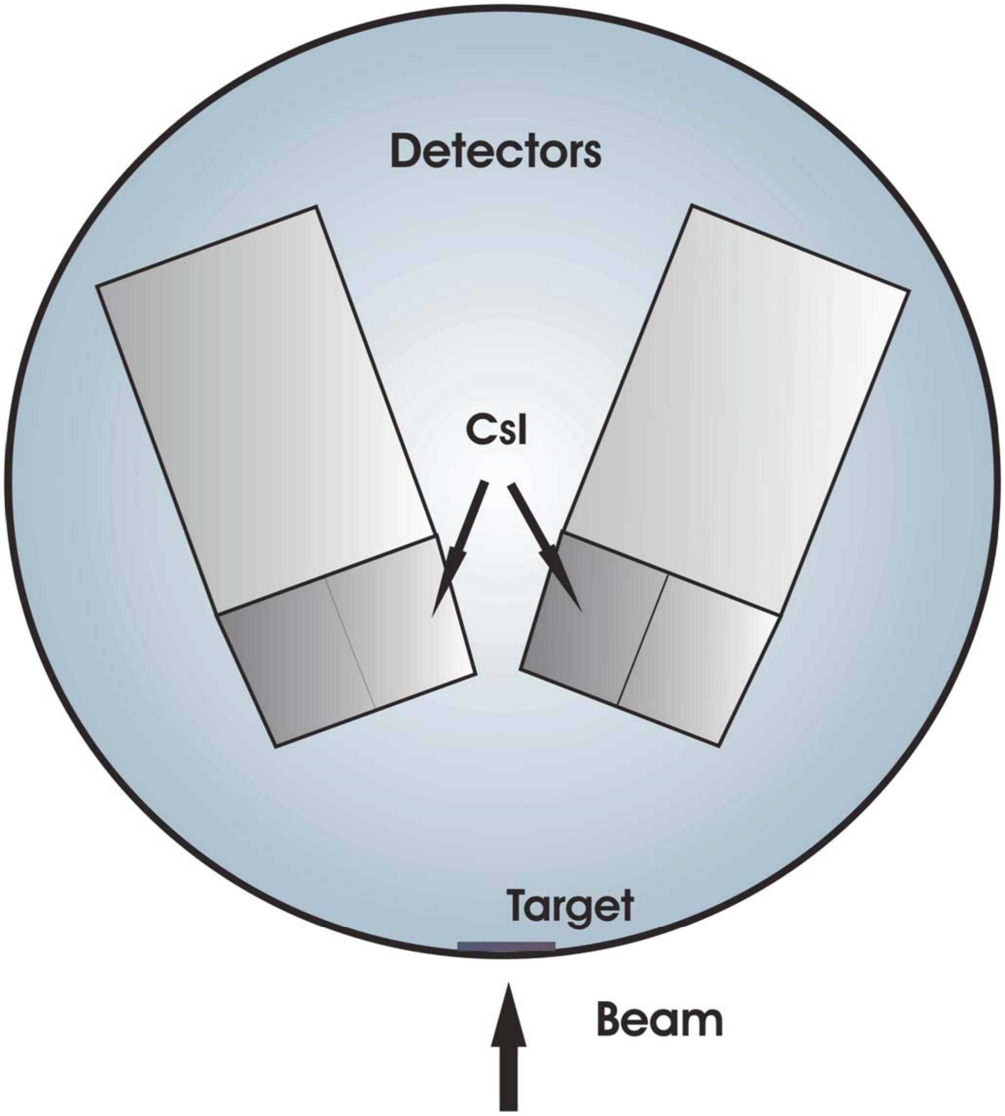

Figure 4.9: Setup with two HiRA telescopes in the WMU chamber.

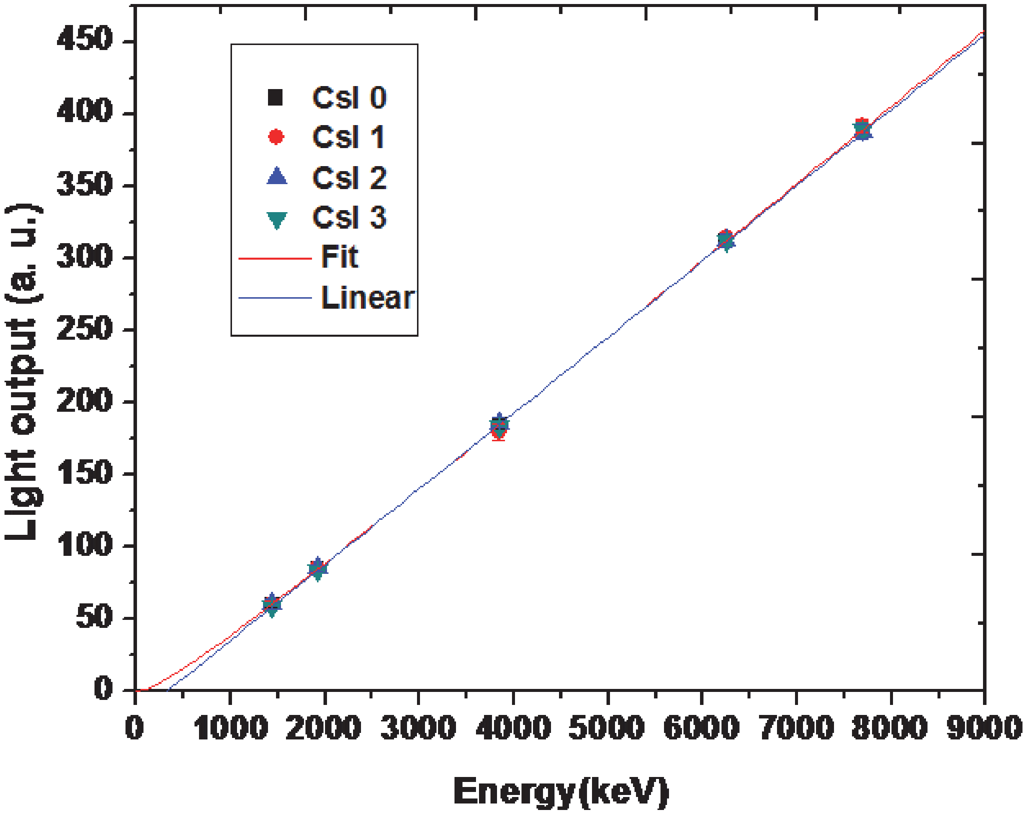

Figure 4.10: Normalized light output vs energy (keV) for four CsI(Tl) crystals.

proton beams, this relationship should be approximately valid for deuterons as well [70]. This has to be taken into account when calibrating CsI and corrections should be made if the deuteron energy is less than 1 MeV. This study was useful for the present experiment, as it confirmed the linearity of the CsI's at energies above 1 MeV. Thus, in the present experiment, we did not use the events with CsI energies below 1 MeV.

4.2.6 Pixelization

After calibration of Si and CsI(Tl), each event is associated with a telescope number, and a telescope must be "called" in order to access the events registered in this particular telescope. In ROOT, this means the events are stored in separate telescope "trees", and each telescope tree must be processed and plotted separately. This is not the best way to represent data, however, and one would like to process all the events in one such tree, without having to specify the telescope number. This tree is called pixel. In this tree, telescope number and strip numbers are just data members, like the energy and position, which are more physically relevant. The position is calculated for each pixel using the EF and EB strip numbers. Since we know the measured positions of corners of telescopes, we can calculate the position for each individual pixel.

Additionally, this stage of data transformation can be used to process the Si events where more than one adjacent strips have signals. The energies are added for these events by using the method of "gluing" developed by V. Henzl [87]. When more than one strip on EF or EB are fired within a telescope in one event, we first examine two adjacent channels of each registered strip and discard the signal with energy smaller than the threshold defined as 1.25 MeV + 1% of the energy of the registered channel. Such small signals are regarded as noise or cross-talk. After that, the remaining signals in the particular telescope are sorted according to their signal amplitudes (calibrated energies) in descending order for EF and EB separately. On each face, hits in separated and non-neighboring strips are considered as singlet; while hits in neighboring strips are labeled as doublets unless it is found to be an accidental neighboring single hit. If hits are identified as singlets on both sides, then we can pair them up according to their energies. When the energy difference between a singlet on one side and the sum of two doublet signals on another side is smaller than 5% of the energy of singlet energy, then we combine the doublet hits together and pair it to the corresponding singlet.

When two singlet signals are on one side and one singlet is on another side, we consider it to be described in one of the following circumstances. The double-hit situation is when two particles in separate strips on one side hit only one strip on another side. Another corresponds to the hit on one of the strips giving no output signals due to either a problem of electronics or strips with broken wire bonds. These situations can be identified and proper matching can be done according to the signal energies. The same principles are applied for the more complicated situation, for instance two doublets and three singlet signals. After the pairing process, the discrepancy in calibrated energy between EF and EB for almost all particles is less than ±0.5 MeV. This is one of the constraints used in the data analysis. In addition to the particle position and energy, the real multiplicity in each telescope can also be determined after the pixelation procedure.

4.2.7 Identification of Particles with HiRA

One of the main purposes of HiRA is the identification of light charged isotopes. This is done by employing the ΔE-E technique. This technique relies on the dependence of energy loss of charged particles on their energy E, charge Z and mass A, as well as the thickness of the material Δx. Charged particles passing through matter lose energy according to the Bethe formula:

$$-\frac{dE}{dx} = \frac{4\pi n Z^2}{m_e c^2 \beta^2} \left(\frac{e^2}{4\pi\epsilon_0}\right)^2 \left[ln\left(\frac{2m_e c^2 \beta^2}{I(1-\beta^2)}\right) - \beta^2\right] \tag{4.1}$$

where n is the electron density, Z is the chrge number of the particle, $\beta = v/c$, and I is the average excitation potential of the material. For lower charged particle speeds $\beta << 1$, or as in the case of deuterons in the present experiment $0.2 < \beta < 0.3$, and taking intow account that $\beta^2 \propto E/A$ at nonrelativistic energies, this equation can be approximated using the leading order term:

$$\Delta E \approx \frac{kAZ^2}{E}\Delta x \tag{4.2}$$

The energy loss of a particle in a thin detector is inversely proportional to its energy. For particles with the same A and Z, a plot of ΔE versus the remaining energy E will look like $f(E) = \lambda/E$ inverse function plot, where λ is uniquely defined by A and Z. Thus each species of particles will form a unique band. This is demonstrated by DeltaE-E particle identification plot using the thin DE and thicker E detectors in Figure 4.11. To make sure that the particle has not punched through the DSSD, the CsI(Tl) crystal behind the pixel is checked to have no associated event in it, or it is used as a "veto" for punch-through particles.

HiRA has the ability to identify particles in a wide range of energies. This is made possible by the 4 cm thick CsI(Tl) layer, which has a more important role besides being a "punch-through veto". For particles that punch through the E detectors and stop in the CsI(Tl) detectors, the DSSD becomes ΔE and and CsI(Tl) assumes the role of the thick E.

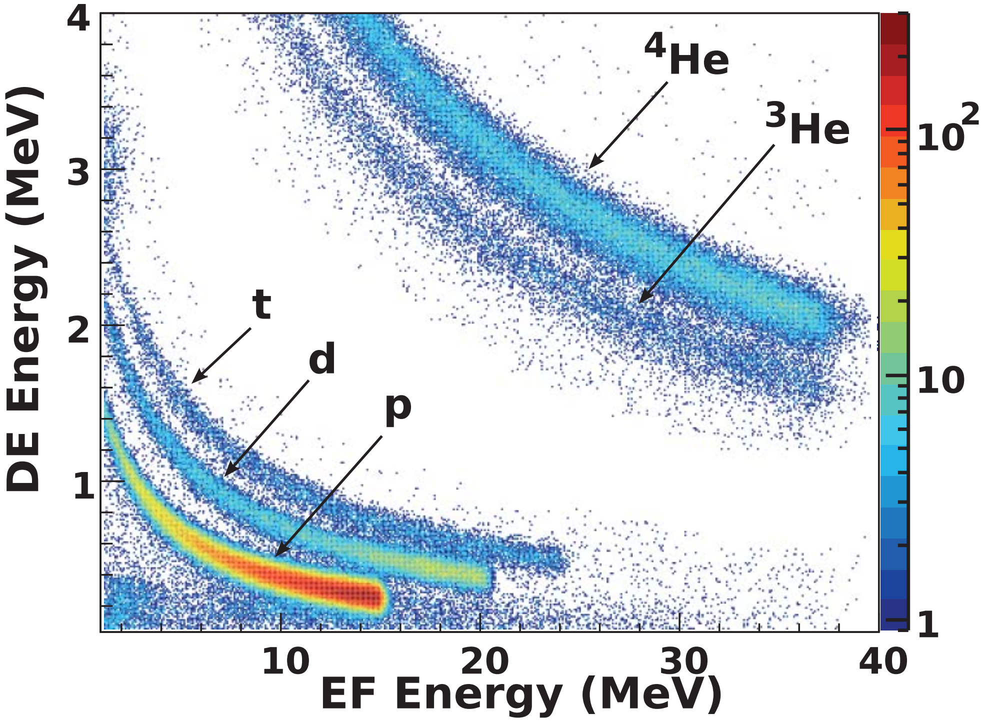

Figure 4.11: HiRA PID with DE and E detectors.

This is demonstrated in Figure 4.12. Gates are drawn around the PID lines in the telescope $\Delta E - E$ and E-CsI two dimensional spectra to select specific isotopes. In this experiment, we are primarily concerned withdeuterons, so the only relevant gate for this dissertation is the deuteron gate.

4.3 S800 Analysis

The S800 spectrometer [56] is used for identification of the heavy residue ^{55}Ni. The identification of the secondary beam particles is performed using ToF-ToF method, described in Subsection 4.3.1. In addition, the non-dispersive position and angle of the reaction residues at the reaction target is calculated using the CRDC1 and CRDC2 positions at the focal plane of the spectrometer. The procedure of calibrating the CRDCs is explained in Subsection 4.3.2.

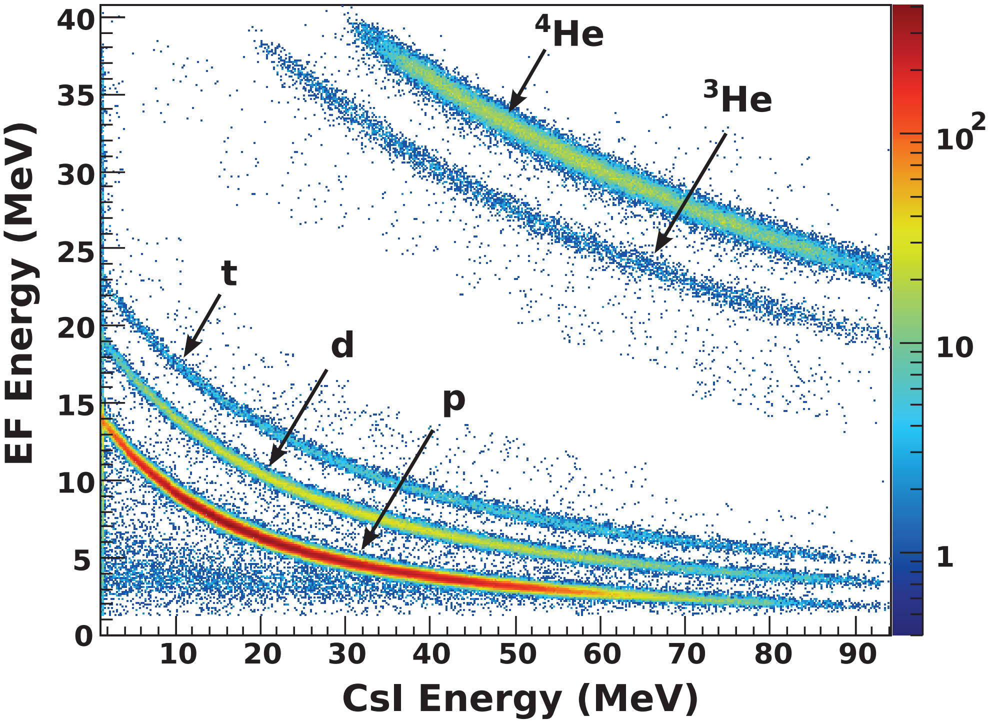

Figure 4.12: HiRA PID with E and CsI(Tl) detectors.

4.3.1 Identification of Secondary Beam Particles

The secondary beam consisted of about 70% ^{56}Ni, the main contaminant being ^{55}Co. ^{56}Ni isotopes were separated from other beam particles by means of the ToF-ToF method, the times used being the A1900 extended focal plane scintillator time, and cyclotron RF time signals relative to the S800 focal planex. As can be seen from Figure 4.13, which shows the beam identification plot used in the analysis, ^{56}Ni isotopes can be clearly identified and separated from contaminants in the beam.

4.3.2 CRDC Calibration

As described in subsection 3.4.1, the CRDC's provide position information in the focal plane that is used to calculate the energy, non-dispersive position and angle of the reaction residue

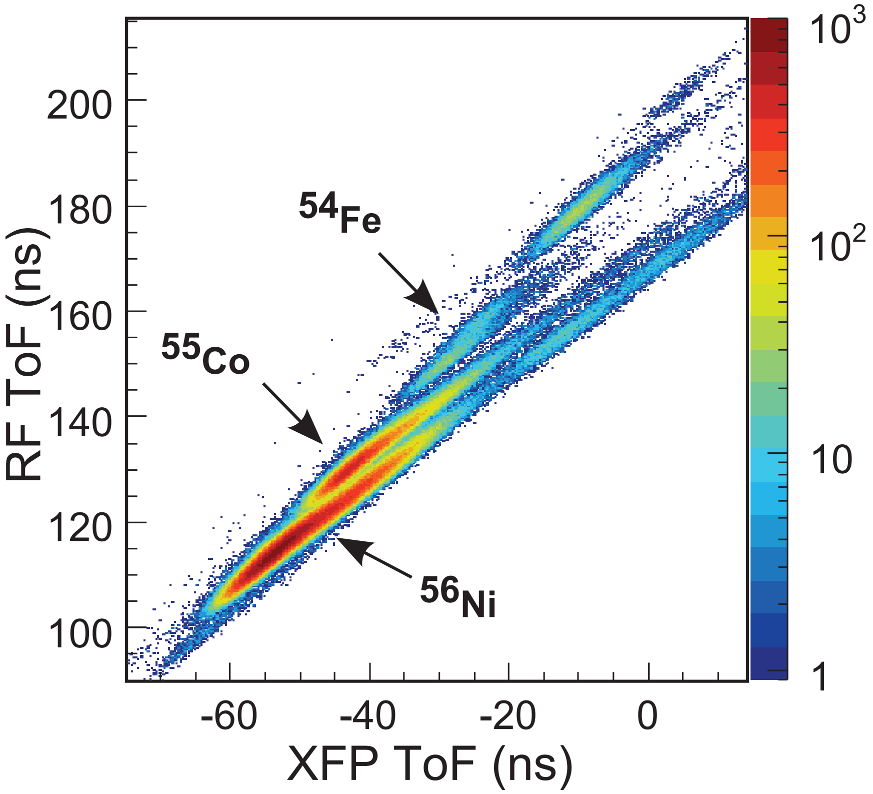

Figure 4.13: Identification of beam from RF-XFP times.

at the reaction target position. In order to relate the CRDC signals to real positions, a mask is inserted in front of the CRDC that is being calibrated. A diagram of the mask is shown in Figure 4.14. The mask contains a pattern of holes and lines covering the entire area of the CRDC. The holes and lines are made asymmetric in both horizontal and vertical directions, in order to unambiguously identify the orientation of the mask in the process of calibration.

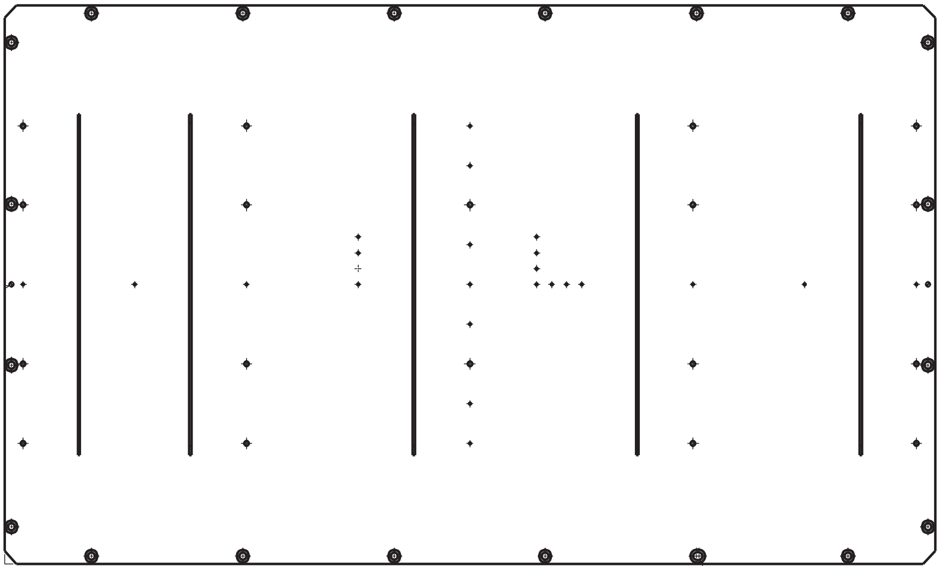

Figure 4.14: A schematic diagram of the CRDC masks.

The raw signals are then converted into real positions in units of mm by calculating the centroids of the holes and linear fitting to match the known positions of the holes. Figure 4.15 shows the calibrated position spectrum of CRDC1.

4.3.3 Identification of Reaction Residues

The time of flight from the downstream MCP to the S800 focal plane, as well as the energy loss in the S800 focal plane ionization chamber were used for identifying the isotopes. The outgoing isotopes are clearly identified as shown in Figure 4.16. The time of flight was

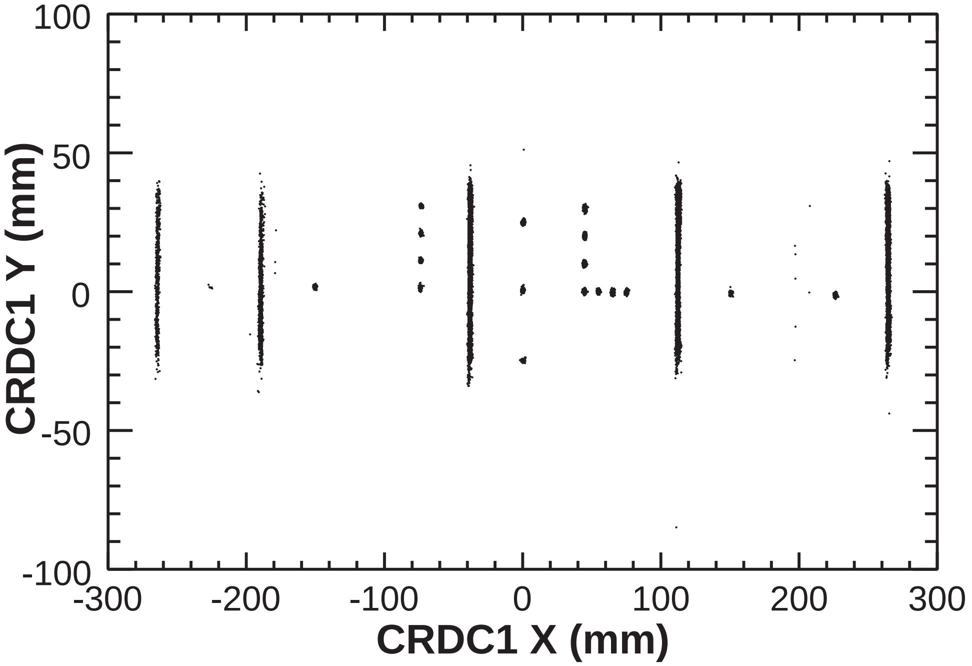

Figure 4.15: Calibrated CRDC1 mask data.

corrected for the differences in the flight length using the CRDC detectors in S800, which measure positions and angles on an event-by-event basis. The ion chamber ΔE was corrected for dependencies on the position and angle in the focal plane, so that all the particles of the same species will have the same energy independent of the focal plane angle and position.

The ToF-ΔE technique allows us to identify particles for the following reasons. For simplicity, we will not take into account the relativistic effects. First, let us look at the y-axis of the spectrum, ΔE. From Equation 4.2 one can see that

$$\Delta E \propto \frac{Z^2}{v^2} \tag{4.3}$$

where v is the particle velocity. The particles move in curved trajectories with nearly constant magnetic rigidities. Derived from the well known Lorentz force and acceleration of particles

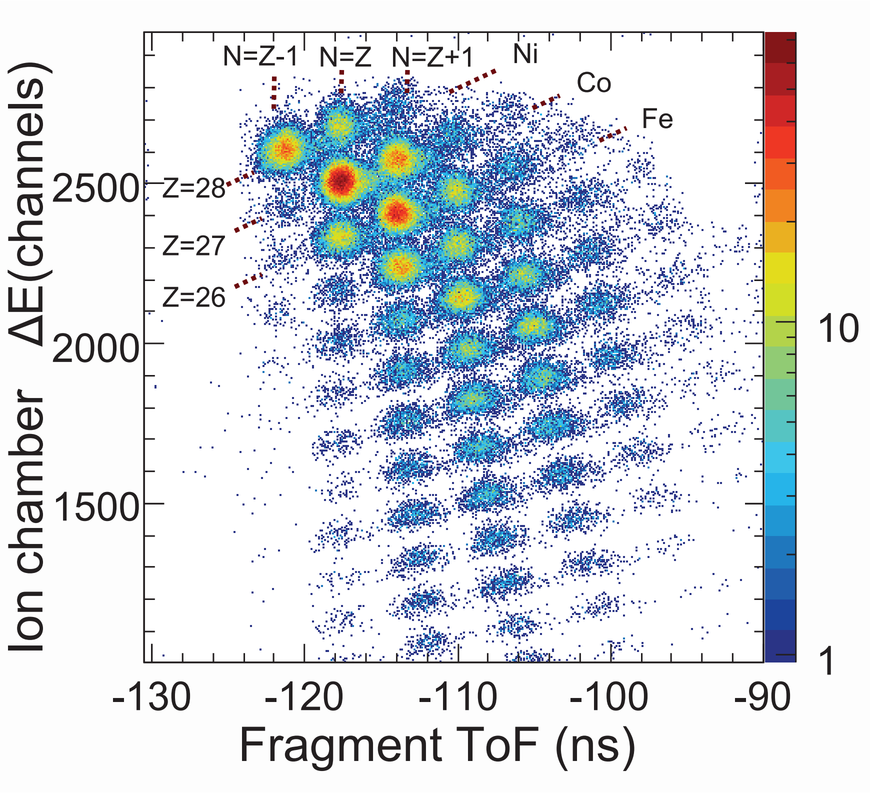

Figure 4.16: Particle identification with S800

in a circular motion, the magnetic rigidity is related to the particle charge, mass and velocity by the following equation,

$$B\rho \propto \frac{Av}{Z} \tag{4.4}$$

where $B\rho$ is the magnetic rigidity. Since $B\rho$ may deviate only about 3% from the average value, we can assume it is constant for our considerations. Thus, replacing Z in Equation 4.3 with Av, we come to

$$\Delta E \propto A^2 \tag{4.5}$$

Thus, for a limited range of $B\rho$, ΔE is proportional to A^2.

Now let us look at the x-axis of the spectrum, the ToF. The ToF is inversely proportional to the velocity v of the particle. Since $Av \propto Z$, $v \propto Z/A$. This leads to $v \propto A/Z$. Thus, with the rough approximations that we have made, we come to the conclusion that ΔE-ToF spectrum approximately gives a 2D spectrum of A^2 vs. A/Z. In this spectrum, one can unambiguously identify one isotope from others.

4.3.4 Energy Loss and Time of Flight Corrections for Focal Plane Position and Angle Dependencies

Since Bρ is not exactly a constant, we make a correction to take this into account. We do this by compensating for the Bρ dependency for both the ion chamber energy and the time of flight. Since Bρ has a linear correlation with the CRDC position, effectively we remove the dependency of energy and time on CRDC1 and CRDC2 x (dispersive) positions, as shown in Figure 4.17.

We also remove the dependency of the ion chamber energy loss and the time of flight on focal plane x and y angles. For the ion chamber the path length, thus the energy loss, of a traversing particle depends on the angle at which it crosses the ion chamber. For the time of flight the path length of the particle depends on the focal plane position and angle in dispersive and non dispersive directions , thus we need to remove these dependencies by correcting them. Figure 4.19 shows the corrected and uncorrected ion chamber energy loss vs. focal plane dispersive angle profile plots. The dependence of time of flight on the focal plane dispersive and non-dispersive angles is removed in the same way as for the position dependence. Figure 4.18 shows the corrected and uncorrected time of flight vs. focal plane dispersive angle profile plots.

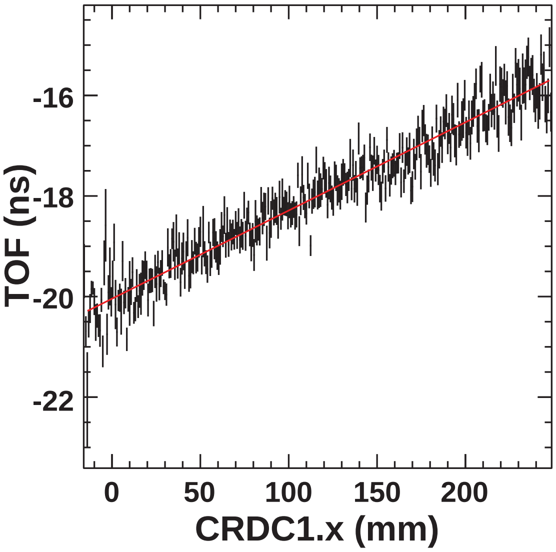

(a) Uncorrected time of flight

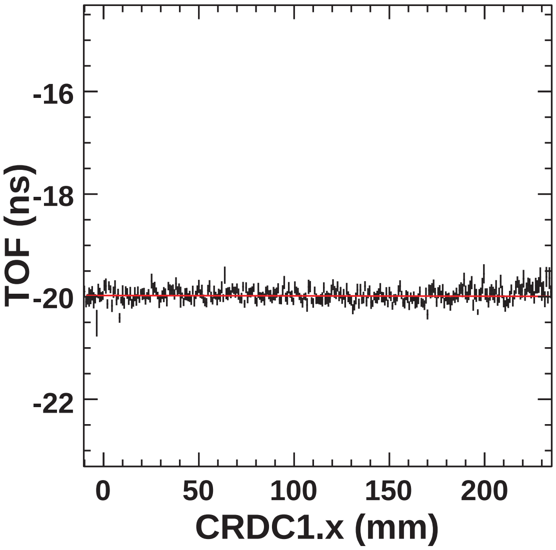

(b) Corrected time of flight

Figure 4.17: Profiles of uncorrected and corrected times of flight vs. focal plane dispersive angle. After correction the dependency on the focal plane angle is removed. The red lines are linear fits to the profiles.

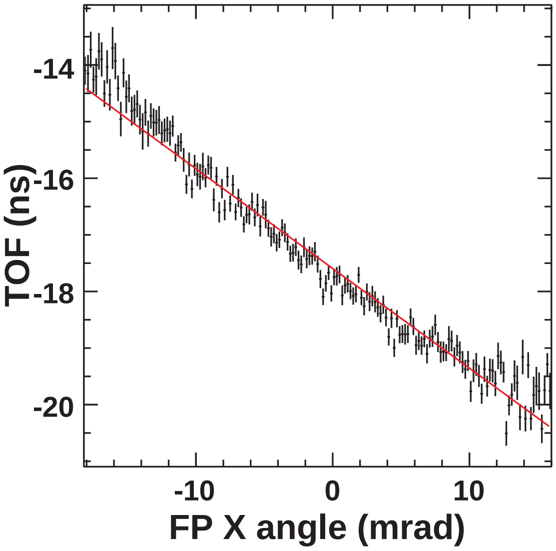

(a) Uncorrected time of flight

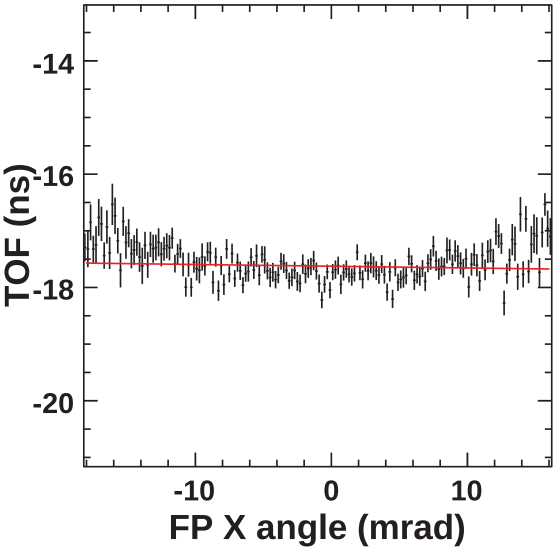

(b) Corrected time of flight

Figure 4.18: Profiles of uncorrected and corrected times of flight vs. CRDC1.x. After correction the dependency on the CRDC1.x position is removed. The red lines are linear fits to the profiles.

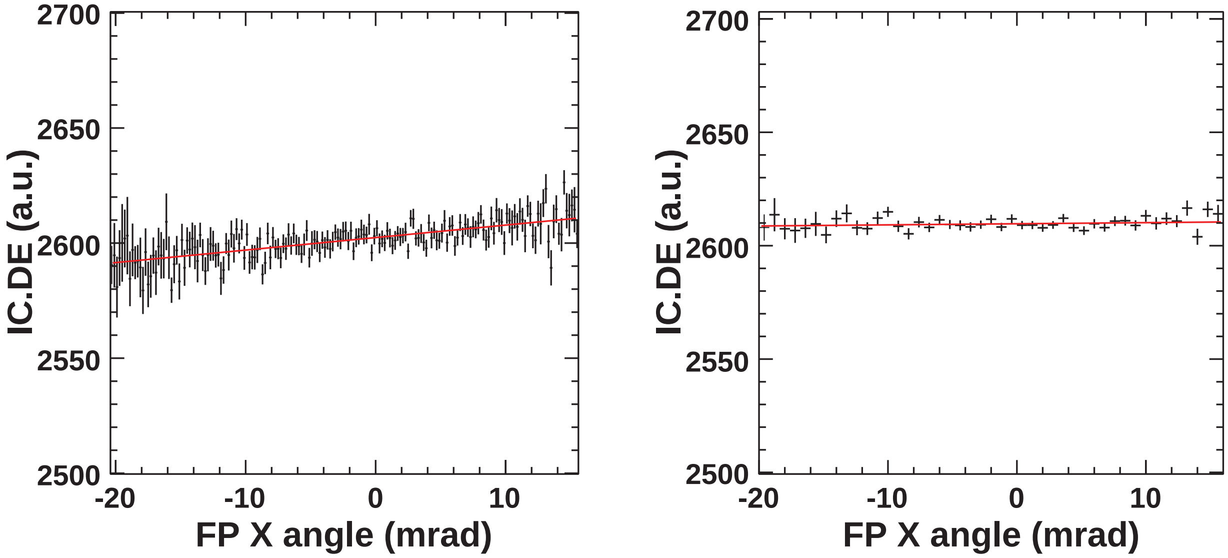

(a) Uncorrected IC energy loss

(b) Corrected IC energy loss

Figure 4.19: Profiles of uncorrected and corrected times of flight vs. CRDC1.x. After correction the dependency on the CRDC1.x position is removed. The red lines are linear fits to the profiles.

4.4 MCP Analysis

Careful calibrations with a cartesian mask placed in front of the MCP foil are required to obtain optimal performance of the MCP tracking detectors. Fig. 4.21 shows a 0.155 mm thick brass target mask containing a matrix of holes is used to map the raw corner signals to physical Cartesian coordinates. A 290 μg/cm^2 aluminized Mylar foil is attached to the mask. Both are mounted on an insulating fiberglass composite ladder and biased to ∼1000 V, providing the electric field that accelerates the secondary electrons ejected from the foils. The smaller holes in the mask have a diameter of 1 mm. The L-shaped pattern on the mask, composed of 2 mm holes, serves to confirm the identity of each hole in the mask.

This mask was used for position calibration with a ^{228}Th source and with rare isotope beams as discussed below. Neither alpha particles nor the beam ions suffer significant energy losses in the foil. The ^{228}Th source emitted alpha particles with energies ranging from approximately 5.4 MeV to approximately 8.8 MeV, which will stop in the mask. Coincidence measurements with a plastic scintillator paddle placed on the opposite side of the mask from the ^{228}Th source source allowed us to identify the alpha particles that pass through holes in the mask. The mask cannot stop the beam, but will degrade the energy of beam ions sufficiently that beam ions passing through the holes in the mask can be distinguished by their magnetic rigidity. Coincidence measurements of beam particles in the NSCL S800 spectrometer [56], downstream of the target, allowed us to select the beam particles that pass through the holes in the mask. Another mask was used calculation of the beam position at the target.

We employ charge division techniques to obtain the raw (uncalibrated) horizontal X_{raw} and vertical Y_{raw} coordinates of the point of interaction on the target from the four resistive anode outputs of the MCP as follows:

$X_{raw} = (UL + LL - UR - LR)/(UL + UR + LL + LR)$

$Y_{raw} = (UL - LL + UR - LR)/(UL + UR + LL + LR)$.

In this section we describe the calibration procedures for converting these raw coordinates into the final (calibrated) horizontal X and vertical Y coordinates of the point where the beam ion interacts with the target.

4.4.1 MCP mask calibrations

Each of the anode corner signal amplitude is proportional to the number of secondary electrons produced in the micro-channels and inversely proportional to the resistance between the point where the charge is deposited on the resistive layer and the corner where the electrode is located. Thus the amplitude of a corner signal will be greater if the deposition is close to that corner. Conversely, it will have a lower amplitude if the signal originates from a point farther away. At high rates or with older channel plates, regions of the MCP, that experience the highest counting rates, tend to produce significantly smaller signals. To account for the differences in the signal amplitudes, we introduce in the signal electronics both low gain and high gain anode signals that differ in amplification by a factor of 8×. These two gain stages are matched with a precision pulser and this matching is checked with the experimental data.

The upper and lower panels in Figure 4.20 shows anode spectra for two different corners; the dashed histograms show the high gain spectra and the solid histograms show the low gain spectra. These two gain stages are matched with a precision pulser and this matching is checked with the experimental data. In the following analyses, the lowest amplitude signals are generally taken from the high gain channel. There is a region indicated in Figure 4.20 where we linearly interpolate between the low gain and high gain signals, and above that the low gain signals are used exclusively. In the upper panel, the low gain signal had a large negative pedestal value, but high gain channel made the loss of dynamic range of negligible importance. With new MCPs and carefully adjusted pedestals, one can usually achieve the performance illustrated in the lower panel, where an additional high gain stage is helpful but not critical to achieve reasonable performance of the MCP tracking detector.

Transforming the uncalibrated position spectra into calibrated physical Cartesian positions consists of the following steps:

1. Pedestals, or channels corresponding to signals with zero amplitude, are initially taken by a pedestal run and subtracted from the raw data. Specifically, pedestal subtractions are done to reset the average values for the QDCs for the UL, UR, LL and LR channels to zero when signals are not present.

2. Final pedestal values are determined by incrementing and decrementing the estimated

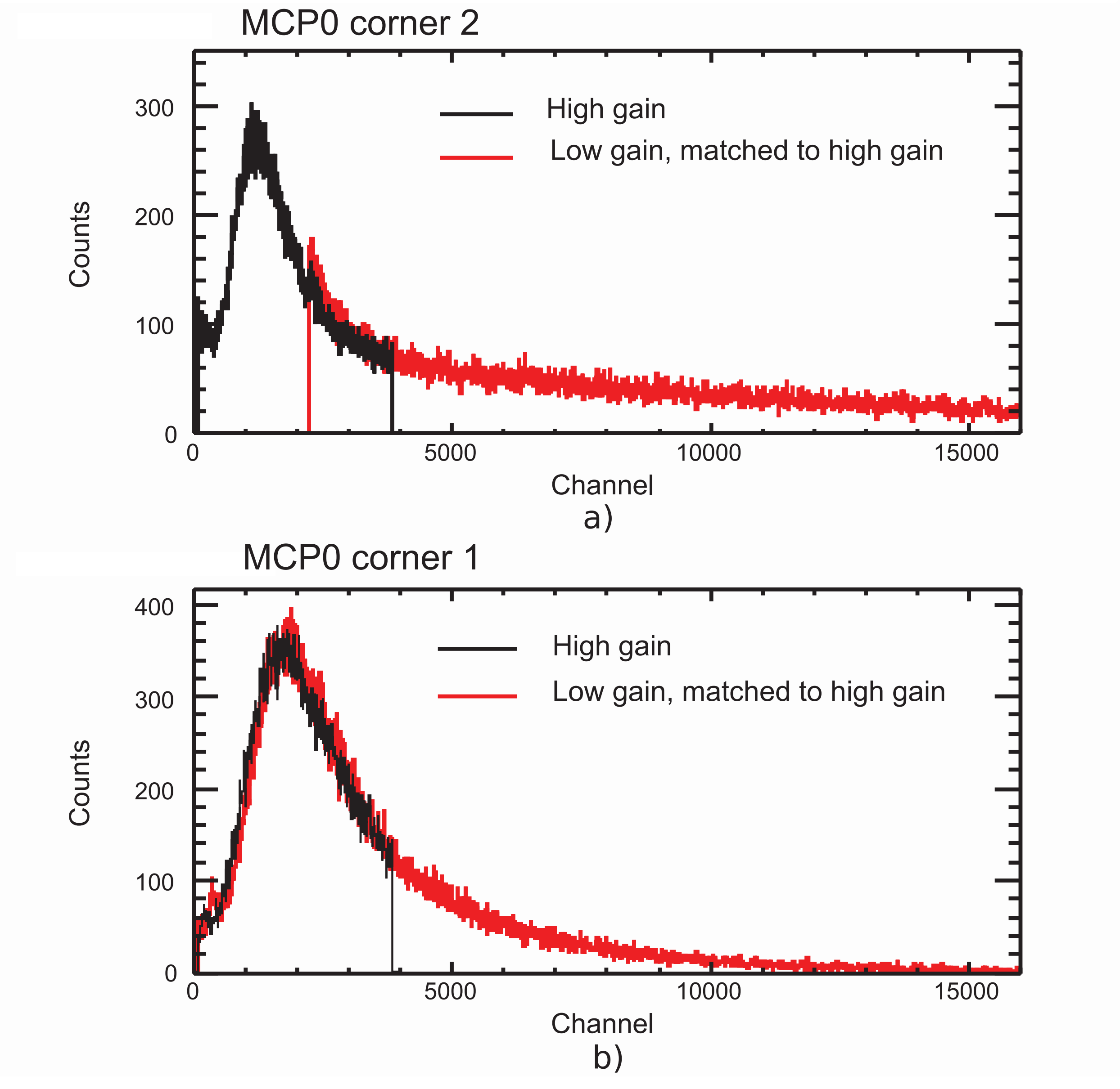

Figure 4.20: The high-gain and low-gain signals from one corner of MCP1.

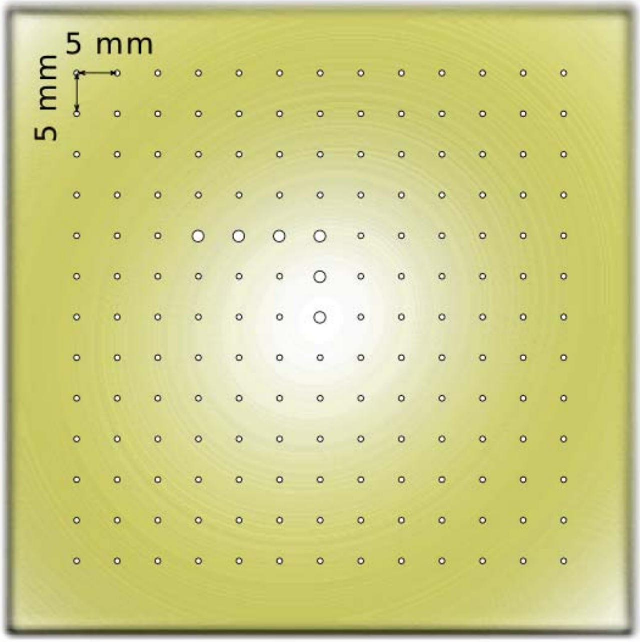

Figure 4.21: A diagram of an MCP mask used for position calibration.

pedestal values to find the pedestals that minimize the dependence of the calculated position of specific holes in the calibration mask on the sum of the corner signals. Typically, the pedestal settings affect position spectra in the center of the MCP near the beam spot more severely since this is the region where the smallest corner signals are generated. The small signals at the center result partly from radiation damage to the MCP and from loading of the MCP caused by the beam rate. Fig. 4.22a shows the position spectrum for one of two MCPs, labeled MCP1, after the completion of step 2. The L-shaped pattern corresponding to the larger holes in the calibration mask is rotated clockwise with respect to the mask. In addition, the spacing between each neighboring holes, is not consistent with a uniform spacing of 5 mm.

3. A 3rd-order 2 dimensional polynomial is used to fit the raw position information to the mask pattern, and optimized to correct the uncalibrated positions to match the known

physical positions of the holes on the mask shown in Fig. 4.21.

$$\begin{aligned} X_{cal} &= X_{raw} - a_1 + a_2 X_{raw} + a_3 Y_{raw} \\ &+ a_4 X_{raw}^2 + a_5 Y_{raw}^2 + a_6 X_{raw}^3 + a_7 Y_{raw}^3 \\ &+ a_8 X_{raw} Y_{raw} + a_9 X_{raw}^2 Y_{raw} + a_{10} Y_{raw}^2 X_{raw} \\ Y_{cal} &= Y_{raw} - b_1 + b_2 Y_{raw} + b_3 X_{raw} \\ &+ b_4 Y_{raw}^2 + b_5 X_{raw}^2 + b_6 Y_{raw}^3 + b_7 X_{raw}^3 \\ &+ b_8 Y_{raw} X_{raw} + b_9 Y_{raw}^2 X_{raw} + b_{10} X_{raw}^2 Y_{raw} \end{aligned} \tag{4.6}$$

where X_{raw}, Y_{raw}, X_{cal} and Y_{cal} are the raw and calibrated coordinates respectively and a_i, b_i are the fit parameters. Each calibrated position, X_{cal} and Y_{cal}, is mapped by the function, which takes into account most of the non-linear effects that are observed in Fig. 4.22a.

After fitting, we have the position spectrum in Fig. 4.22b. In the center of the mask, the centroids of the peaks are located to within 0.5 mm of the correct physical positions of the mask. For a few mask holes near the edge of the beam spot, the centroid can be off by as much as 2.0 mm. The widths of the peaks are consistent with a position resolutions of 1.0 mm for the MCP detector. This data was taken with assembly of permanent magnets that create a magnetic field of 0.030 T at the surface of the target foil.

4.4.2 Microchannel Plate Performance in Beam

In this section we describe the performance of the MCPs with rare isotope beams in two experiments, one described in Ref. [77], and the present experiment. The primary differences between the two experiments are the beam energies and the magnetic fields in the MCP assemblies.

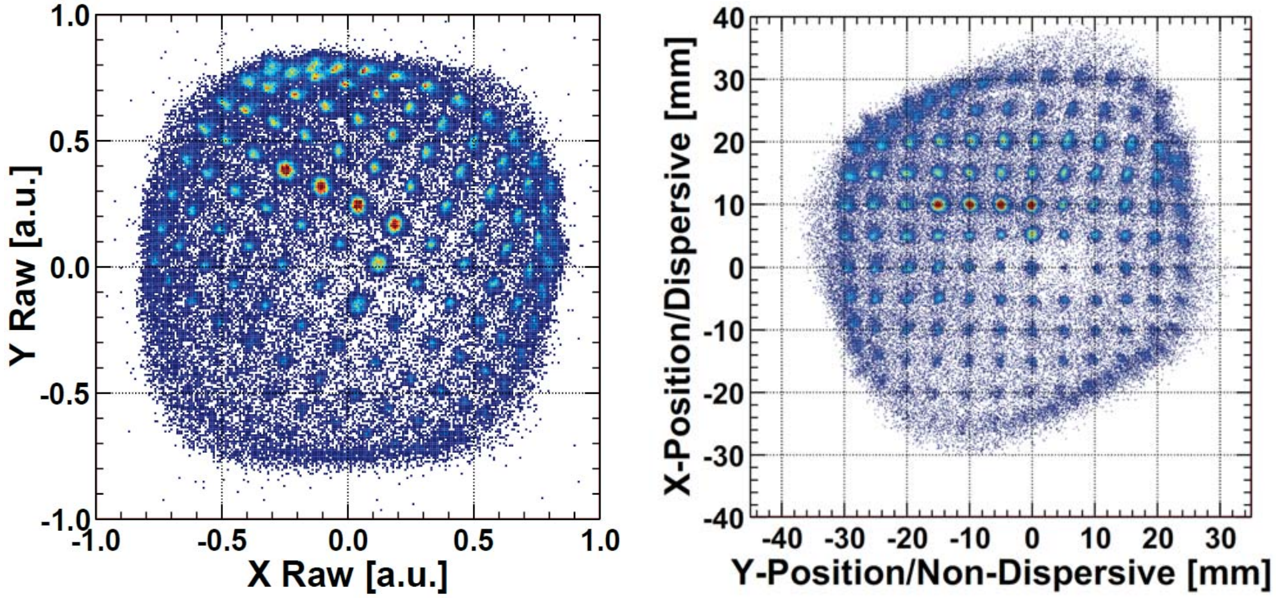

(a) MCP raw α-source calibration (b) MCP final α-source calibration spectrum

Figure 4.22: MCP α-source calibration from Ref. [77] with a 0.030 T magnetic field at the MCP foil.

4.4.3 Calibration with ^{70}Se at 72 MeV/u

The first experiment involved a ^{70}Se beam and utilized the same setup as the alpha source measurements described in the preceding section. In this setup, the magnetic field was supplied by two different sets of permanent magnets as shown in Fig. 3.20. The measured magnetic field attained a value of 0.03 T at the location of the target and increased to 0.05 T at the location of the MCP.

Fig. 4.23, shows the uncalibrated and calibrated mask image of a defocused ^{70}Se secondary beam. In this test, the incoming secondary beam particles arrive at the target with nearly parallel trajectories. Here, the incoming angle is 0°. The trigger for the mask spectrum was the detection of a ^{70}Se ion in the S800 mass spectrograph [56] focal plane detector. Only ^{70}Se ions that pass through the holes in the mask are bent to the S800 focal plane and create a trigger; ^{70}Se ions that go to the 0.54 mm mask itself lose sufficient energy that their subsequent trajectories are deflectedaway from the S800 focal plane detector. The L-shaped pattern of the 2 mm holes, shown in Fig.6 for the alpha particle calibrations, can be clearly seen in Fig. 4.23. The rotation of the L-shape pattern and the non-linear distortion of the hole pattern at the edges of the uncalibrated spectrum, are similar to that observed for the alpha particles in Fig. 6a. As shown by Fig. 4.23b, the calibration straightens this out, rotating the L-shaped pattern to agree with the drawing of the mask and setting the spacing between holes to be the nominal 5 mm spacing expected for the mask.

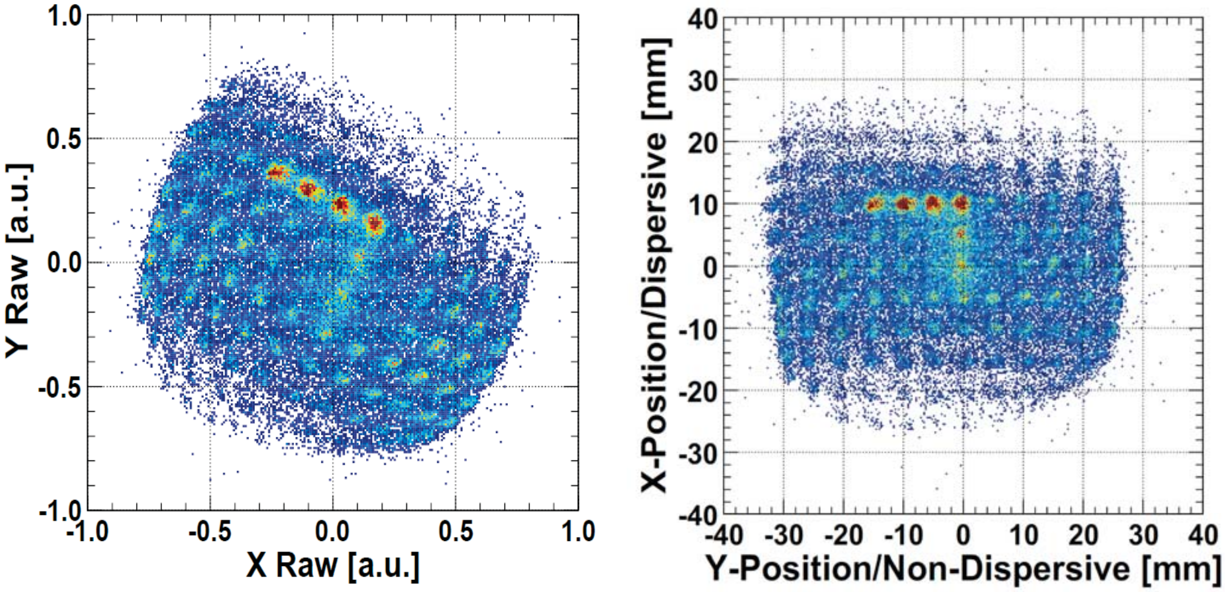

(a) MCP1 raw calibration with beam

(b) MCP1 beam calibration

Figure 4.23: MCP beam calibration from the ^{70}Se experiment [77].

There is a clear difference in the position resolution of the alpha particle and beam mask spectra, with the alpha source spectrum clearly having the better resolution. Specifically, the position resolution for the alpha source spectrum is approximately 1.5 mm FWHM in both the vertical and horizontal directions. If one attempts to unfold the influence of the hole size in the mask, the observed alpha resolution corresponds to an intrinsic resolution of 1 mm. In contrast, the position resolution for the data taken with the ^{70}Se beam is approximately 2.5 mm FWHM in both the vertical and horizontal directions. After unfolding the influence of the hole size in the calibrated mask spectrum, the observed intrinsic resolution for the ^{70}Se beam corresponds to about 2.0 mm FWHM, which is 2 times larger than the observed values for the alpha source.

It is not obvious why the beam exhibits a resolution that is worse than that obtained with the α source. In general, condition for both measurements are similar. The voltage was adjusted to make sure that range of signal amplitudes are comparable to each other. The beam counting rate was higher, but there was no evidence of a dependence of the resolution on beam rate during calibrations. Moreover, the rate dependence was explored by Shapira et al. [57, 58, 79, 80] and no strong dependence of resolution on rate was observed.

One possible difference is the beam energy. The MCPs detect electrons from a variety of sources. Significant contributions come from primary electrons scattered by the beam and from secondary electrons ionized indirectly due to the energy deposition in the target. These secondary electrons have kinetic energies that are small compared to the energy imparted to them by the accelerating potential of -1000 V on the target. In comparison, primary electrons scattered by the beam can have velocities more than twice that of the beam [91]; the relevant energies range from an upper limit, E_{max}, given approximately by elastic scattering kinematics and the lower limit, E_{min}, by the energy-range relationship for electrons [92, 93]. In collisions at 1 MeV/u, the primary electrons rarely exceed 1 keV in energy. In U+U collisions at incident energies of 10 MeV/u, on the order of 6 electrons are emitted at energies in excess of 1 keV, and the mean energy of these electrons is 2 keV [94]. Both the maximum and average energies of electrons grow with incident energy, the energy for electrons backscattered from the ^{70}Se beam at $E/A = 72MeV$ is about 170 keV. From the Mott scattering cross section, one can estimate the mean energy of primary electrons to be approximately $\langle E \rangle \approx E_{min} ln(E_{max}/E_{min})$. As the Mott cross section for such electrons is large, multiple scattering for such electrons can even lead to the scattering of some high energy electrons from the target foil to backward angles.

Electrons emitted from the target foil follow roughly helical orbits from the target to the MCP [57, 58]. Assuming the magnetic field varies slowly on the scale of this radius, the motion can be assumed to be adiabatic and the final radius will be given by $r_{MCP} = r_{foil} \cdot (\frac{B_{foil}}{B_{MCP}})^{1/2}$, where r_{MCP} and B_{MCP} are the orbital radius and magnetic field at the MCP and r_{foil} and B_{foil} are the radius and magnetic field at the target foil.

For the data in Figs. 4.22 and 4.23, the magnetic field in the MCP assembly has values of $B_{MCP} = 0.050T$ and $B_{foil} = 0.030T$. The initial orbital radius r_{foil} is determined by the component of the electron momentum perpendicular to the magnetic field. Since the most energetic electrons will be preferentially emitted close perpendicular to the magnetic field, we approximate the average electron momentum by $p_{\perp} \approx \sqrt{(}2m_e\langle E \rangle)$. For collisions involving the ^{70}Se beam at $E/A = 72MeV$, we estimate the mean scattered electron energy to be approximately 12 keV and the FWHM contribution to the position resolution to be about 1.6 mm FWHM. For collisions at E/A=1 MeV comparable to the work of Shapira et al. [57, 58], or for the case of an alpha source, in comparison, we estimate that the mean scattered electron energy would be about 1 keV and the FWHM contribution to the resolution to be about 0.4 mm FWHM. Clearly, the increase of scattered electron energy with beam energy can contribute to a worsening of the position resolution of the channel plate tracking detector.

To further explore the influence of the primary electrons on the resolution, we used these MCPs in another experiment involving a ^{56}Ni beam at 37 MeV/u. In this case, there were two MCP tracking detectors. Each tracking detector was equipped with a stronger magnetic field. The field was provided by two permanent magnets [Magnet Sales & Manufacturing Inc, part number: 35 NERR192x2.0 NSSM]; together they provided a magnetic field measured at the MCP and the MCP foil positions of 0.21 and 0.127 T respectively, approximately 4x that of the preceding the preceding measurements. Lowering the beam velocity, we estimate the mean scattered electron energy to be approximately 12 keV and with the increased magnetic field, the FWHM contribution to the position resolution is estimated to be about 0.34 mm. The contribution of the primary electrons to the resolution for this second setup, with its larger magnetic field, is significantly smaller, suggesting that the observed position resolution for this setup should be much better than for the previous setup.

Fig. 4.24 displays the calibrated mask spectra for two MCPs. The observed position resolutions for these spectra is 1.6 mm for the smaller holes, which is significantly better than the observed resolution for the ^{70}Se beam. If one attempts to unfold the influence of the hole size in the mask for the ^{56}Ni beam, the observed resolution for the ^{56}Ni beam corresponds to an intrinsic resolution of 1.1 mm. This is significantly better than that for the ^{70}Se beam, providing support for the assumption that increasing the magnetic field can compensate for presence of increasingly energetic primary electrons at the higher incident energies. The improvement is comparable to our estimates given above. Using the resolutions of each MCP we calculated an MCP angular resolution of 0.23°.

4.4.4 Calibration of the MCPs in the Present Experiment

The angle for the ^{56}Ni(p,d)^{55}Ni reaction depends on to position where the reaction occurs in the target and on the direction of the momentum of the incident ^{56}Ni just before the reaction. To constrain these quantities, an MCP tracking system was used. This MCP tracking system employed two Micro Channel Plate tracking detectors, MCP0 and MCP1. They were placed at 50 cm apart, with MCP0 and MCP1 denoting the upstream and downstream MCPs respectively. The reaction target was located at 10 cm downstream of the MCP1. As shown in Fig. 3.20 and described in the tests described above, each tracking detector and target was rotated by 60° with respect to the beam, so that the permanent magnets associated with these detectors do not block the incoming particles.

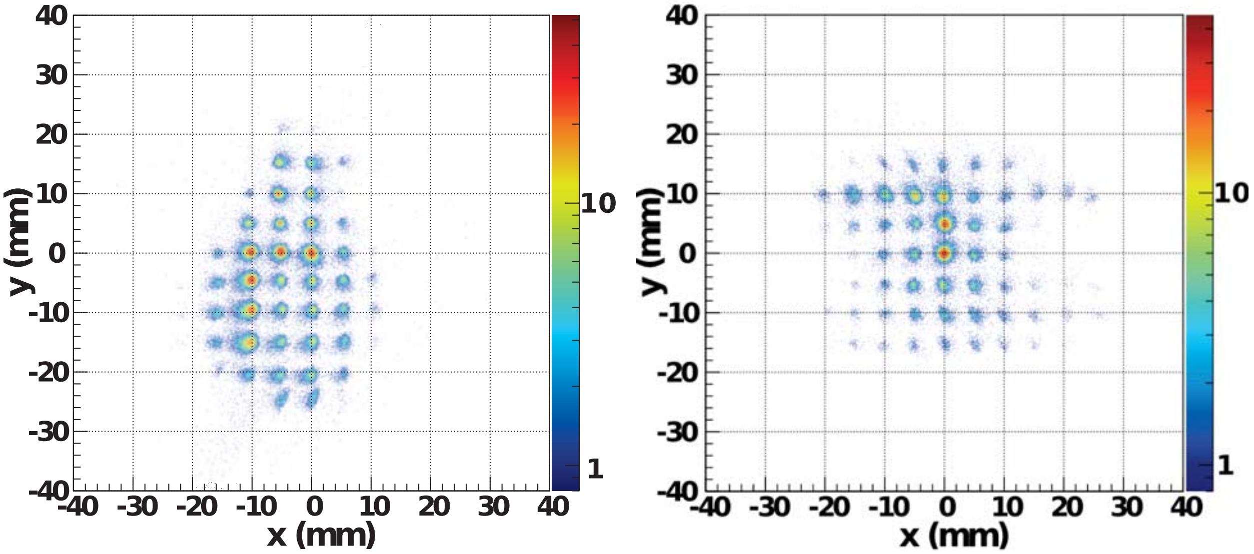

(a) MCP0 beam calibration

(b) MCP1 beam calibration

Figure 4.24: MCP calibration from the present experiment. Combination of slower beam and stronger magnetic field results in a better position resolution.

The strong magnet fields in the MCP setup influence the trajectories of the ^{56}Ni beam ions. If the beam initially travels horizontally, the first MCP magnet deflects the beam by an angle of $\theta = Bdsin\gamma/B\rho$. Here, B is the magnetic B-field at MCP foil (∼0.13 T), d is the distance the beam traveled in the B-field (∼8 cm), γ is angle of the foil with respect to the normal (60°) and Bρ = 1.72 Tesla·m is the magnetic rigidity of the beam. The estimated deflection angles are therefore about 0.17° for ^{56}Ni. To compensate for this deflection, the magnetic fields in the two MCPs were in opposite direction with respect to each other, in order to avoid changing the angle of the beam. In this configuration, the main effect of the two magnets on the beam is to shift it upward by 1.5 mm which is negligible compared to the beam size. This shift is of no consequence as long as it is small, because the experiment only depends on the position and angle of the beam at the target, not on its position upstream before the MCPs.

Fig. 4.24 showed the mask image of secondary beam ^{56}Ni at the foil position in the ^{56}Ni experiment setup. The 60° rotation of the target foil means that 0.5 times the horizontal position measurement is the horizontal displacement perpendicular to the beam axis. Thus, the horizontal displacement perpendicular to the beam is measured with resolution of approximately 0.8 mm in the horizontal position, which is better than the 1.6 mm resolution of the vertical position.

4.4.5 Determining the location of the beam on the target

Beam angles and positions on the reaction target are deduced from the measured positions in MCP0 and MCP1 using simple geometry, based on the assumption that the deflection on the trajectories of ^{56}Ni beam due to the magnets in MCP detection systems is small. To evaluate the uncertainties of the calibration procedure on the target, we inserted a mask in the reaction target position. The mask is made out of 1.56 mm thick aluminum plate with five 2 mm holes, as shown in the schematic diagram of Fig. 4.25. The four outer holes form a square with 10 mm sides. A fifth hole is located at the center.

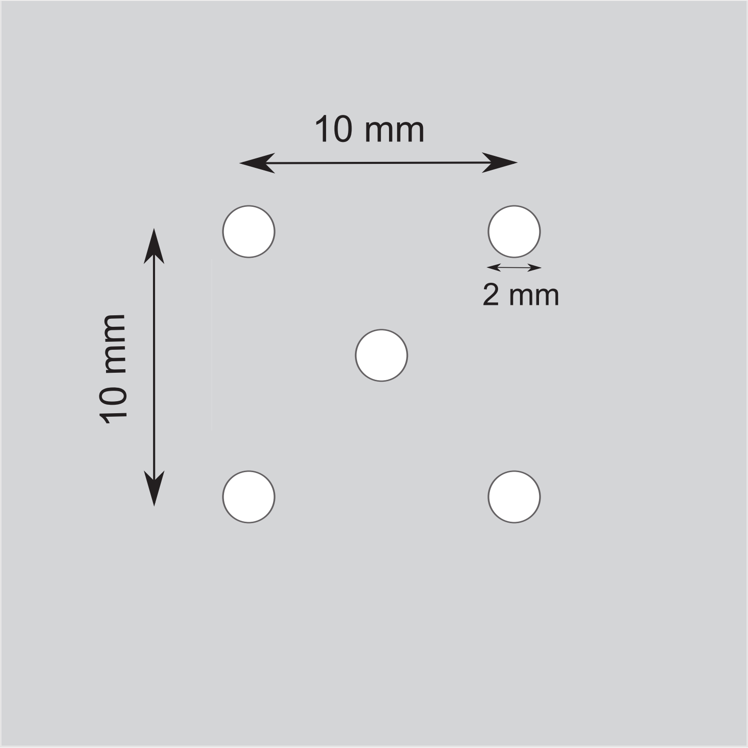

Figure 4.25: A schematic view of the target mask.

To check the ability of the MCP calibrations to determine the beam spot on target, we compare the point of interaction on the target calculated using the MCP position measurements and the experimental geometry to the drawing of the target mask. This is shown in Fig. 4.26. The calculated beam spot matches the target mask reasonably well, but the resolution of reconstructed positions on the target is worse than the position resolution shown on either mask calibration. The resolution is comparable with the resolution calculated by propagation of errors from the two MCPs and positions of target mask and MCP foils. For the outer holes, the resolutions are 1.2 mm in the horizontal direction and 1.5 mm in the vertical direction. The difference in the resolution is due to the rotation of the MCP foils. However it is not uniform and is somewhat worse in the center of the target center, corresponding to 2 mm resolution in the vertical direction, and it appears to be somewhat worse on the right hand side of the target. The average resolution of 1.5 mm is comparable to the pitch of the silicon strip detectors.

Fig. 4.27 shows the ^{56}Ni beam position spectrum on target obtained by extrapolating the positions at two MCPs. Typical beam spots of secondary beams such as ^{56}Ni have finite size of about 11 mm FWHM in the horizontal direction and 17 mm FWHM in the vertical direction, as shown in Fig. 4.27. Thus, particles produced from reactions happening at the target center and at a position that is 1σ of the beam spot size away from the center would have different scattering angles even if they are detected in the same pixel of the HiRA device. The actual scattering angle also has contributions coming from the range of incident angles for the beam on the reaction target. Fig. 4.28 show the calibrated spectrum of incident angles at the reaction target. The angular distributions have widths of $\delta\theta_{beam-horizontal}$=1.5° FWHM and $\delta\theta_{beam-vertical}$=1.35° FWHM. Folding the beam angle distribution against the target spot size distribution, one has $\delta\theta_{total-horizontal}$=2.3° FWHM and $\theta_{total-vertical}$=3.0°, respectively. We have superimposed the mask positions on the spectrum. By comparing Figs. 4.26 and 4.27, one can see that the resolution of the tracking system is about a factor of 10× better than the width of the beam spot. One should therefore be able to improve the resolution in experiments for which the target beam spot or beam angular resolution is a critical issue.

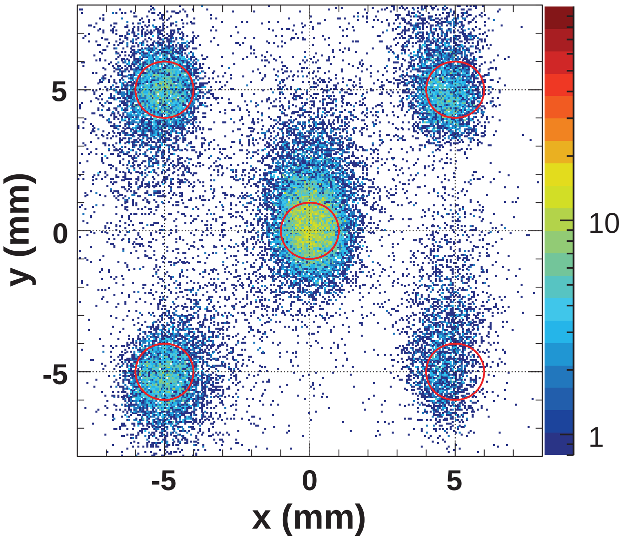

Figure 4.26: Calculated position at the reaction target using MCP positions.

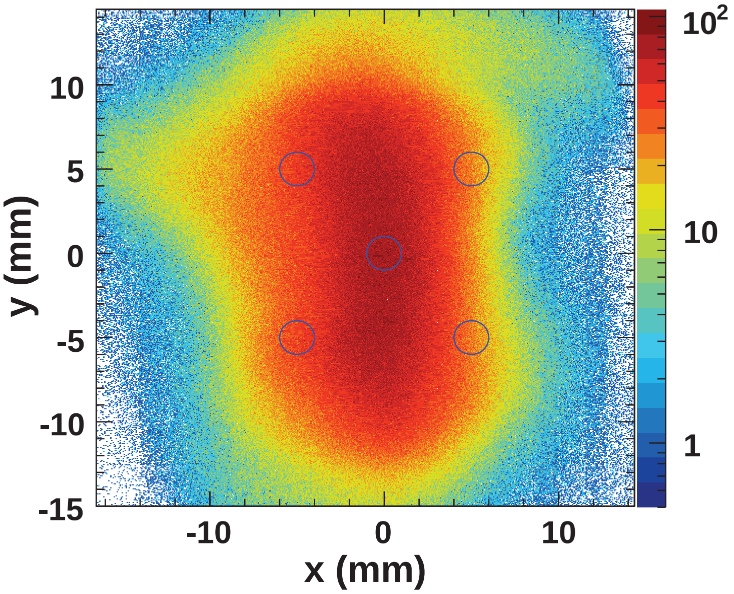

Figure 4.27: Beam position spectrum on target of ^{56}Ni. The circles show the target mask holes in Fig. 4.26.

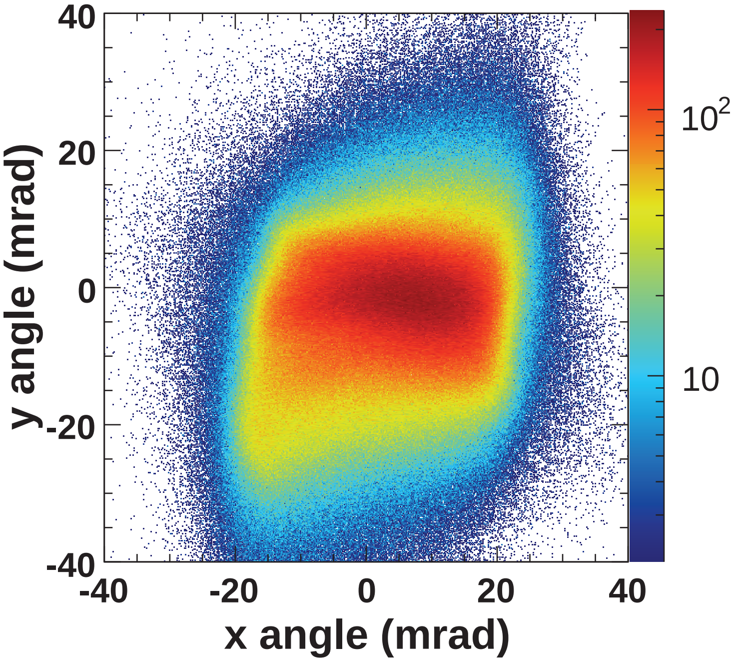

Figure 4.28: Beam angle spectrum on target of ^{56}Ni.

Chapter 5

Experimental Results

To obtain the differential cross sections and consequently the spectroscopic factors of the ^{56}Ni(p,d)^{55}Ni reaction, measured data from the three detector systems are processed separately and then assembled together to provide relevant experimental observables. In this chapter, we describe the procedures for extracting those observables in Sections 5.1, 5.2 and 5.4, as well as the background subtraction in Section 5.3. Factors involved in absolute normalization of the differential cross sections and their uncertainties are discussed in Subsection 5.4.1. Also discussed in Section 5.5 is the structural information on the populated states of ^{55}Ni such as spectroscopic factors, angular momentum and parity. The obtained spectroscopic factors are compared to theoretical spectroscopic factors.

5.1 Reaction Kinematics

After the selection of deuterons in HiRA, ^{56}Ni beam particles from time of flight and ^{55}Ni residues in the S800, the energy of the deuteron and its scattering angle with respect to the beam is used to determine the Q-Value for the ^{56}Ni(p,d)^{55}Ni reaction. Figure 5.1 shows a plot of the deuteron energy versus the angle between the deuteron and beam particle in the laboratory frame. The bands correspond to deuterons in coincidence with various states of the ^{55}Ni reaction residues and the curves are the calculated kinematics according to the excitation energies compiled in the National Nuclear Data Center (NNDC) database [95].

The forward angle portion of the plot is zoomed in and showed in the upper left inset. The observed energy levels in the NNDC database of the recoil residue ^{55}Ni, below 7 MeV, are listed in Table 5.1, with the firm and tentative spin and parity assignments. The tentative spin and parity values are shown in parentheses.

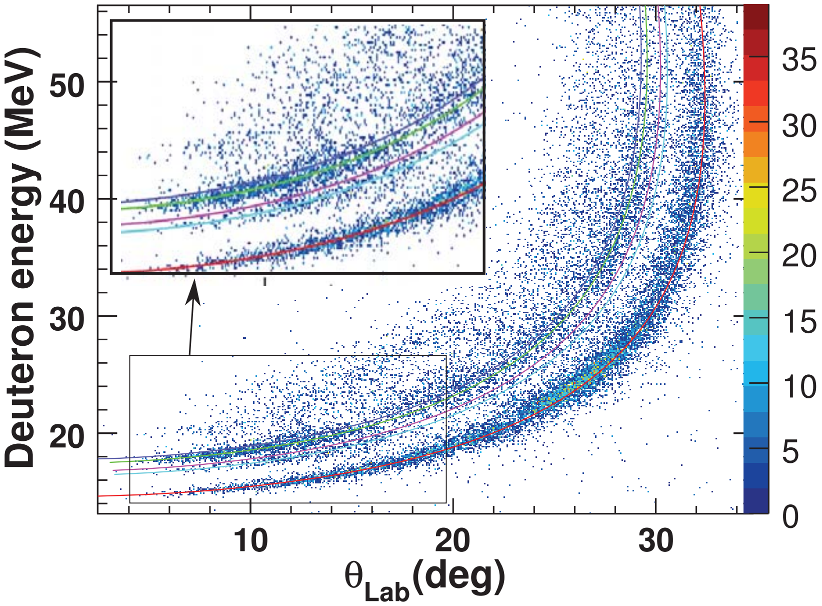

Figure 5.1: Deuteron kinematics for ^{56}Ni(p,d)^{55}Ni in laboratory frame.

5.1.1 Effects of Target Thickness on Resolution

Choosing the target thickness is often done with consideration of event statistics and energy resolution, and this is certainly true for this experiment. Finding the right balance between these two conflicting factors is very important. We chose to optimize the statistics with Q-value resolution sufficient to resolve the ground state of ^{55}Ni.

For this purpose, we used a CH_2 target of 9.6 mg/cm^2 thickness. Before the target, the beam energy was 37 MeV per nucleon. To illustrate the energy spread strictly resulting from the target thickness, we neglect the spread in the beam energy. We can assume a uniform

Table 5.1: Measured energy levels of ^{55}Ni for energies below 7 MeV, with available spin and parity assignments [NNDC].

Energy level (keV)	J^{π}
0	$7/2^{-}$
2089	
2462	
2839	
2882.1	$(11/2^{-})$
3185	$(1/2^{+})$
3502	
3583.1	$(13/2^{-})$
3617.1	$(15/2^{-})$
3752	$(3/2^{+})$
3784	
4046	
4444	
4483.1	$(17/2)$
4616	
4743	
4983	
5178	
5389	
5876	
5937	
6600	
6870	

probability of the reaction happening throughout the target, as the change in energy of the beam is ± 3%. Let us consider two extremes: first, the reaction happens at the entrance of the target, and second, the reaction happens at the exit of the target. For simplicity of calculations and clarity, let us consider the deuterons coming out at a 15° angle. For energy loss calculations, we used LISE++ [88]. In the first case the beam energy is 37 MeV per nucleon, or 2070 MeV total.If the reaction occurs at the front surface of the target, the deuteron energy right after the reaction will be 16.776 MeV. After it passes through the target, the deuteron will have 16.20 MeV kinetic energy remaining. In the second case, when the reaction occurs at the end of the target, the ^{56}Ni beam particle will have 1951 MeV before the reaction. The resulting energy of the deuteron is 16.65 MeV. The difference between the deuteron energies in these two extreme cases is 450 keV. At 15°, this corresponds to a the Q-value or excitation energy resolution of 360 keV FWHM.

For more backward angles, another important factor to consider is the effect of the target thickness on the angular resolution. Figure 5.2 displays the calculated kinematics for the ^{56}Ni(p,d)^{55}Ni showing the effect of the reaction location in target. The dashed red line corresponds to the energy and angle of the deuterons for reactions happening at the entrance of the target, the solid blue line corresponds to the energy and angle of the deuterons for reactions happening at the exit of the target. At the entrance and exit of the target, the energies of the ^{56}Ni beam particles are 2070 MeV and 1950 MeV, respectively. The corresponding maximum angles of deuterons in the laboratory frame are 32.85° and 32.1°, respectively.

Lastly, the angular straggling of deuterons in the thick target is significant. Calculations performed using the computer program LISE show a FWHM angular straggling of 0.52° for deuterons travelling full length of the target [88]. The angular straggling for the ^{56}Ni

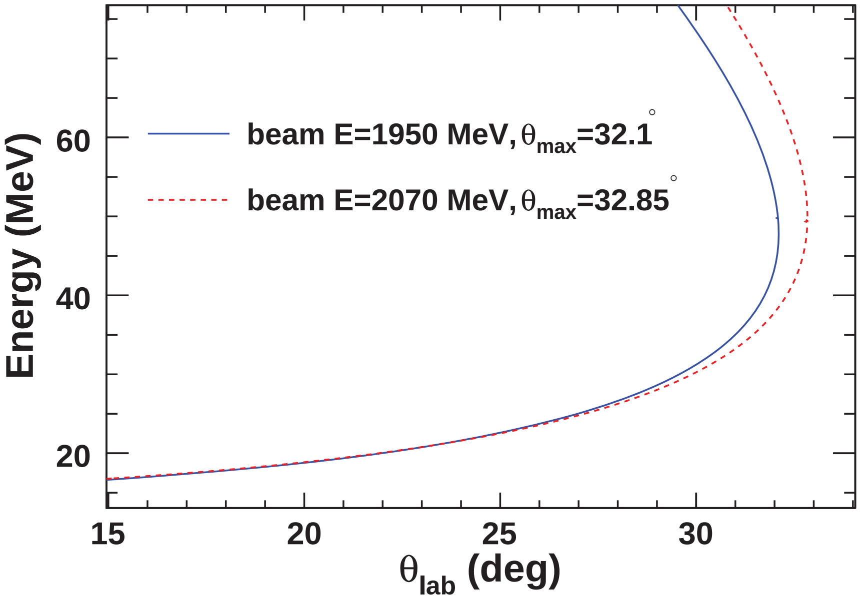

Figure 5.2: Calculated kinematics of the ^{56}Ni(p,d)^{55}Ni for reactions happening at the entrance of the target (dashed red line) and at the exit of the target (solid blue line).

beam particles is less significant, 0.15° FWHM. If the reaction takes place near the exit of the target, the angular straggling will be considerably less, and average angular straggling should be lower than these maximum values. Together with the beam energy difference, the angular straggling of the deuterons dominates the apparent width of the kinematic band at maximum angles.

5.1.2 Improvement in the Angular Resolution with MCPs

We observed three low lying final states in ^{55}Ni with significant cross sections. These are the $7/2^-$ ground state, and two excited states at E*= 2.089 and 3.185 MeV. To determine the effects of the position and angular measurements of the MCPs on the resolution of these states, we performed simulations of kinematics with and without taking into account the MCP measurements. Fig. 5.3 demonstrates two kinematics plots of the p(^{56}Ni,d)^{55}Ni reaction, in which the laboratory energies for these states are plotted as a function of the laboratory scattering angle. In both simulations, the effects of the target thickness on the kinematics are taken into account.

Figure 5.3a shows the results of the kinematics simulations without taking into account the MCP position and angular resolutions. The beam spot size of 11 mm FWHM in the horizontal direction and 17 mm FWHM in the vertical direction, and angular spreads of 1.35° in horizontal direction and 1.5° in vertical direction were used. The beam spot size and beam spread were discussed in Subsection 4.4.5. The kinematic bands corresponding to the three states are broadened with the angular resolution of 2.5°. Beyond 25°, the states begin to overlap and by 30°, it becomes very difficult to distinguish the states experimentally.

Fig. 5.3b shows the simulated kinematics assuming the calculated FWHM angular resolutions and target position resolutions of 0.23° and 1.5 mm, as discussed in Subsection 4.4.4; Improvements in angular resolution allow clearer identification of states in the ^{55}Ni residue. The kinematic bands corresponding to the three states are improved with the angular resolution of 1.0°. In figures 5.3a and 5.3b, the energy resolutions of the Si and CsI detectors have not been taken into account. If we take those into account, the resolution of the bands will be somewhat worse at forward angles of $\theta < 20°$, but essentially unchanged at larger angles.

We would like to point out that the calculated resolution in Fig. 5.3b and the measured resolution in Fig. 5.5b are not limited to the resolution of the MCPs alone. We expected a better angular resolution of 0.5° from the folding of MCP angular, position and HiRA angular resolutions. However, the dominant contribution to the resolution at large angles in the experiment was from the target thickness of 9.6 mg/cm^2. With such a thick target, the maximum angle of deuterons changes with the beam energy at the time of the reaction, which varies depending on the point of interaction in the target. As discussed in Subsection 5.1.1, this effect is approximately 0.8° at 32°. To see what the kinematics would look like without the target thickness effects, we performed a kinematics simulation assuming zero target thickness. The results of this simulation are shown in Figure 5.4. Thus, if one is to use a thin target one should achieve a resolution of 0.5° comparable to that shown in Fig. 5.4 which is clearly better than that shown in Figs. 5.3a and 5.3b.

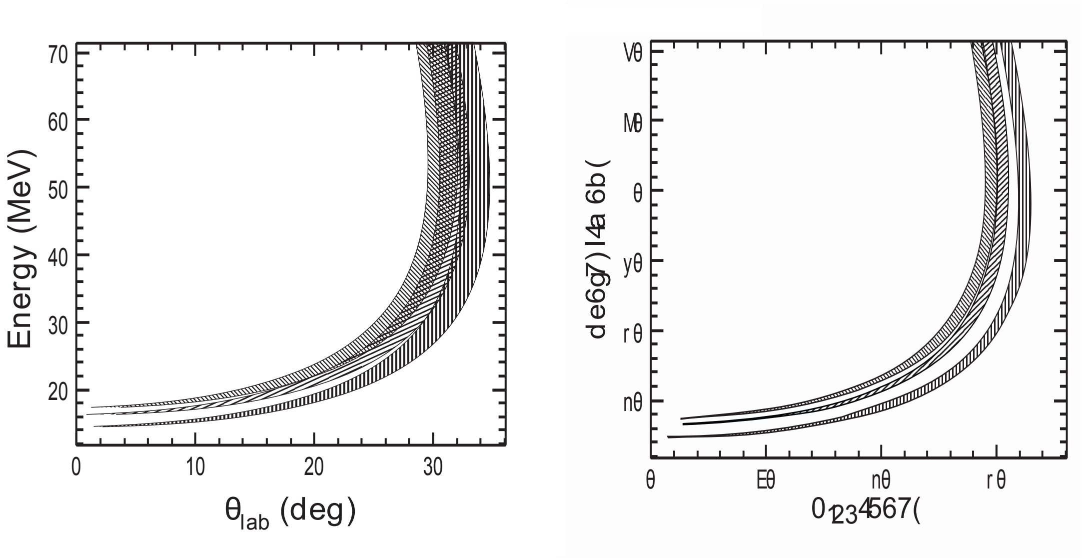

(a) Calculated kinematics without MCPs (b) Calculated kinematics with MCPs

Figure 5.3: Comparison between calculated deuteron kinematics plots with and without using the MCPs. There's a clear improvement in separation of the ground state (the lowest band) from excited states. At higher angles, it is necessary to use the MCPs to get a separation of excited states. These calculations only illustrate the improvement of the angular resolution coming from the use of the MCP tracking detectors. These figures do not include the influence of finite energy resolution in the silicon and CsI detectors of HiRA.

Fig. 5.5 demonstrates the improvement of the experimental resolution in a plot of measured deuteron energy vs. measured laboratory angle. At larger angles the ground state can be clearly separated from the excited states with MCP angles, but without them it is not possible to resolve the ground state.

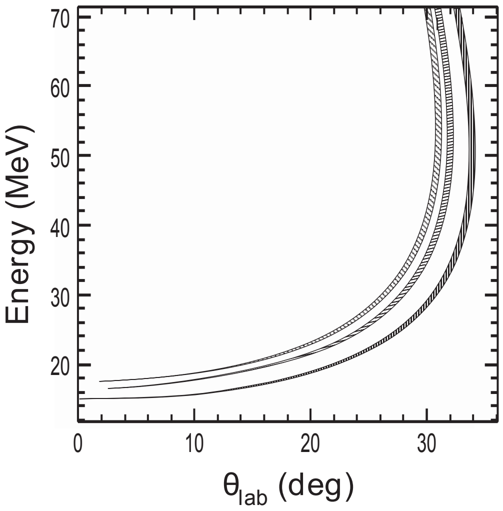

Figure 5.4: Calculated deuteron kinematics for the ^{56}Ni(p,d)^{55}Ni reaction assuming zero target thickness.

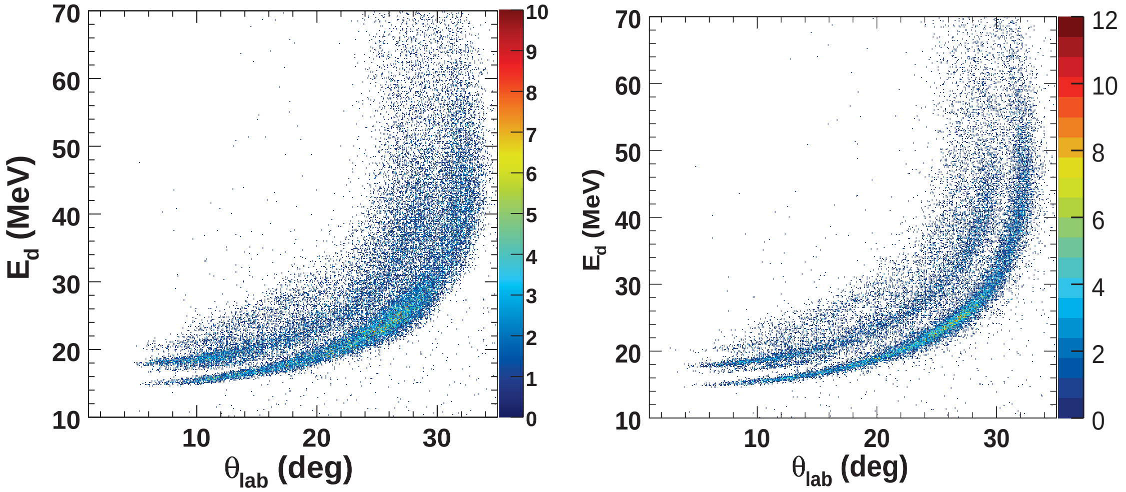

(a) Kinematics without MCPs

(b) Kinematics with MCPs

Figure 5.5: Comparison between deuteron kinematics plots with and without using the MCPs. There's a clear improvement in separation of the ground state (the lowest band) from excited states.

5.2 Q-value Calculations

Let us look at the kinematics of a transfer reaction, with the beam particle A and target a, and reaction products B and b. In our case, A is ^{56}Ni, a is a proton, B is ^{55}Ni and b is a deuteron. We adopt the notation

$$A + a \rightarrow B + b \tag{5.1}$$

for the reaction where the ^{56}Ni (A) and the proton target (a) lead to the production of a ^{55}Ni residue (B) and a deuteron (b). Figure 5.6 exhibits the parameters pertaining to the reaction in Equation 5.1. The emitting angles of the nuclei B and b in the laboratory system are ϕ and θ, respectively.

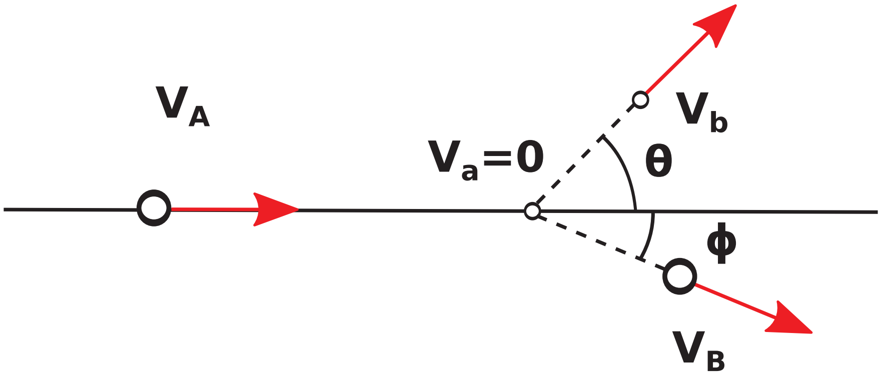

Figure 5.6: Nuclear reaction $A + a \rightarrow B + b$, as seen in the laboratory frame of reference.

In the laboratory frame of reference, the conservation of energy dictates the following relationship between the kinetic energies of particles before and after the reaction:

$$T_A + Q = T_B + T_b \tag{5.2}$$

where the *Q-value of the reaction* denotes the increase in kinetic energy for the reaction, and T_A, T_B and T_b are the kinetic energies of the projectile and reaction products, respectively.

The kinetic energy of the target a is conveniently omitted ($T_a = 0$) because it is at rest in the laboratory system. The Q-value is given by the difference between the rest energies in the entrance and exit channels:

$$Q = (m_A + m_a - m_b - m_B^*) \tag{5.3}$$

In this expression, we use the unit system where $c = 1$. We have put a star on m_B because the nucleus B (^{55}Ni) can be in an excited state, which increases its rest energy by an amount equal to the excitation energy. It should be noted that our light product b, the deuteron, has no particle stable excited states. It is particle bound only in its ground state.

To calculate the excitation energy of the state or equivalently m_B^* in Equation 5.3 from an observed kinematic line in the experiment, conservation of energy and momentum, or the 4-momentum, is used.

The following equation for conservation of 4-momentum,

$$P_A + P_a = P_B + P_b \tag{5.4}$$

where $P_A = (E_A, \vec{P}_A)$, can be rewritten as

$$P_A - P_b = P_B - P_a \tag{5.5}$$

By taking the Minkowski norms ($P^2 = \vec{P}^2 - E^2$) of both sides of Equation 5.5, and using the *relativistic energy-momentum relation* $E^2 = \vec{P}^2 + m^2$, we obtain the following relationship,

$$
{m_A}^2 + {m_b}^2 - 2E_A E_b + 2|\vec{P_A}||\vec{P_b}|cos(\theta) = {m^*_B}^2 + {m_a}^2 - 2E_B m_a \tag{5.6}
$$

where θ is the angle between the heavy ^{56}Ni and deuteron. In the calculation of this angle, beam angle and position are taken into account in addition to HiRA angles. Replacing E_B by $(E_A + m_a - E_b)$ on the right hand side of the Equation 5.6, due the conservation of energy, and leaving m^*_B alone, we reach

$$
\begin{aligned}
m^*_B &= m_B + E^*_B \\
&= \sqrt{{m_A}^2 + {m_b}^2 - {m_a}^2 - 2E_A E_b + 2|P_A||P_b|cos(\theta) + 2(E_A + m_a - E_b)m_a}
\end{aligned} \tag{5.7}
$$

After m^*_B is determined from Equation 5.7, it is inserted into Equation 5.3, and the reaction Q-value is calculated on an event-by-event basis.

Fig. 5.7 shows a quantitative improvement of Q-value peaks when using the MCPs. Four Q-value spectra were obtained on an event by event basis for center of mass angle up to 60° in steps of 15°. The resolution depends on the angle, so the Q-value resolution changes depending on the selection of angles, getting worse at larger center of mass angles. It can be seen from the plots that the improvement with MCPs is more prominent at larger angles, in the 45°-60° angular range, the improvement in Q-value resolution is from 3.0 MeV to 1.5 MeV, while in the 0°-15° the improvement is from 0.6 MeV to 0.5 MeV. The remaining widths of the states is largely due to the target thickness as discussed in the previous section (5.1.2).

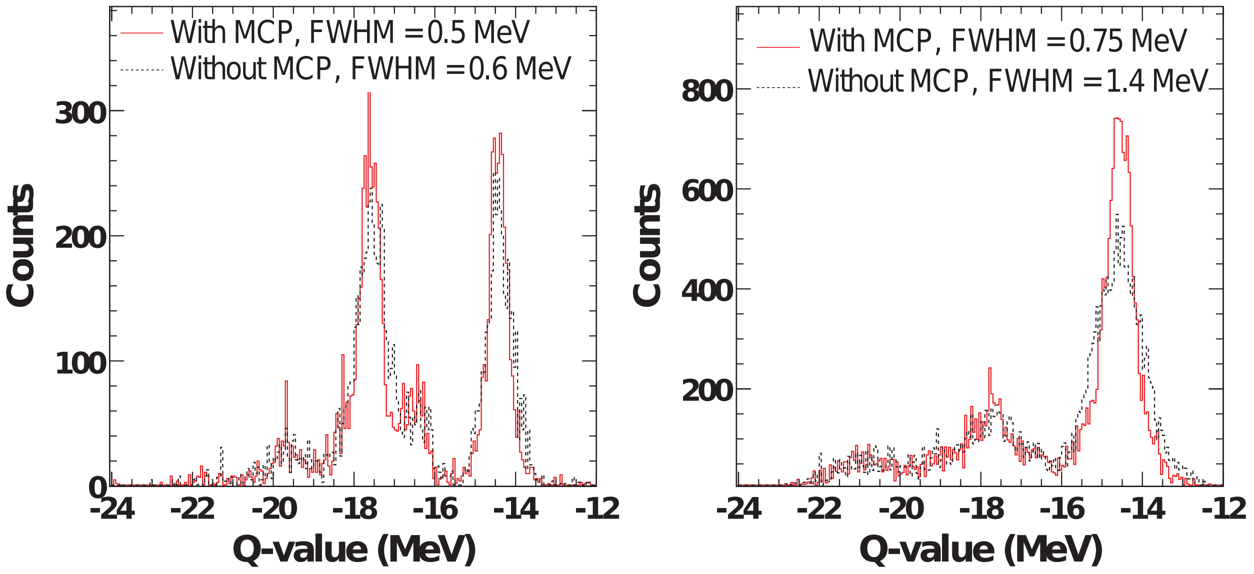

(a) θ_{cm}=0°-15°

(b) θ_{cm}=15°-30°

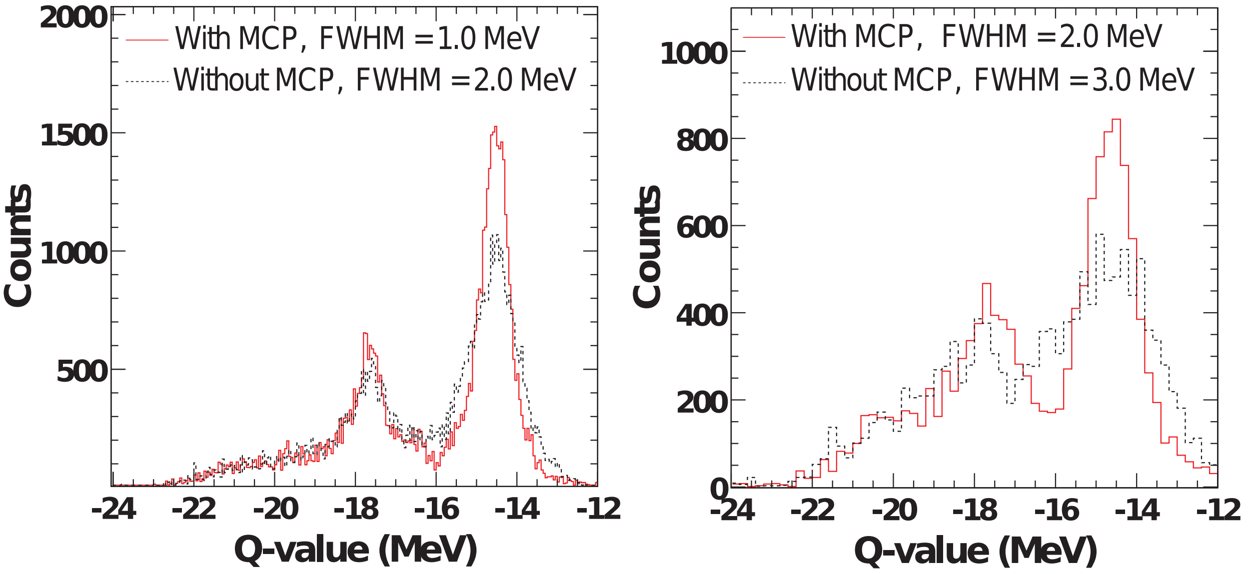

(c) θ_{cm}=30°-45°

(d) θ_{cm}=45°-60°

Figure 5.7: Q-Value spectra with the MCPs and without the MCPs in four angular ranges.

5.3 Background Subtraction

Since our measurement is kinematically complete, meaning we have complete information about the motion of reaction participants both before and after the reaction, it is necessary to make sure that we identify and eliminate any background due to particles that are not involved in the reaction. In principle, the main source of such background events are the carbon nuclei in the CH_2 target, which comprise 1/3 of the total number of nuclei in the target. The main trigger for data runs in the experiment was the coincidence of HiRA and the S800, so an event is registered only if there are signals from both HiRA and S800. By selecting the deuterons in HiRA and ^{55}Ni in S800, we select events that correspond to the ^{56}Ni(p,d)^{55}Ni reaction, while neglecting events corresponding to many of the reactions on the ^{12}C in the target. However, it is possible that both deuterons and ^{55}Ni particles may originate in a reaction involving the carbon in the target.

To estimate the contribution from the carbon nuclei to our reaction yields, we performed a calibration run with a target made of pure carbon. For a correct estimate of the background counts in the actual data runs, it is neccessary to normalize the carbon data, as the number of carbon particles in the target and the total number of beam particles are different between the carbon target runs and normal data runs. This carbon target was 17 mg/cm^2 thick, corresponding to 8.52×10^{20} carbon nuclei per cm^2, while the 100 μm thick plastic target had 3.95×10^{20} carbon nuclei per cm^2. The total number of beam particles hitting the carbon target was 7.0×10^8 versus 2.1×10^{10} in the data runs with the plastic target. This corresponds to a normalization factor of 13.9; i.e. we must multiply the carbon background run by about 14 to get the appropriate estimate of background for the reaction with the CH_2 target.

Figure 5.8 shows the S800 particle identification plot of data with the carbon target in place on the right panel and the deuteron kinematics for these data. It demonstrates that there is negligible background from the carbon nuclei, with only about 10 particles scattered through the ranges of the kinematics plot. Two kinematics cuts are displayed, the cut with black solid line corresponding to ground state, and the cut with black dashed line corresponding to the states near 3.185 MeV. Inside each of the cuts, only one count is found, which is statistically not significant compared to the counts from the ^{56}Ni(p,d)^{55}Ni reaction. Thus, we have not performed background subtraction for the reaction on ^{12}C in the analysis described below.

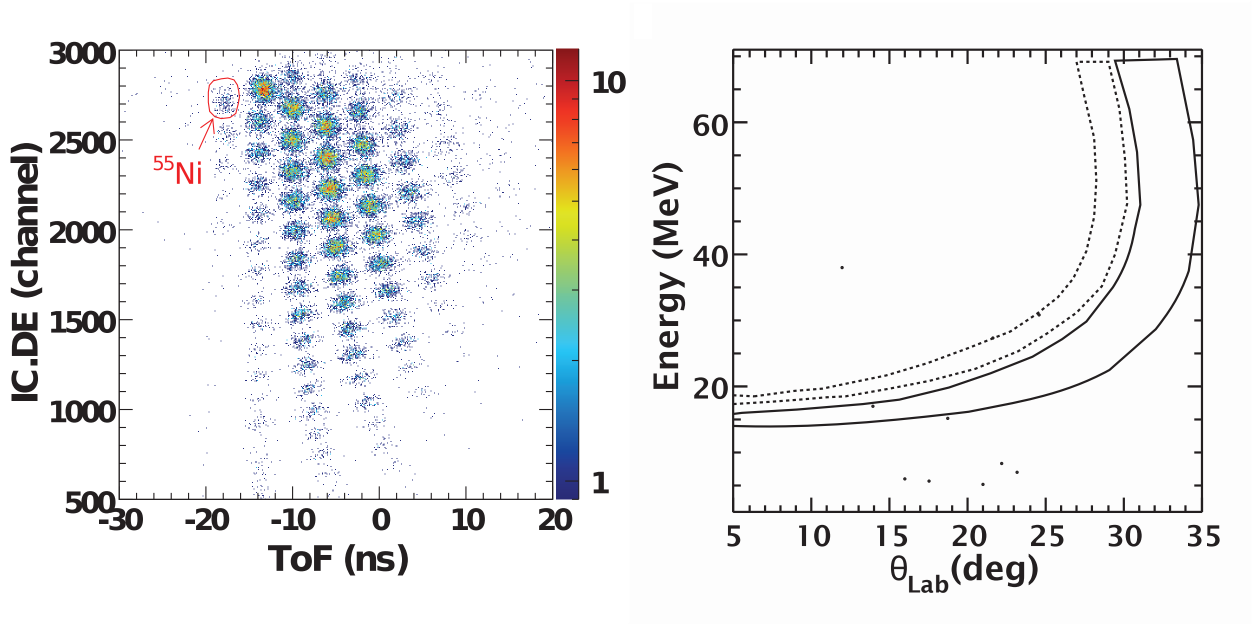

(a) (b)

Figure 5.8: Carbon target reaction runs with ^{56}Ni beam. (a) S800 PID spectrum gated on the incoming ^{56}Ni beam. (b) Deuteron kinematics spectrum gated on ^{56}Ni beam particles and ^{55}Ni residues. Two kinematics cuts are displayed, the cut with black solid line corresponding to ground state, and the cut with black dashed line corresponding to the states near 3.185 MeV.

5.4 Extraction of Cross Sections

In extracting absolute differential cross sections, we must normalize the yields of the angular distribution using the total number of beam particles and areal density of target particles. In this section, we describe how we calculated the normalization coefficient and differential cross sections, as well as how we estimated the uncertainties from efficiencies of various detectors used in the measurement. Thus, we show that the experimental cross section does not vary throughout the experiment. Lastly, we compare the differential cross sections obtained to reaction model calculations, and discuss the extraction of spectroscopic factors.

5.4.1 Absolute Normalization and Error Analysis

Due to the complexity of the experiment, normalization of the differential cross section has many components. The absolute differential cross section as a function of angle could be expressed by the following equation:

$$(\frac{d\sigma}{d\Omega})^{CM}_{\theta_i} = \frac{N_d(\theta_i)}{\Delta\Omega(\theta_i)N_{tar}N_{beam}} \tag{5.8}$$

where N_{beam} is the total number of ^{56}Ni beam particles that hit the target for over a specific time interval Δt; N_{tar} is the number of hydrogen nuclei per square centimeter in the reaction target; N_d is the actual number of deuterons from the reaction of interest emitted during the time interval Δt in the i^{th} scattering angle bin in the center-of-mass frame; $\Delta\Omega(\theta_i)$ is the center-of-mass solid angle corresponding to this angular bin.

$N_d(\theta_i)$ differs from the measured value by several factors. One is the data acquisition efficiency ϵ_{daq}, also known as the *live time* fraction, which accounts for the loss of events that occur when the data acquisition is busy reading a previous event. Taking these factors into account, the actual number of deuterons, N_d, can be determined from the measured coincidence between deuterons and ^{55}Ni recoils, the live time of data acquisition (ϵ_{daq}), the A1900 XFP efficiency (ϵ_{xfp}), the MCP position efficiency (ϵ_{mcpPos}), the S800 acceptance and transmission efficiency (ϵ_{s800}), and the HiRA geometric efficiency ($\epsilon(\theta_i)_{HiRA}$) using Equation 5.9. These efficiencies influence the measured number of events because the XFP, MCP and S800 are needed to identify the transfer reaction events. As the MCP efficiency depends on the beam particle, the efficiency for the ^{56}Ni beam was determined and used. We use the efficiency for measuring all four anode signals (position signal) in the MCP, as explained below. It is observed that if there is a position signal in an MCP, then there is always a time signal. Taking these factors into account,

$$N_d(\theta_i) = \Sigma_{run}\left(\frac{N_d^{det}(\theta_i)/\epsilon(\theta_i)_{HiRA}}{\epsilon_{daq}\epsilon_{xfp}\epsilon_{mcpPos}\epsilon_{S800}}\right)_{run} \quad . \tag{5.9}$$

As seen in Equation 5.9, the absolute normalization of the cross sections requires direct continuous measurement of beam intensities N_{beam} which was achieved by the MCP1 detector placed 10 cm in front of the reaction target. Since the number of beam particle was determined from MCP, the efficiency of the MCP time signal is required in order to obtain the actual beam particles on target. However, we note that the MCP1 efficiency is required to get $N_d(\theta_i)$. So, to some extent the dependence of the experimental cross section to the efficiency of the MCP1 time signal cancels out. The total number of ^{56}Ni beam particles, N$_{beam}$, is determined from total number of beam particles measured in MCP scaler $N_{beamAll}$, MCP scaler efficiency ϵ_{mcp} and the fraction of ^{56}Ni particles in the beam η.

$$N_{beam} = \eta \frac{N_{beamAll}}{\epsilon_{mcp}} \tag{5.10}$$

The scaler efficiency is governed by the efficiency for the MCP time signal and the dead time of the scaler event. The main factor in the efficiency is the MCP time signal.

5.4.2 Beam Purity

As discussed in Section 4.3.1, we had a cocktail of beams that included isotopes other than ^{56}Ni, thus, we need to accurately determine the fraction of the beam with ^{56}Ni isotopes. Other major isotopes in the beam cocktail are ^{55}Co and ^{54}Fe, as shown in Figure 4.13. The fractions of the main beam contaminants, ^{55}Co and ^{54}Fe, are 24% and 4%, respectively. These beams had similar magnetic rigidities to ^{56}Ni, thus making it through the A1900 separator to the reaction chamber. On the proton rich side of the valley of stability, nuclei with the same number of neutrons constitute the dominant contribution to the beam. To separate these isotopes, we used the difference in velocities of these isotopes by measuring the time of flight from the A1900 fragment separator to the reaction target. As shown in Figure 5.9, the fraction of the ^{56}Ni particles in the beam fluctuates slightly between 0.69 and 0.72, with an average purity of 0.71.

5.4.3 Charge States

The net charge of an ion is called its *charge state*. Because of electromagnetic interactions with atoms, some ^{55}Ni residues pick up electrons in the target, changing the charge state of the ion. These ions with different charge states will have a different magnetic rigidity

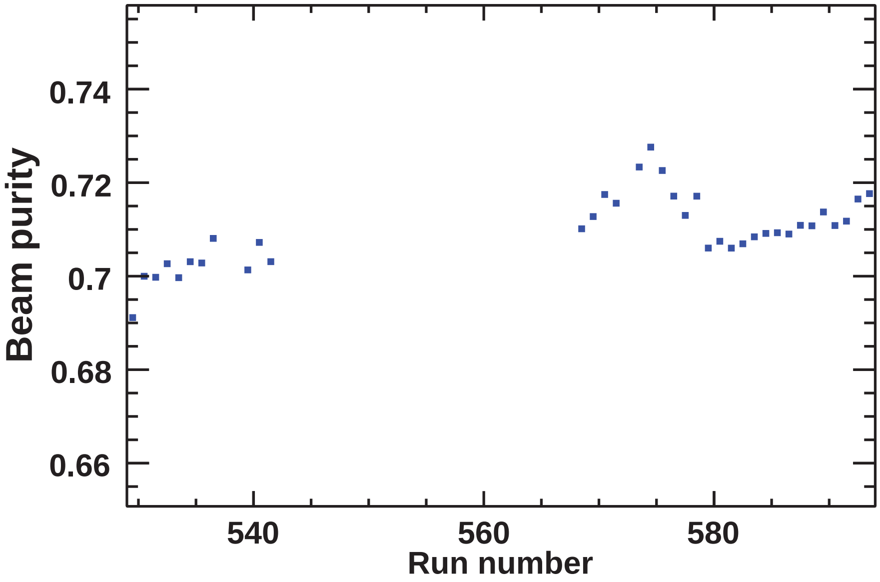

Figure 5.9: The fraction of the ^{56}Ni particles in the beam run-by-run. The runs 543-567 do't have the fractions because they were test and calibration runs.

due to a changed charge state. Generally, the lower charge state ion will be deflected less than the fully stripped ion and will not reach the focal plane of the S800 spectrometer. To account for the loss of particles to charge state changes, we needed to determine the fraction of isotopes with charge state +28 after they enter the reaction target to within 1% error. To do this, we had a "charge state run", where the magnetic rigidities of the S800 magnets were set so that both +28 and +27 charge states could reach the focal plane. We did this using the beam because the charge state change cross sections are the same for ^{55}Ni and ^{56}Ni since they are almost identical chemically. The distribution of charge states is demonstrated in Figure 5.10, in which the time of flight from the A1900 XFP to the S800 focal plane is plotted versus the CRDC1 x position. As the beam is not pure, two groups of peaks instead of only two peaks can be identified in the figure, with normal charge states on the right and lower charge states on the left. The two peaks with the lowest values of the TOF are ^{56}Ni, the next two at higher TOF are two charge states of ^{55}Co. The group on the left is shifted up by about 11 ns because of the corrections applied on the time of flight based on the focal plane positions. The total number of ^{56}Ni particles is 59124, and 54460 of them, or 92.1%, are in 28$^+$ charge state.

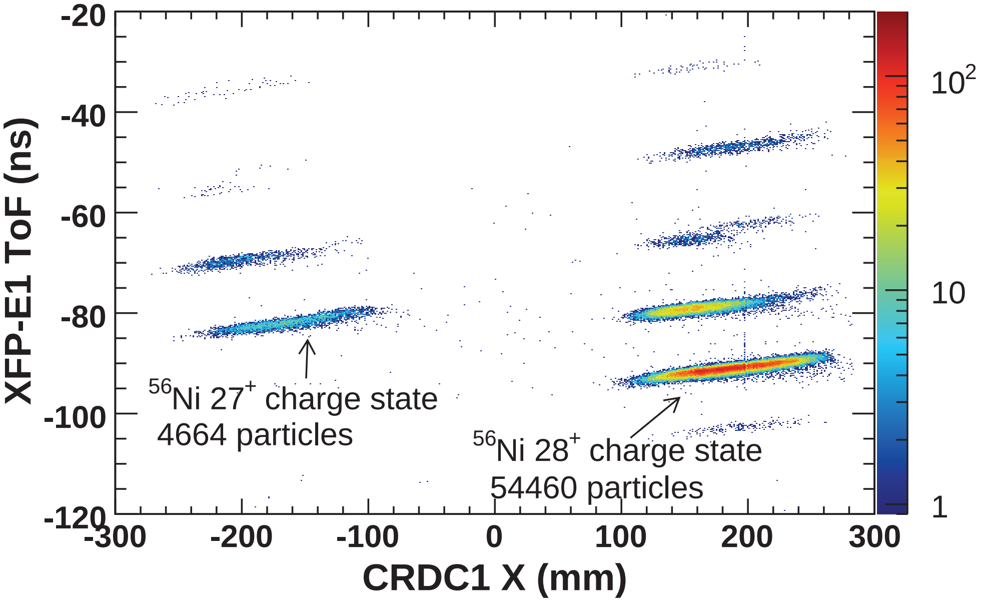

Figure 5.10: A plot of the charge state runs. The +27 and +28 charge states of ^{56}Ni are indicated.

5.4.4 Detection Efficiencies

In order to perform a correct normalization, detection efficiencies and the live time of the DAQ have to be accurately estimated. The efficiencies of detectors such as MCPs, HiRA, S800 and A900 XFPs are discussed in this subsection.

5.4.4.1 Live Time of Data Acquisition

The live time of the data acquisition is the period when the data acquisition system is not busy and can accept the arriving events. The counting rates of events as a function of time were recorded by electronic scaler modules. Typically the same signal was put into two scalers. One of them was run without a gate. It therefore recorded the total signal rate. The second scaler had a gate applied to it. This gate was the live time, which enabled the scaler to record pulses only when the data acquisition was live. By comparing the live to raw (total) rates of recorded scaler signals, the DAQ live time can be calculated. Figure 5.11 shows the ratios of the live to raw rates for the signals from the MCP0 and MCP1 discriminators and from the clock in the present experiment. One notices that the live time was low, about 0.5, for runs 529 through 541. This is because the HiRA singles signals were included in the trigger as a secondary trigger for these runs, increasing the dead time. As the HiRA singles had a rate of approximately five times higher than the coincidence rate of HiRA and S800, the live time was lowered because of higher total trigger rate. The MCP1 live time, which is similar to the MCP0 and the clock live time, was used as DAQ live time in this experiment. In general, the live time from the MCP scalers should be a little more accurate if the beam intensity is showing fluctuation, because the clock can generate signals when the beam intensity is zero and the computer is 100% live. The similarity of MCP and clock deadtimes indicate that the beam was rather constant in intensity.

5.4.4.2 S800 Acceptance and Transmission Efficiency

In order to correctly estimate the number of ^{55}Ni residues originating from the ^{56}Ni(p,d)^{55}Ni reaction, we need to know the fraction of these residues that reach the S800 focal plane. The maximum rate of particles the focal plane detectors can withstand is about 6000 per second,

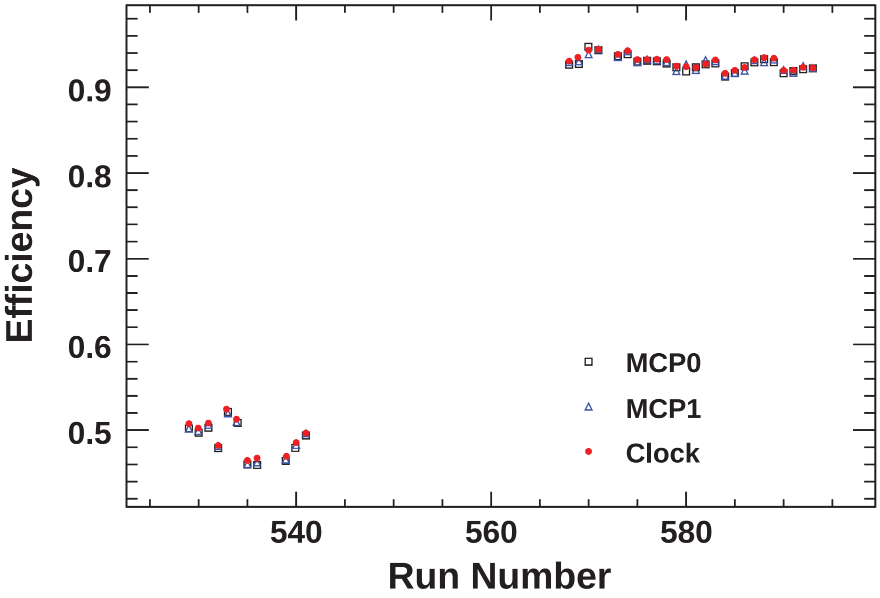

Figure 5.11: Live time of data acquisition, acquired by the ratios of live to raw rate of MCP0, MCP1 and the clock. The runs 543-567 are not included because they were test and calibration runs.

therefore a tungsten beam blocker was inserted on the low rigidity side (below -100 mm in CRDC1) of the S800 magnet to keep the focal plane detectors from being overwhelmed by the intensity of the beam particles.

We checked whether the residues of interest were blocked by the blocker and are within the S800 acceptance by the CRDC positions of the particles of interest with and without selecting the deuterons detected in HiRA. From the discussion of charge states in Subsection 5.4.3 above, we conclude that all the ^{55}Ni with charge states different from 28+ will be blocked by the beam blocker, therefore we are interested in the transmission efficiency for ^{55}Ni reaction residues with 28+ charge state.

Figure 5.12, shows all of the ^{55}Ni, regardless of their origin, in the CRDC2 detector of the S800 focal plane. We can see the discontinuity at x=300 mm of the CRDC2 spectrum, which means that some of the ^{55}Ni are not reaching the S800 focal plane. Assuming a symmetric distribution, we calculate that approximately 5% of the ^{55}Ni are lost. However, we are only interested in the transmission efficiency for the recoil residues from the ^{56}Ni(p,d)^{55}Ni reaction. Figure 5.13, showing the ^{55}Ni recoil residues from the ^{56}Ni(p,d)^{55}Ni reaction in the CRDC2 detector of the S800 focal plane, demonstrates that all the ^{55}Ni nuclei remain within the unblocked region of the S800 focal plane. It is expected that the distribution of the recoil residues is continuous, without abrupt changes. Thus, it can be assumed that the transmission efficiency is essentially 100%, and no correction is necessary for the estimation of the number of ^{55}Ni residues.

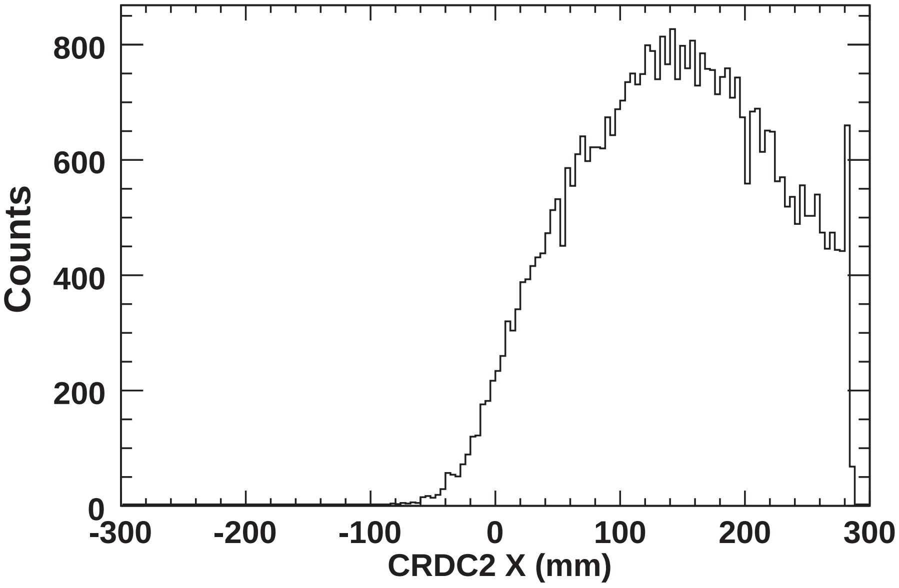

Figure 5.12: The distribution of all the ^{55}Ni residues in the CRDC2 detector of the S800 focal plane.

5.4.4.3 MCP Efficiency

As the MCPs give us both position and time information that are used in the experiment, we need to consider the efficiencies for both on a run-by-run basis. As expected, the signals are

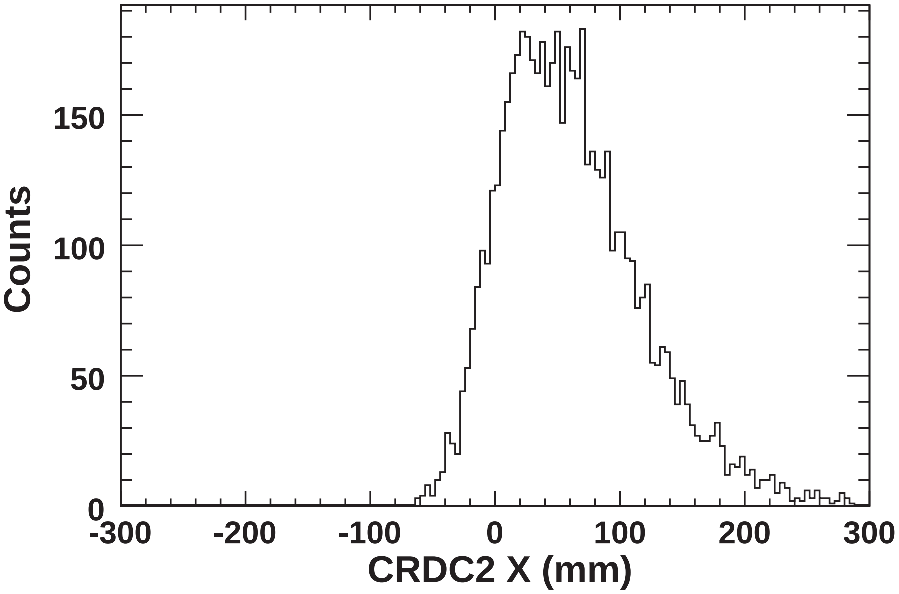

Figure 5.13: The distribution of the ^{55}Ni recoil residues from the ^{56}Ni(p,d)^{55}Ni reaction in the CRDC2 detector of the S800 focal plane.

correlated, and MCP time signal has the efficiency of 1 when the MCP position is measured, meaning whenever there is a position signal from an MCP, there is always a time signal from it as well. The MCP time efficiency is obtained by taking the ratio of the number of registered MCP time events gated on S800 E1 signal to the number of events with non-zero E1 signal. The downstream MCP (MCP1) time signal is used for estimating the total number of beam particles hitting the target. However, since we used the MCP1 time signal for selecting the ^{55}Ni reactions residues in the S800 focal plane, this efficiency shouldn't affect the extraction of the differential cross section, as the number of reaction events are divided by the number of beam particles. Still, the MCP position efficiencies for events that have an MCP1 time, which is the efficiencies of both MCP positions when there is a time signal from MCP1, must be known to determine the cross section for the ^{56}Ni(p,d)^{55}Ni reaction events that populate particular states of the ^{55}Ni nucleus. This simplifies the correction for the MCP efficiency.

Figure 5.14 shows the run-by-run time efficiency of MCP1. There is a gap in run numbers from run 541 to run 568, as we had some calibration runs between those runs. As one can see, the efficiency deteriorates over time, but stays above 0.90 for the duration of the experiment, with an average 0f 0.94. Figure 5.15 shows the run-by-run efficiency of combined MCP0 and MCP1 positions. The efficiency fluctuates between 0.75 and 0.65 for the duration of the experiment, with an average of 0.70.

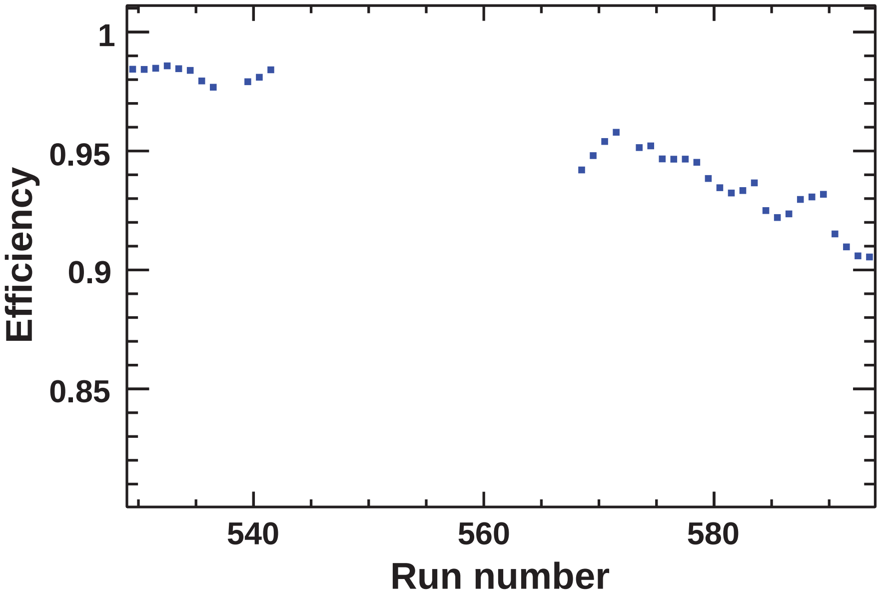

Figure 5.14: Run-by-run efficiency of MCP1 time. The runs 543-567 are not included because they were test and calibration runs.

5.4.5 HiRA Geometric Efficiency

In Subsection 3.2.4, we discussed the geometric efficiency of the designed HiRA setup, however, the real geometric efficiency is slightly different. A minor change resulted from the difference between actual positions of pixels obtained from LBAS measurement, as discussed in Section 3.7, and the design values. A larger difference resulted from the fact that not all

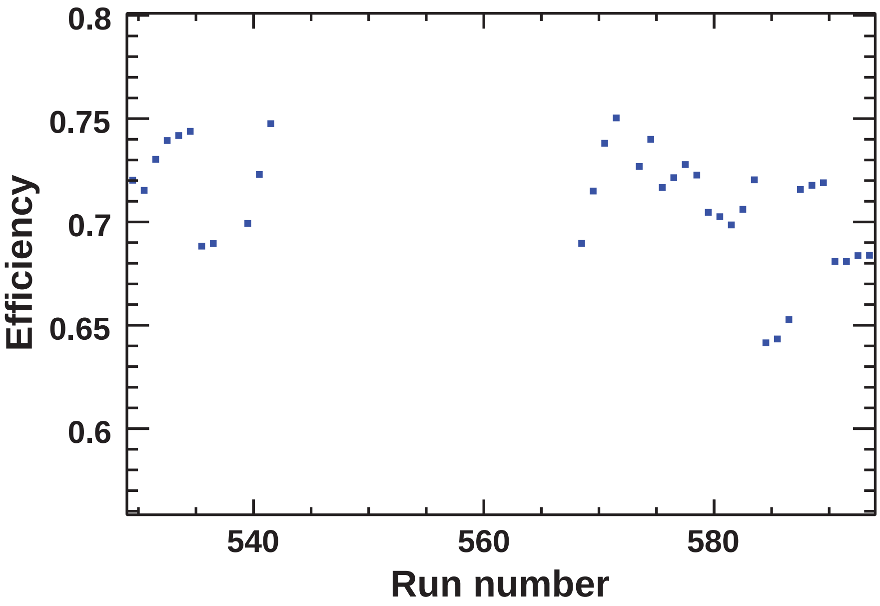

Figure 5.15: Run-by-run efficiency of combined MCP0 and MCP1 positions. The runs 543-567 are not included because they were test and calibration runs.

of the Si strips and CsI(Tl) crystals were functioning. A total of 38 silicon strips, including 17 DE, 13 EF and 8 EB strips, and one CsI crystal in telescope 15 did not work. Also, due to the gaps between the CsI, particles punching through strips 15 and 16 would not always be accurately identified, and therefore these particles were not included in the data analysis.

5.4.5.1 Effects of Beam Angle and Position at Target on Geometric Efficiency

The ^{56}Ni beam that was used in the experiment had a wide phase-space spread due to the selected compromise between intensity and beam quality. A smaller phase space could have been achieved, but at the cost of reduced beam intensity. At the target, the beam had an angular spread of 15 mrad in the horizontal direction and 20 mrad spread in the vertical direction, as well as a spot size of 15 mm in the horizontal direction and 20 mm in the vertical direction. This spread smears the geometric efficiency over the actual scattering angles. A Monte-Carlo simulation of these effects was performed, which demonstrated the smearing of the sharp edges for geometric efficiency in Figure 5.16. The red histogram shows the geometric efficiency calculated without taking into account the beam smearing, and the blue histogram shows geometric efficiency calculated taking into account the beam smearing, as monitored by the MCPs. Figure 5.16, showing the ratio of the calculated efficiencies with and without the beam smearing, emphasizes the differences between these two histograms. Below 5 and above 41 degrees, there is a significant difference between the two efficiencies, at least a factor of 2.5. Where the ratios differ by more than 30%, one must be cautious in using the efficiency because it strongly relies on the understanding of the resolution function for the MCPs. Between those values, the efficiencies are consistent with other, with a maximum deviation of 30% in the range of 5-5.5 degrees, and approximately 20% at the edges of telescopes.

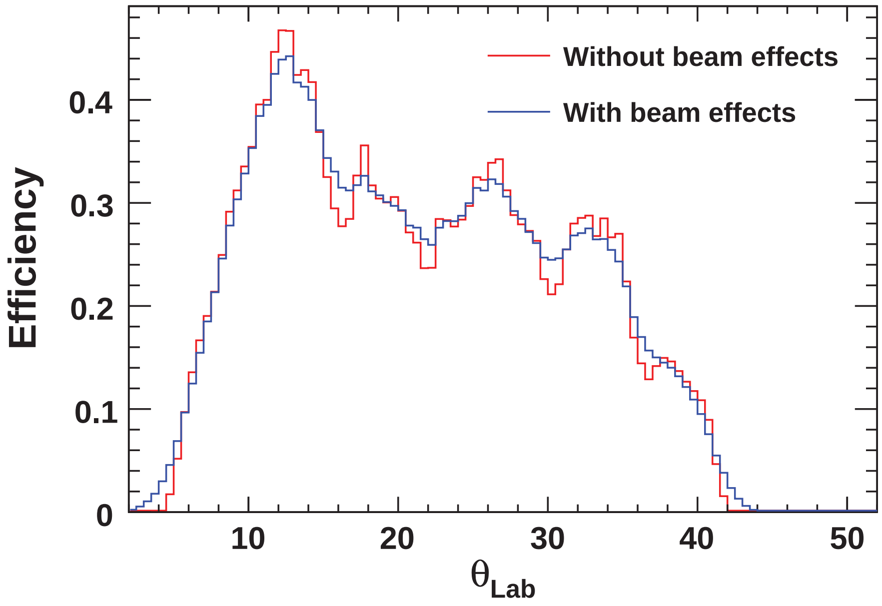

Figure 5.16: Comparison of geometric efficiencies of the HiRA configuration with and without the beam effects.

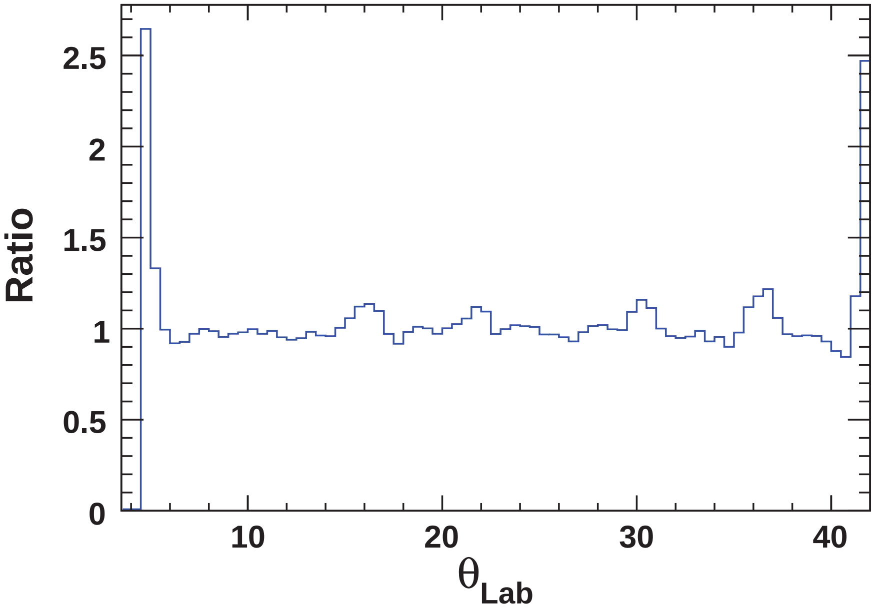

Figure 5.17: Ratio of geometric efficiencies of the HiRA configuration with and without the beam effects.

5.4.6 Overall normalization uncertainties

The data set was split into seven groups of runs in order to estimate the overall normalization uncertainties stemming from detection efficiencies and other systematics uncertainties. The normalization uncertainty can be estimated from the variation of the cross section between the groups. The ground state spectroscopic factors for each group are shown in Figure 5.18. Fluctuations between different groups are found, but the overall normalization uncertainties are usually better than ±8% indicated by the corresponding dashed lines.

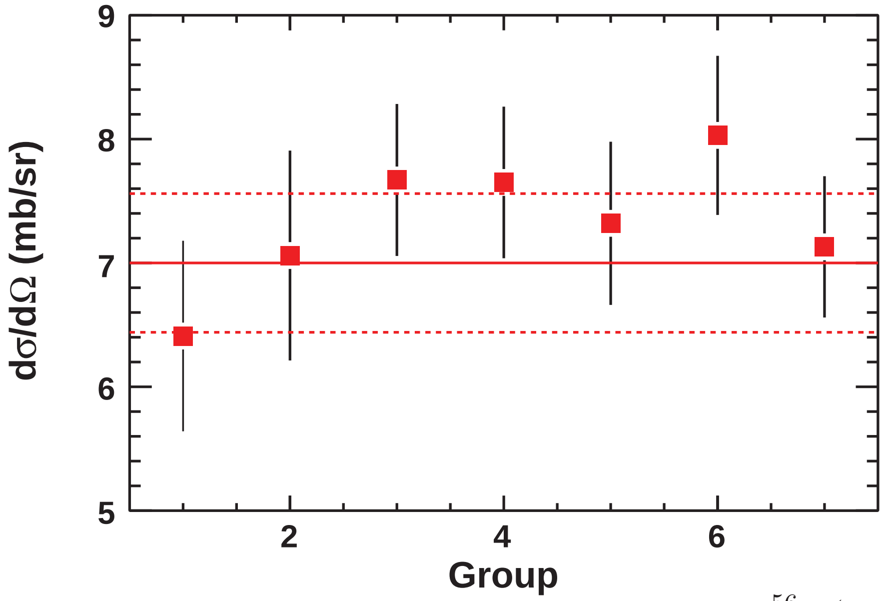

Figure 5.18: The ground state spectroscopic factors for the ^{56}Ni(p,d)^{55}Ni reaction for seven groups of the data set.

5.5 Differential Cross Sections and Spectroscopic Factors

Differential cross sections for the ^{56}Ni(p,d)^{55}Ni reaction populating ground and some excited states of the ^{55}Ni nucleus are the main observables of this experiment. They are obtained after correctly determining and normalizing the angular distributions of the deuterons in the center-of-mass frame. Tables 5.2 and 5.3 list the experimental differential cross sections. As shown in Figure 5.19, the data are also plotted in solid circles with purely statistical uncertainties for the ground state. For the ground state of ^{55}Ni, spectroscopic factor of 7±0.7 is obtained. The error bars for the center-of-mass angles are larger for the backward angles, as it depends not only on the laboratory angular resolution, but also on the energy resolution and the beam energy at the time of the reaction, increasingly so at larger angles. Differential cross sections determined from the present measurements are compared to calculations in the framework of the ADWA using CH89 global optical-model potentials and transferred neutron orbital with Woods-Saxon potential of fixed radius 1.25 fm (discussed in Section 2.2).

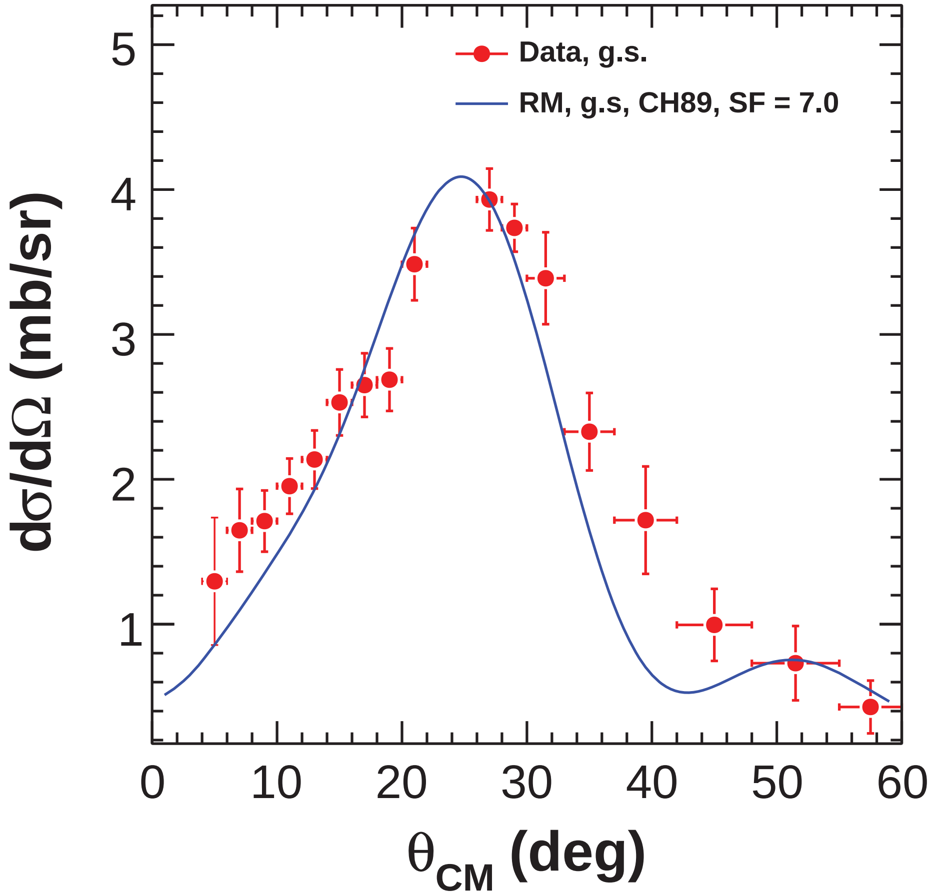

Figure 5.19: Differential cross section of ^{56}Ni(p,d)^{55}Ni reaction resulting in the ground state of ^{55}Ni.

5.5.1 Line Shape Analysis

As shown in Table 5.1, the known excited states of ^{55}Ni below 3.5 MeV are at 2.089, 2.462, 2.839, 2.882, 3.185 and 3.5 MeV. For these states, we did not have the energy resolution to unambiguously resolve them. However, we can deduce the differential cross sections and ℓ

Table 5.2: Table of values for differential cross section of ^{56}Ni(p,d)^{55}Ni reaction resulting in the ground state of ^{55}Ni.

CM angle (deg)	$d\sigma/d\Omega$ (mb/sr)	error (mb/sr)
5	1.3	0.44
7	1.65	0.29
9	1.71	0.21
11	1.95	0.19
13	2.14	0.20
15	2.53	0.23
17	2.65	0.22
19	2.69	0.22
21	3.48	0.25
27	3.93	0.21
29	3.74	0.16
31.5	3.39	0.32
35	2.32	0.27
39.5	1.72	0.37
45	0.99	0.25
51.5	0.73	0.26
57.5	0.43	0.18

values by looking at the shapes of excitation energy spectra for different angular bins, in other words performing *line shape analysis*. Figure 5.20 demonstrates how the line shape analysis is done for 2° angular cuts from 5° to 17°. The vertical lines represent where the known energy states should be, the solid fit line is the overall fit function used to calculate the peaks of the states in the line shape analysis, and the dashed lines show the individual gaussians for the states derived from the fitting. This fit was done with constraints that the peak centers should be at the known energy values and the resolution was fixed at calculated resolutions ranging from 500 keV to 600 keV depending on the angle.

To calculate the differential cross sections from the line shape analysis for each state, we first obtained the number of detected deuterons by integrating the area of the fit curve for that state for each angular cut. Then we calculated the actual number of deuterons by correcting for the geometric efficiency of the HiRA array. After that we applied the normalization procedure discussed in Subsection 5.4.1.

Figure 5.21 shows the differential cross section deduced from the line shape analysis for the 2.089 MeV state. The 2.089 MeV state has unknown spin and parity. For angles larger than 19°, the line shape analysis could not be applied successfully because at these angles the deuterons have high enough energy to enter CsI detectors, which have worse resolutions. Other reasons for the deterioration of the Q-value resolution at large angles are the stronger dependence of the Q-Value resolution on the angular resolution and the reaction point in the target at higher angles. From the Q-value plots in Figure 5.20 one can see that the group of states around 3 MeV is dominated by a strong peak that looks like a single peak at 3.815 MeV. The deduced differential cross sections for the states 2.462, 2.839, 2.882 and 3.5 MeV states do not show significant angular dependence and are small. Therefore we also calculated the cross sections assuming there is a single state around 3 MeV. Figure 5.22

shows the differential cross sections deduced from the line shape analysis and with the single state assumption for the 3.185 MeV state, shown in blue open squares and red filled circles, respectively. The tentative literature ℓ value from the work of Mueller et al. [27,28] for 3.185 MeV state is 0. The results from the line shape analysis and single state assumption differ by approximately 10%. For the extraction of spectroscopic factors, we chose to use the line shape analysis cross sections and errors, as it represents only the 3.185 MeV state.

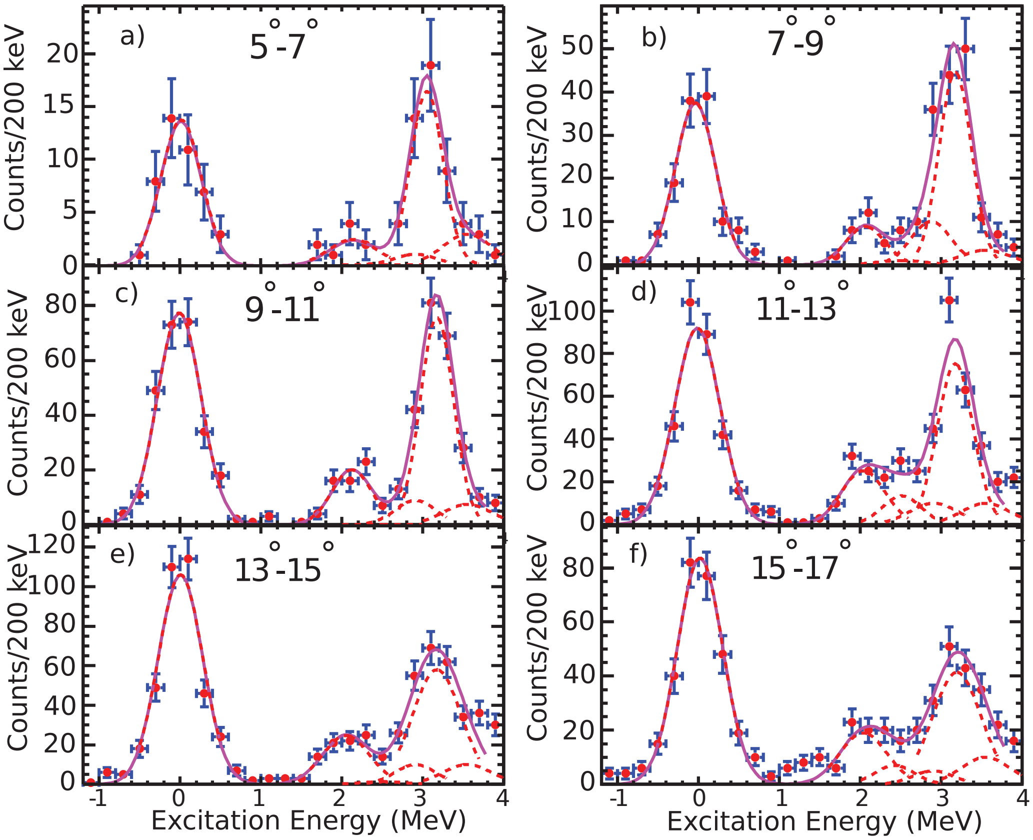

Figure 5.20: Line shape analysis of events in the center-of-mass frame. The solid lines represent the overall fitting function and the dashed lines represent the fitting obtained for individual peaks.

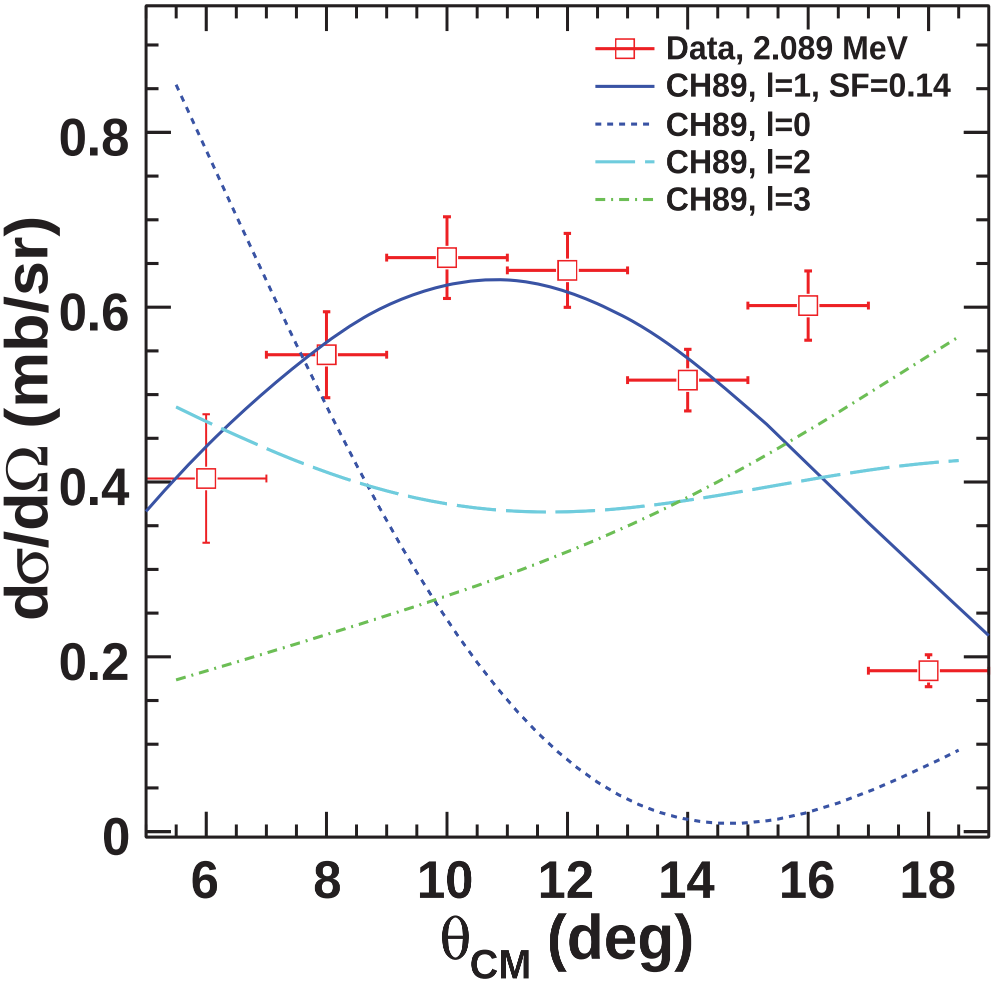

Figure 5.21: Differential cross sections of ^{56}Ni(p,d)^{55}Ni reaction for the ^{55}Ni 2.089 MeV excited state. The blue solid lines are the corresponding reaction model calculations scaled by the corresponding spectroscopic factors. Calculations for different ℓ value transfers with arbitrary scaling factors are given for comparison.

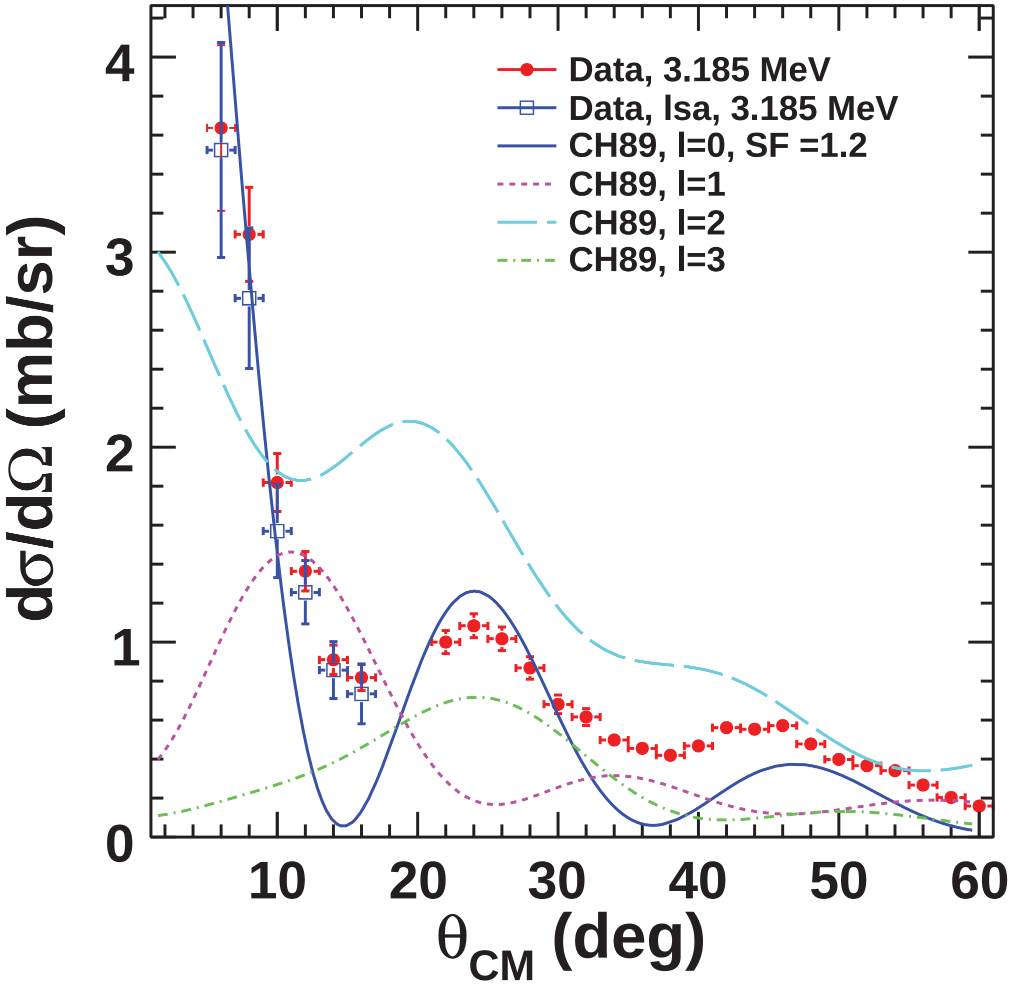

Figure 5.22: Differential cross sections of ^{56}Ni(p,d)^{55}Ni reaction for the ^{55}Ni 3.185 MeV excited state. The blue solid lines are the corresponding reaction model calculations scaled by the corresponding spectroscopic factors. Calculations for different ℓ value transfers with arbitrary scaling factors are given for comparison.

Table 5.3: Table of values for the differential cross section of the ^{56}Ni(p,d)^{55}Ni reaction resulting in the 2.089 MeV excited state of ^{55}Ni.

CM angle (deg)	$d\sigma/d\Omega$ (mb/sr)	error (mb/sr)
6	0.40	0.074
8	0.55	0.049
10	0.66	0.047
12	0.64	0.042
14	0.52	0.035
16	0.6	0.04
18	0.18	0.018

5.5.2 Spectroscopic Factors

Experimental spectroscopic factor for a transfer reaction is obtained by taking the ratio of the measured differential cross sections to those calculated with a reaction model. For the ground state of ^{55}Ni, this was done by using the seven data points near the peak, from 14° to 32° in the center-of-mass frame. The fluctuation of the ground state cross-sections for the groups of runs, discussed in Subsection 5.4.6, is determined to be approximately 10%. Therefore we assign 10% uncertainty to the experimental SFs for the ground state of ^{55}Ni. For the 2.089 MeV state of ^{55}Ni, the spectroscopic factor was extracted by using the four data points near the peak, from 8° to 14° in the center-of-mass frame. Finally, for the 3.185 MeV state of ^{55}Ni, the spectroscopic factor was extracted by using the four data points near the peak at 0°, using the data from 6° to 12° in the center-of-mass frame. The uncertainty for the SFs of these two excited states are estimated to be approximately 20% due to the folding of normalization, fitting and statistical errors. These SFs are summarized in Table 5.5. For uncertainties stemming from the choice of optical model parameters, we assigned the value of 15% based on calculations performed by Nunes et al [96]. Since the reaction model and

Table 5.4: Table of values for the differential cross section of the ^{56}Ni(p,d)^{55}Ni reaction resulting in the 3.185 MeV excited state of ^{55}Ni.

CM angle (deg)	$d\sigma/d\Omega$ (mb/sr)	error (mb/sr)
6	3.3	0.42
8	2.8	0.24
10	1.7	0.15
12	1.2	0.1
14	0.83	0.075
16	0.75	0.066
22	1.0	0.059
24	1.1	0.061
26	1	0.061
28	0.87	0.057
30	0.68	0.048
32	0.62	0.043
34	0.5	0.037
36	0.46	0.034
38	0.42	0.032
40	0.47	0.033
42	0.56	0.037
44	0.55	0.036
46	0.57	0.037
48	0.48	0.033
50	0.4	0.03
52	0.37	0.029
54	0.34	0.028
56	0.27	0.024
58	0.2	0.021
60	0.16	0.018

Table 5.5: Spectroscopic Factors obtained in this work.

Isotope	ℓj^{π}	SF(LB-SM) (theo.)	SF(CH89) (exp.)	Rs (CH89)
^{56}Ni	f7/2$^-$	6.8	7±1.3	1.03±0.18
^{56}Ni	p3/2$^-$	0.18	0.14±0.035	0.78±0.2
^{56}Ni	s1/2$^+$	-	1.2±0.3	-

experimental uncertainties are independent, we have summed them in quadrature. Thus, the total uncertainties for the ground, 2.089 MeV and 3.185 MeV states are 18%, 25% and 25%.

The Large-basis shell-model (LB-SM) calculations for the ground and 2.089 MeV states of ^{55}Ni were performed using the code NuShellX [14] in fppn shell-model space with gx1pn effective interaction [97] by A. Signoracci. The spectroscopic factor of 7±0.7 for the ground state of ^{55}Ni shows a good agreement with shell model calculations and it is consistent with the assumption that ^{56}Ni is a closed shell. The calculations using the GXPF1 interaction in the pf model space performed by M. Horoi [23] give a SF of 6.75, which is very close to the one obtained using the gx1pn interaction above. From a strict theoretical point of view SFs are not occupation numbers but a measure of what fraction of the full wave function can be factorized into a correlated state (often chosen to be a given closed-shell core) and an independent single-particle or single-hole state. Large deviations of these SF from the values predicted by an IPM model indicate a strongly correlated system. The fact that the shell-model calculation and the experimental SF from the present dissertation for the transition to the ground state of ^{55}Ni do not deviate much from the IPM value suggest that the single-particle picture of the ^{56}Ni is a viable assumption.

Another way to obtain experimental SFs is by using knockout reactions. The experimental knockout SFs have been observed to have consistent and significant reductions compared to the theoretical shell-model SFs. For example, Yurkewicz et al. measured one-neutron knockout cross section of ^{57}Ni [20]. They obtained an inclusive cross section of 41.4(12) mb for the reaction, compared to a theoretical prediction of 85.4 mb. Thus, the experimental SF constitutes only 48% of the theoretical cross section. For this reason, it would have been interesting to compare the results of the present dissertation with one-neutron knockout SFs of ^{56}Ni. Currently there is no experimental data published for ^{56}Ni neutron knockout. Recently, however, an experiment was performed to measure the ^{56}Ni neutron-knockout cross sections [98]. This experiment is still being analyzed, and we can compare the results with the results of the present dissertation after its publication.

A second test of these shell-model calculations for ^{56}Ni is that the first excited state has been deduced to have $\ell = 1$ angular momentum. The experimental spectroscopic factor extracted from the data shows a small reduction (R_s=0.78) compared to shell model calculations, but considering the uncertainty of the result, this deviation is not significant.

The results confirm the previously tentative assignment of $\ell = 0$ value to the 3.185 meV state. The Q-value spectrum around 3 MeV region is dominated by transition to the 3.185 MeV, which looks like a single peak with the similar resolution as the ground state. Analysis of the angular distribution of this energy group, shown in Figure 5.22, confirms that the cross section is growing with decreasing angle consistent with an $\ell = 0$ transition because of increasing differential cross section at forward angles. We have looked at other nuclei near ^{55}Ni with the same number of neutrons ($N = 27$) and even number of protons to see if they also have $\ell = 0$ states near 3 MeV. It is interesting to note that the same spectroscopic factor of 1.2 has been observed for the $\ell = 0$ state of ^{53}Fe, which is two protons removed from ^{55}Ni, at 2.96 MeV [99]. Other nuclei with $N = 27$, ^{51}Cr ($Z = 24$), ^{49}Ti ($Z = 22$) and ^{47}Ca ($Z = 20$), have an $\ell = 0$ states at 2.763 MeV [100], 2.504 MeV and 2.600 MeV, respectively.

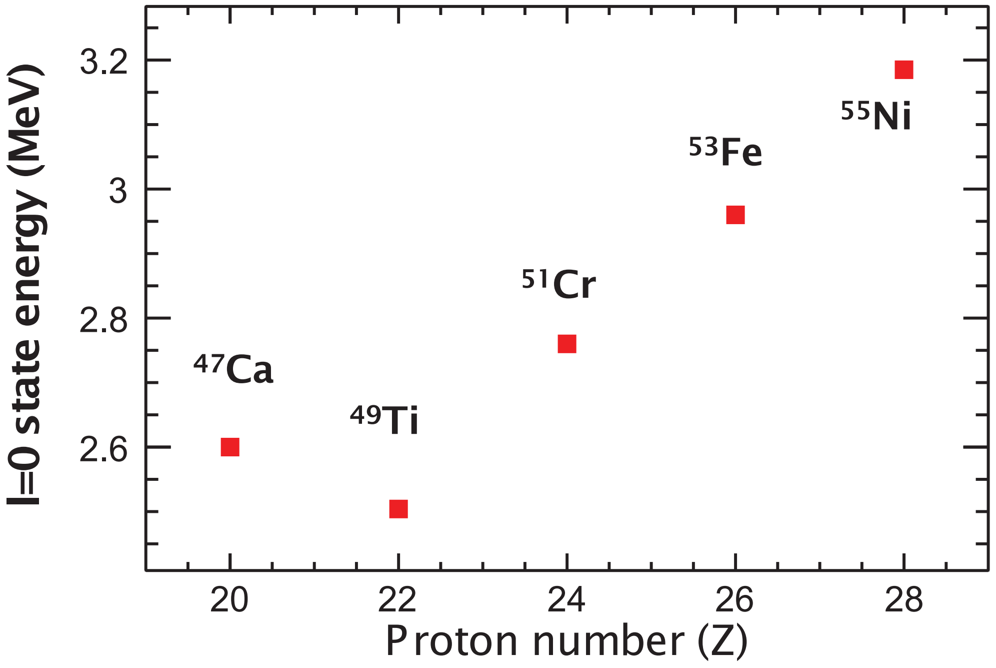

Figure 5.23: Energies of the first $\ell = 0$ ($1s_{1/2}$) states of $N = 27$ isotones with even Z of 20 to 28 (^{47}Ca to ^{55}Ni). The energies increase with increasing Z, with the exception of ^{47}Ca.

The energy levels of these $\ell = 0$ hole states in are in the range of 2.5-3.2 MeV, suggesting similar core structures in those nuclei. Interestingly, as shown in Figure 5.23, there is an overall trend of increasing energies for these states with increasing proton number, with the exception of ^{47}Ca. This is possibly due to stronger binding of neutrons in the $1s_{1/2}$ shell with increasing proton number. However, the higher energy level of this state in ^{47}Ca suggests that there maybe other effects in play. The shell-model calculations of the SF for this state, however, proved to be difficult to perform. This is because the $\ell = 0$ state lies outside the fppn model space used for the nuclei near ^{56}Ni. This calculation should be possible with the inclusion of the sd-shell in the model space, e.g. in a model space including sdf shells.

5.5.3 Evolution of Neutron Hole States in N=28 Nuclei

One of the original purposes of the experiment was to observe the changes in spectroscopic factors as we move towards the edge of the valley of stability. Lee et al. have been investigating global trends in SFs of $N = 28$ isotones [34]. Results of some experiments had expected quenching of the SFs in that region. However, our results show no trend of quenching when we reach the $N = Z = 28$ nucleus. Figure 5.24 shows the spectroscopic factors for $N = 28$ isotones with even Z, and ^{56}Ni(p,d)^{55}Ni reaction SF is shown in red open triangle. Blue open triangles are extracted SF values obtained from the past measurements [30]. For nuclei with shell closure at $N = 20$ (^{48}Ca) and $Z = 28$ (^{56}Ni) we observe higher SFs. The lowering of SFs for nuclei between those nuclei can be partly explained by the fragmentation of SF to isobaric analog states with the same spin and parity values.

5.6 Summary and Outlook

Transfer reactions have been the classic tool for providing information about the angular distributions, the excitation energies, and the spectroscopic factors of possible single-particles states. With the advent of radioactive beams, there has been a renewed effort to utilize these beams transfer reactions in inverse kinematics. In this dissertation, the ^{56}Ni(p,d)^{55}Ni transfer reaction measurement was carried out with the radioactive ^{56}Ni beam in inverse kinematics for the first time. A kinematically complete measurement was necessary, identifying both the light ejectile deuteron and the heavy beam-like residue ^{55}Ni on an event-by-event basis. Beam particles had to be tracked on an event-by-event basis as well, due to large phase-space spread of the radioactive beam and for identification of beam contaminants.

Three detection systems were used. The HiRA array was used for identification of the

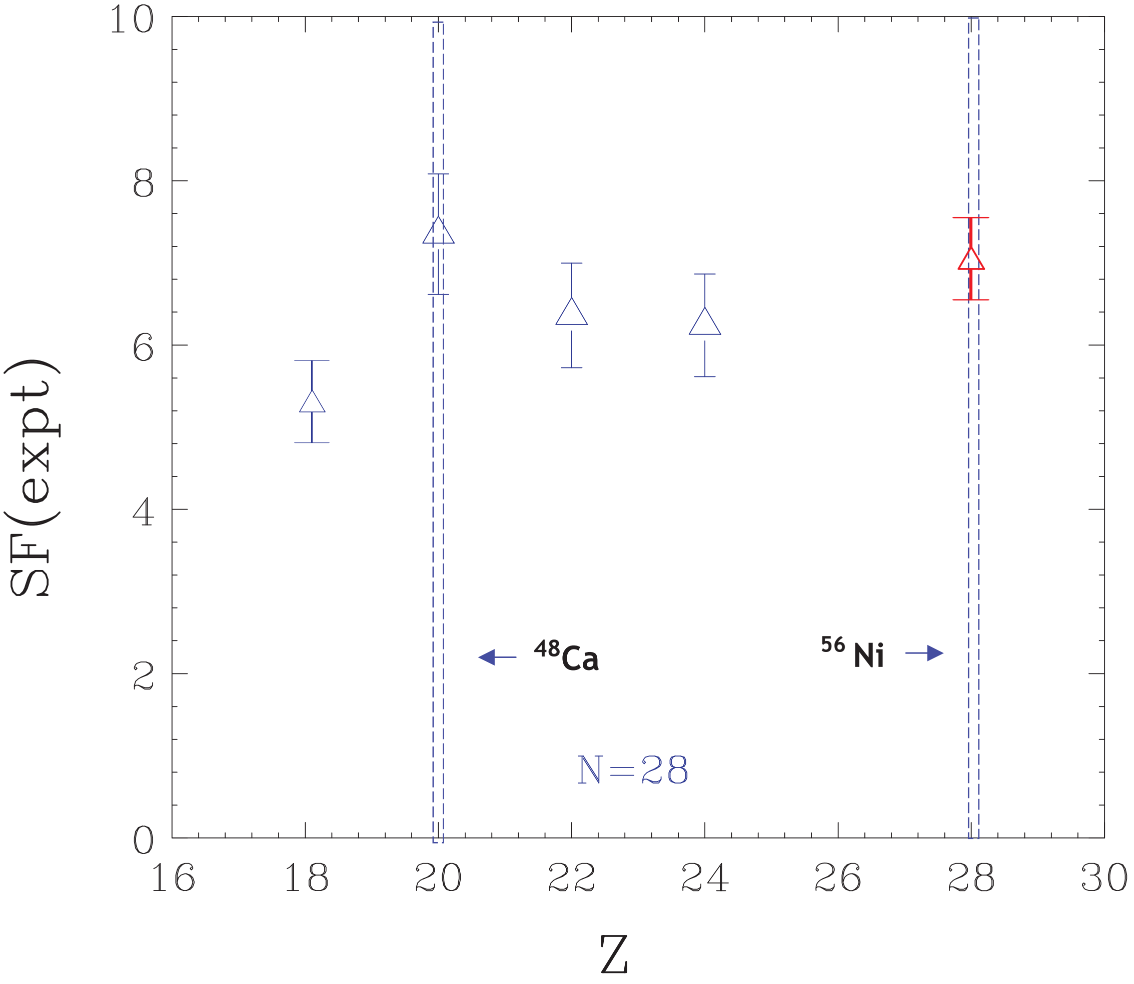

Figure 5.24: Spectroscopic factors for $N = 28$ isotones with even Z. ^{56}Ni(p,d)^{55}Ni reaction SF is shown in red open triangle. Blue open triangles are extracted SF values obtained from the past measurements [30].

deuterons and measuring their energy and angle with high resolution. The S800 spectrograph was used for the identification of the ^{55}Ni residue. Two MCPs were used for tracking of the ^{56}Ni beam particles, measuring their position and time at two places. The MCPs served as the beam counter as well, for the purpose of normalization. We have improved upon the technique of using MCPs for transfer reactions with fast radioactive beams, by utilizing strong magnetic fields and multiple gain stages for MCP signals.

We have extracted spectroscopic factors of the ^{56}Ni(p,d)^{55}Ni reaction, for the ground and two excited states of ^{55}Ni. The neutron SF value of 7 for the ^{56}Ni(p,d)^{55}Ni ground state shows that the current shell model calculations describe the ^{56}Ni nucleus reasonably well. Another important goal was to study the structure of ^{55}Ni by determining the spin and parities of as many excited states as possible. In this regard, ^{55}Ni remains the least studied of the quartet of nuclei one nucleon removed from the doubly-magic ^{56}Ni, ^{55}Ni, ^{57}Ni, ^{55}Co and ^{57}Cu. We have assigned an ℓ value of 1 to first excited state of ^{55}Ni for 2.089 MeV state of ^{55}Ni. We extracted a spectroscopic factor of 0.14 for this state. This serves as a second test of the shell model, and the results agree with the shell model calculations. We confirmed the tentative $\ell = 0$ assumption for 3.185 MeV state. The neutron spectroscopic factor of 1.2 for this state is difficult to compare with shell model calculations. However, the existence of $\ell = 0$ states in other $N = 28$ isotones, notably ^{53}Fe with rather close neutron SF of 1.2, indicate structural similarities of neutron orbitals among these isotones.

In the future, more precise measurements of the ^{56}Ni(p,d)^{55}Ni reaction are necessary for gaining better information about the low lying states of ^{55}Ni. A number of technical improvements can be suggested. Using thinner targets are advantageous for better resolution of states in ^{55}Ni. The technology of using solid/liquid hydrogen is advancing, and using it instead of CH_2 targets would also enhance the resolving powers of measurements. Better beam quality with less spread in phase-space is desirable as well, because even if the beam is accurately tracked, the difference between the actual deuteron angle and the detector angle makes the estimation of geometric efficiency less accurate. From the theoretical standpoint, it is desirable to use more expanded model spaces in the shell model in order to calculate the theoretical SFs for excited states that lie outside of the pf shell. Furthermore, the inconsistency between transfer and knockout reaction model calculations calls for more theoretical studies.

REFERENCES

REFERENCES

[1] H. Yukawa. On the interaction of elementary particles. i. *Proc. Phys. Math. Soc. Japan*, 17:48, 1935.

[2] F. Halzen and A. D. Martin. *Quarks and Leptons:An Introductory Course in Modern Particle Physics*. Wiley, New York, 1984.

[3] https://intra.nscl.msu.edu/illustrations/gallery.php?id=34.

[4] A. Bohr and B. R. Mottelson. *Nuclear Structure*, volume I. Benjamin, New York, 1975.

[5] William D. Myers and Wladyslaw J. Swiatecki. Nuclear masses and deformations. *Nucl. Phys.*, 81:1–60, 1966.

[6] M. G. Mayer and J. H. D. Jensen. *Elementary Theory of Nuclear Shell Structure*. John Wiley and Sons, London, 1960.

[7] R.F. Casten. *Nuclear structure from a simple perspective*. Oxford University Press Inc., New York, 1990.

[8] M. A. Preston and R.K. Bhaduri. *Structure of The Nucleus*. Westview Press, 1993.

[9] B. A. Brown. http://www.nscl.msu.edu/ brown/jina-workshop/bab-lecture-notes.pdf, 2005.

[10] B. A. Brown. The nuclear shell model towards the drip lines. *Progress in Particle and Nuclear Physics*, 47(2):517 – 599, 2001.

[11] A. Akmal, V. R. Pandharipande, and D. G. Ravenhall. Equation of state of nucleon matter and neutron star structure. *Phys. Rev. C*, 58(3):1804–1828, Sep 1998.

[12] W. H. Dickhoff and D. V. Neck. *Many body theory exposed*. World Scientific, Singapore, 2008.

[13] N. Austern. *Direct Nuclear Reaction Theories*. John Wiley and Sons, New York, 1970.

[14] B. A. Brown and W. D. M Rae. Computer program, http://www.nscl.msu.edu/ brown/resources/resources.html.

[15] W. H. Dickhoff and C. Barbieri. Self-consistent green's function method for nuclei and nuclear matter. *Progress in Particle and Nuclear Physics*, 52(2):377 – 496, 2004.

[16] E. Caurier, G. Martinez-Pinedo, F. Nowacki, A. Poves, and A. P. Zuker. The shell model as a unified view of nuclear structure. *Rev. Mod. Phys.*, 77:427–488, Jun 2005.

[17] Ionel Stetcu, Bruce R. Barrett, Petr Navrátil, and James P. Vary. Long- and short-range correlations in the *ab-initio* no-core shell model. *Phys. Rev. C*, 73:037307, Mar 2006.

[18] C. Barbieri and M. Hjorth-Jensen. Quasiparticle and quasihole states of nuclei around ^{56}ni. *Phys. Rev. C*, 79(6):064313, Jun 2009.

[19] K. L. Yurkewicz, D. Bazin, B. A. Brown, C. M. Campbell, J. A. Church, D.-C. Dinca, A. Gade, T. Glasmacher, M. Honma, T. Mizusaki, W. F. Mueller, H. Olliver, T. Otsuka, L. A. Riley, and J. R. Terry. $e2$ excitation strength in ^{55}ni : Coupling of the $^{56}ni2_1^+$ collective core vibration to the $f_{7/2}$ odd neutron hole. *Phys. Rev. C*, 70(6):064321, Dec 2004.

[20] K. L. Yurkewicz, D. Bazin, B. A. Brown, J. Enders, A. Gade, T. Glasmacher, P. G. Hansen, V. Maddalena, A. Navin, B. M. Sherrill, and J. A. Tostevin. One-neutron knockout from ^{57}ni. *Phys. Rev. C*, 74(2):024304, Aug 2006.

[21] K. Minamisono, P. F. Mantica, T. J. Mertzimekis, A. D. Davies, M. Hass, J. Pereira, J. S. Pinter, W. F. Rogers, J. B. Stoker, B. E. Tomlin, and R. R. Weerasiri. Nuclear magnetic moment of the ^{57}cu ground state. *Phys. Rev. Lett.*, 96(10):102501, Mar 2006.

[22] T. E. Cocolios, A. N. Andreyev, B. Bastin, N. Bree, J. Büscher, J. Elseviers, J. Gentens, M. Huyse, Yu. Kudryavtsev, D. Pauwels, T. Sonoda, P. Van den Bergh, and P. Van Duppen. Magnetic dipole moment of $^{57,59}cu$ measured by in-gas-cell laser spectroscopy. *Phys. Rev. Lett.*, 103(10):102501, Aug 2009.

[23] M. Horoi, B. A. Brown, T. Otsuka, M. Honma, and T. Mizusaki. Shell model analysis of the ^{56}ni spectrum in the full pf model space. *Phys. Rev. C*, 73(6):061305, Jun 2006.

[24] J. S. Berryman, K. Minamisono, W. F. Rogers, B. A. Brown, H. L. Crawford, G. F. Grinyer, P. F. Mantica, J. B. Stoker, and I. S. Towner. Doubly-magic nature of ^{56}Ni: Measurement of the ground state nuclear magnetic dipole moment of ^{55}Ni. *Phys. Rev. C*, 79:064305, Jun 2009.

[25] M. Honma, T. Otsuka, B. A. Brown, and T. Mizusaki. New effective interaction for pf-shell nuclei and its implications for the stability of the $n = z = 28$ closed core. *Phys. Rev. C*, 69:034335, Mar 2004.

[26] P.T. Callaghan, M. Kaplan, and N.J. Stone. The magnetic dipole moment of 55co. *Nuclear Physics A*, 201(3):561 – 569, 1973.

[27] D. Mueller, E. Kashy, and W. Benenson. Coulomb displacement energies of the $a = 4n+3$, $t = \frac{1}{2}$ mirror nuclei in the $1f_{\frac{7}{2}}$ shell. *Phys. Rev. C*, 15(4):1282–1287, Apr 1977.

[28] Huo Junde. Nuclear data sheets for a = 55. *Nuclear Data Sheets*, 109(4):787 – 942, 2008.

[29] M.H. Macfarlane and J.P. Schiffer. *Nuclear Spectroscopy and Reactions*, volume 40B. Academic, New York, London, 1974.

[30] Jenny Lee, M. B. Tsang, W. G. Lynch, M. Horoi, and S. C. Su. Neutron spectroscopic factors of ni isotopes from transfer reactions. *Phys. Rev. C*, 79:054611, May 2009.

[31] M. B. Tsang, Jenny Lee, and W. G. Lynch. Survey of ground state neutron spectroscopic factors from li to cr isotopes. *Phys. Rev. Lett.*, 95(22):222501, Nov 2005.

[32] Jenny Lee, J. A. Tostevin, B. A. Brown, F. Delaunay, W. G. Lynch, M. J. Saelim, and M. B. Tsang. Reduced neutron spectroscopic factors when using potential geometries constrained by hartree-fock calculations. *Phys. Rev. C*, 73:044608, Apr 2006.

[33] A. F. Lisetskiy, B. A. Brown, M. Horoi, and H. Grawe. New $t = 1$ effective interactions for the $f_{5/2}\, p_{3/2}\, p_{1/2}\, g_{9/2}$ model space: Implications for valence-mirror symmetry and seniority isomers. *Phys. Rev. C*, 70:044314, Oct 2004.

[34] Jenny Lee. Private communication.

[35] Ian J. Thompson and Filomena M. Nunes. *Nuclear Reactions for Astrophysics*. University Press, Cambridge, 2009.

[36] H. Feshbach, C. E. Porter, and V. F. Weisskopf. Model for nuclear reactions with neutrons. *Phys. Rev.*, 96(2):448–464, Oct 1954.

[37] G.R. Satchler. *Introduction to Nuclear Reactions*. Macmillan, London, 1980.

[38] D.F. Jackson et al. *Nuclear Reactions*. Methuen, London, 1970.

[39] G. J. Kramer, H. P. Blok, and L. Lapikás. A consistent analysis of (e,e'p) and (d,3he) experiments. *Nuclear Physics A*, 679(3-4):267 – 286, 2001.

[40] F. Perey and B. Buck. A non-local potential model for the scattering of neutrons by nuclei. *Nuclear Physics*, 32:353 – 380, 1962.

[41] P J A Buttle and L J B Goldfarb. Finite range effects in deuteron stripping processes. *Proceedings of the Physical Society*, 83(5):701, 1964.

[42] R. C. Johnson and P. J. R. Soper. Contribution of deuteron breakup channels to deuteron stripping and elastic scattering. *Phys. Rev. C*, 1:976–990, Mar 1970.

[43] R. L. Varner, W. J. Thompson, T. L. McAbee, E. J. Ludwig, and T. B. Clegg. A global nucleon optical model potential. *Physics Reports*, 201(2):57 – 119, 1991.

[44] X. D. Liu. *Stripping reactions induced by N=6 isotones*. Ph.d. thesis, Michigan State University, 2005.

[45] F. Nunes. Private communication, 2008.

[46] B. E. F. Macefield. Energy dependence of (d, p) reactions on heavy mass targets. *Nuclear Physics*, 59(4):573 – 579, 1964.

[47] Jenny Lee, M. B. Tsang, and W. G. Lynch. Neutron spectroscopic factors from transfer reactions. *Phys. Rev. C*, 75:064320, Jun 2007.

[48] R. C. Johnson, E. J. Stephenson, and J. A. Tostevin. Nature of the amplitudes missing from adiabatic distorted-wave models of medium energy (d, p) and (p, d) reactions. *Nuclear Physics A*, 505(1):26 – 66, 1989.

[49] M. Igarashi et al. Computer program twofnr (surrey university version).

[50] N. Keeley, N. Alamanos, and V. Lapoux. Comprehensive analysis method for (d,p) stripping reactions. *Phys. Rev. C*, 69:064604, Jun 2004.

[51] F. Delaunay, F. M. Nunes, W. G. Lynch, and M. B. Tsang. Coupling and higher-order effects in the ^{12}C$(d,p)^{13}$C and ^{13}C$(p,d)^{12}$C reactions. *Phys. Rev. C*, 72:014610, Jul 2005.

[52] L.D. Knutson, J.A. Thomson, and H.O. Meyer. Deuteron d-state effects for the reactions 117sn(d, p)118sn and 119sn(d, p)120sn. *Nuclear Physics A*, 241(1):36 – 46, 1975.

[53] Jenny Lee. *SURVEY OF NEUTRON SPECTROSCOPIC FACTORS AND ASYMMETRY DEPENDENCE OF NEUTRON CORRELATIONS IN TRANSFER REACTIONS*. Ph.D. thesis, Michigan State University, 2010.

[54] M.S. Wallace, M.A. Famiano, M.-J. van Goethem, A.M. Rogers, W.G. Lynch, J. Clifford, F. Delaunay, J. Lee, S. Labostov, M. Mocko, L. Morris, A. Moroni, B.E. Nett, D.J. Oostdyk, R. Krishnasamy, M.B. Tsang, R.T. de Souza, S. Hudan, L.G. Sobotka, R.J. Charity, J. Elson, and G.L. Engel. The high resolution array (hira) for rare isotope beam experiments. *Nuclear Instruments and Methods in Physics Research Section A: Accelerators, Spectrometers, Detectors and Associated Equipment*, 583(2-3):302 – 312, 2007.

[55] J Yurkon, D Bazin, W Benenson, D.J Morrissey, B.M Sherrill, D Swan, and R Swanson. Focal plane detector for the s800 high-resolution spectrometer. *Nuclear Instruments and Methods in Physics Research Section A: Accelerators, Spectrometers, Detectors and Associated Equipment*, 422(1-3):291 – 295, 1999.

[56] D. Bazin, J. A. Caggiano, B. M. Sherrill, J. Yurkon, and A. Zeller. The s800 spectrograph. *Nuclear Instruments and Methods in Physics Research Section B: Beam Interactions with Materials and Atoms*, 204:629 – 633, 2003. 14th International Conference on Electromagnetic Isotope Separators and Techniques Related to their Applications.

[57] D. Shapira, T. A. Lewis, L. D. Hulett, and Z. Ciao. Factors affecting the performance of detectors that use secondary electron emission from a thin foil to determine ion impact position. *Nuclear Instruments and Methods in Physics Research Section A: Accelerators, Spectrometers, Detectors and Associated Equipment*, 449(1-2):396 – 407, 2000.

[58] D. Shapira, T. A. Lewis, and L. D. Hulett. A fast and accurate position-sensitive timing detector based on secondary electron emission. *Nuclear Instruments and Methods in Physics Research Section A: Accelerators, Spectrometers, Detectors and Associated Equipment*, 454(2-3):409 – 420, 2000.

[59] Rogers et al. Use of micro channel plates in transfer reactions. In preparation.

[60] The k500+k1200, a coupled cyclotron facility at the national superconducting cyclotron laboratory., July 1994.

[61] D. J. Morrissey. The coupled cyclotron project at the nscl. *Nuclear Physics A*, 616(1-2):45 – 55, 1997. Radioactive Nuclear Beams.

[62] B. M. Sherrill. Scientific opportunities with the nscl coupled cyclotron facility. *Prog. Theor. Physics*, 146:6069, 2002.

[63] F. Marti, P. Miller, D. Poe, M. Steiner, J. Stetson, and X. Y. Wu. Commissioning of the coupled cyclotron system at nscl. In *AIP CONFERENCE PROCEEDINGS*, pages 64–68, 2001.

[64] D. J. Morrissey, B. M. Sherrill, M. Steiner, A. Stolz, and I. Wiedenhoever. Commissioning the a1900 projectile fragment separator. *Nuclear Instruments and Methods in Physics Research Section B: Beam Interactions with Materials and Atoms*, 204:90 – 96, 2003. 14th International Conference on Electromagnetic Isotope Separators and Techniques Related to their Applications.

[65] Glenn F. Knoll. *Radiation detection and measurement, 3rd edition.* Wiley & Sons, Inc, New York, 1999.

[66] M. S. Wallace. *Experimental and Theoretical Challenges in Understanding the rp-Process on Accreting Neutron Stars.* Ph.d. thesis, Michigan State University, 2005.

[67] A. Wagner, W. P. Tan, K. Chalut, R. J. Charity, B. Davin, Y. Larochelle, M. D. Lennek, T. X. Liu, X. D. Liu, W. G. Lynch, A. M. Ramos, R. Shomin, L. G. Sobotka, R. T. de Souza, M. B. Tsang, G. Verde, and H. S. Xu. Energy resolution and energy-light response of csi(tl) scintillators for charged particle detection. *Nuclear Instruments and Methods in Physics Research Section A: Accelerators, Spectrometers, Detectors and Associated Equipment*, 456(3):290 – 299, 2001.

[68] V. Avdeichikov, B. Jakobsson, V.A. Nikitin, P.V. Nomokonov, and E.J. van Veldhuizen. On-beam calibration of the [delta]e(si)-sci/pd charged particle telescope. *Nuclear Instruments and Methods in Physics Research Section A: Accelerators, Spectrometers, Detectors and Associated Equipment*, 466(3):427 – 435, 2001.

[69] M. J. van Goethem, M. S. Wallace, B. E. Nett, M. A. Famiano, K. R. Herner, D. J. Oostdyk, M. Mocko, W. G. Lynch, M. B. Tsang, P. Schotanus, J. Telfer, H. L. Clark, A. Moroni, R. de Souza, and L. G. Sobotka. Investigations and corrections of the light output uniformity of csi(tl) crystals. *Nuclear Instruments and Methods in Physics Research Section A: Accelerators, Spectrometers, Detectors and Associated Equipment*, 526(3):455 – 476, 2004.

[70] J. E. Birks. *Theory and practice of scintillation counters.* Oxford, 1964.

[71] S.R. Klein, P. Barale, E. Beuville, F. Bieser, K. Dao, S. Kleinfelder, V. Lindenstruth, M.A. Lisa, C. McParland, T. Noggle, H.G. Ritter, C. Vu, H. Wieman, A. Aluyshin, and M. Aluyshin. Front end electronics for the star tpc. *Nuclear Science, IEEE Transactions on*, 43(3):1768 –1772, jun 1996.

[72] Joseph Caggiano. *Spectroscopy of Exotic Nuclei with the S800 Spectrograph.* Ph.D. thesis, Michigan State University, 1999.

[73] M. Berz, K. Joh, J. A. Nolen, B. M. Sherrill, and A. F. Zeller. Reconstructive correction of aberrations in nuclear particle spectrographs. *Phys. Rev. C*, 47(2):537–544, Feb 1993.

[74] J. Adams and B.W. Manley. The mechanism of channel electron multiplication. *IEEE Transactions on Nuclear Science*, NS-13:88, June 1966.

[75] Joseph Ladislas Wiza. Microchannel plate detectors. *Nuclear Instruments and Methods*, 162(1-3):587 – 601, 1979.

[76] www.photonis.com.

[77] A. M. Rogers. Study of ^{69}Br proton decay, 2005.

[78] E. C. Pollacco, J. C. Jacmart, Y. Blumenfeld, Ph. Chomaz, N. Frascaria, J. P. Garron, and J. C. Roynette. A compact gridless channel plate detector for time-of-flight measurements. *Nuclear Instruments and Methods in Physics Research*, 225(1):51 – 56, 1984.

[79] O. H. Odland, W. Mittig, A. Lï£¡pine-Szily, G. Fremont, M. Chartier, M. MacCormick, and J. M. Casandjian. A fast position sensitive microchannel plate detector for ray-tracing of charged particles. *Nuclear Instruments and Methods in Physics Research Section A: Accelerators, Spectrometers, Detectors and Associated Equipment*, 378(1-2):149 – 154, 1996.

[80] J. L. Culhane. Position sensitive detectors in x-ray astronomy. *Nuclear Instruments and Methods in Physics Research Section A: Accelerators, Spectrometers, Detectors and Associated Equipment*, 310(1-2):1 – 13, 1991.

[81] Quantar technology inc., 200 washington st., santa cruz, ca 950604976, usa.

[82] http://www.acuitylaser.com/ar600/index.shtml.

[83] http://www.owis-staufen.com.

[84] George L. Engel, Muthukumar Sadasivam, Mythreyi Nethi, Jon M. Elson, Lee G. Sobotka, and Robert J. Charity. A multi-channel integrated circuit for use in low- and intermediate-energy nuclear physics–hinp16c. *Nuclear Instruments and Methods in Physics Research Section A: Accelerators, Spectrometers, Detectors and Associated Equipment*, 573(3):418 – 426, 2007.

[85] http://www.root.cern.ch.

[86] Electronic instrument services, department of chemistry, indiana university, bloomington.

[87] V. Henzl. Private communication, 08.

[88] O.B. Tarasov and D. Bazin. Lise++: Radioactive beam production with in-flight separators. *Nuclear Instruments and Methods in Physics Research Section B: Beam Interactions with Materials and Atoms*, 266(19-20):4657 – 4664, 2008. Proceedings of the XVth International Conference on Electromagnetic Isotope Separators and Techniques Related to their Applications.

[89] B Davin, R.T de Souza, R Yanez, Y Larochelle, R Alfaro, H.S Xu, A Alexander, K Bastin, L Beaulieu, J Dorsett, G Fleener, L Gelovani, T Lefort, J Poehlman, R.J Charity, L.G Sobotka, J Elson, A Wagner, T.X Liu, X.D Liu, W.G Lynch, L Morris, R Shomin, W.P Tan, M.B Tsang, G Verde, and J Yurkon. Lassa: a large area silicon strip array for isotopic identification of charged particles. *Nuclear Instruments and Methods in Physics Research Section A: Accelerators, Spectrometers, Detectors and Associated Equipment*, 473(3):302 – 318, 2001.

[90] Western michigan university tandem van de graaf accelerator.

[91] H. Backe, P. Senger, W. Bonin, E. Kankeleit, M. Krämer, R. Krieg, V. Metag, N. Trautmann, and J. B. Wilhelmy. Estimates of the nuclear time delay in dissipative u + u and u + cm collisions derived from the shape of positron and δ-ray spectra. *Phys. Rev. Lett.*, 50(23):1838–1841, Jun 1983.

[92] J. D. Jackson. *Classical Electrodynamics, 3rd edition, Chapter 13.* Wiley, 1998.

[93] J. C. Ashley, J. C. Tung, , and R. H. Ritchie. Inelastic interactions of electrons with polystyrene: Calculations of mean free paths, stopping powers, and csda ranges. *IEEE Trans. Nucl. Sci. NS*, 26, 1978.

[94] R. Krieg, E. Boek, U. Gollerthan, E. Kankeleit, G. Klotz-Engmann, M. Krämer, U. Meyer, H. Oeschler, and P. Senger. Reaction dynamics studied via positron and electron spectroscopy. *Phys. Rev. C*, 34(2):562–575, Aug 1986.

[95] NNDC. http://www.nndc.bnl.gov.

[96] F. Nunes. Private communication, 2011.

[97] B. Alex Brown and W. A. Richter. New “usd” hamiltonians for the *sd* shell. *Phys. Rev. C*, 74(3):034315, Sep 2006.

[98] D. Weishaar. Experiment 06020, single-particle and single-hole states near ^{56}Ni.

[99] T. Suehiro, J.E. Finck, and J.A. Nolen Jr. A study of the 54fe(p, d)53fe reaction at 40 mev. *Nuclear Physics A*, 313(1-2):141 – 156, 1979.

[100] H. Xiaolong. Nuclear Data Sheets for A = 51. *Nuclear Data Sheets*, 107:2131–2322, August 2006.